

University of California  
Santa Barbara

# A Search for *R*-parity violating supersymmetry at the 13 TeV LHC

A dissertation submitted in partial satisfaction  
of the requirements for the degree

Doctor of Philosophy  
in  
Physics

by

Rohan Bhandari

Committee in charge:

Professor David Stuart, Chair  
Professor Harry Nelson  
Professor Nathaniel Craig

June 2018

The Dissertation of Rohan Bhandari is approved.

---

Professor Harry Nelson

---

Professor Nathaniel Craig

---

Professor David Stuart, Committee Chair

May 2018

A Search for  $R$ -parity violating supersymmetry at the 13 TeV LHC

Copyright © 2018

by

Rohan Bhandari

Dedication here

## **Acknowledgements**

Acknowledgements Here.

# **Curriculum Vitæ**

## Rohan Bhandari

### **Education**

- |      |   |
|------|---|
| 20XX | Ph.D. in Physics (Expected), University of California, Santa Barbara. |
| 20XX | M.A. in Physics, University of California, Santa Barbara.             |
| 20XX | etc   |

### **Publications**

Publications.

**Abstract**

A Search for  $R$ -parity violating supersymmetry at the 13 TeV LHC

by

Rohan Bhandari

Abstract text.

# Contents

<b>Curriculum Vitae</b>	<b>vi</b>
<b>Abstract</b>	<b>vii</b>
<b>List of Figures</b>	<b>xi</b>
<b>List of Tables</b>	<b>xvi</b>
<b>0 Introduction for Non-technical Readers</b>	<b>1</b>
<b>1 Introduction</b>	<b>2</b>
<b>Part I Theoretical Context and Motivations</b>	<b>3</b>
<b>2 The Standard Model</b>	<b>4</b>
2.1 Overview and Successes . . . . .	4
2.2 The Standard Model as an Incomplete Theory . . . . .	6
2.2.1 The Hierarchy Problem and Naturalness . . . . .	8
<b>3 Supersymmetry</b>	<b>11</b>
3.1 Natural Supersymmetry . . . . .	11
3.2 Phenomenological and Experimental Constraints . . . . .	14
3.3 $R$ -parity violating Supersymmetry . . . . .	18
3.3.1 Minimal Flavor Violating Supersymmetry . . . . .	20
<b>Part II Experimental Apparatus</b>	<b>22</b>
<b>4 Experimental Apparatus</b>	<b>23</b>
4.1 The Large Hadron Collider . . . . .	24
4.2 Compact Muon Solenoid . . . . .	26

4.2.1	Inner Tracking System . . . . .	28
4.2.2	Electromagnetic Calorimeter . . . . .	29
4.2.3	Hadronic Calorimeter . . . . .	30
4.2.4	Muon System . . . . .	33
4.2.5	Trigger System . . . . .	34
<b>5</b>	<b>Particle Reconstruction and Identification</b>	<b>38</b>
5.1	Tracks . . . . .	38
5.1.1	Vertices . . . . .	39
5.2	Calorimeter Clusters . . . . .	40
5.3	Particle Flow . . . . .	41
5.3.1	Linking . . . . .	41
5.3.2	PF Reconstruction and Identification . . . . .	43
5.4	Leptons . . . . .	44
5.4.1	Electrons . . . . .	44
5.4.2	Muons . . . . .	46
5.5	Jets . . . . .	47
5.5.1	Clustering . . . . .	48
5.5.2	Selection . . . . .	49
5.5.3	b-tagging . . . . .	50
5.6	Large-radius Jets . . . . .	53
5.6.1	$M_J$ . . . . .	54
<b>Part III</b>	<b>Data, Simulation, and Selection</b>	<b>57</b>
<b>6</b>	<b>Data Samples and Simulation</b>	<b>58</b>
6.1	Data . . . . .	58
6.2	Monte Carlo Simulation . . . . .	58
6.2.1	Background Samples . . . . .	61
6.2.2	Signal Samples . . . . .	61
<b>7</b>	<b>Event Selection</b>	<b>65</b>
7.1	Baseline selection . . . . .	65
7.2	Trigger Efficiency . . . . .	68
7.3	Analysis Binning . . . . .	71
<b>Part IV</b>	<b>The Search</b>	<b>76</b>
<b>8</b>	<b>Background Prediction</b>	<b>77</b>
8.1	Overview . . . . .	77
8.2	$t\bar{t}$ and QCD Normalizations . . . . .	78

8.2.1	$M_J$ Connection . . . . .	79
8.3	W + jets Normalization . . . . .	81
8.4	Other Normalization . . . . .	83
<b>9</b>	<b>Systematic Uncertainties</b>	<b>84</b>
9.1	Gluon Splitting Rate . . . . .	84
9.2	b-tagging Data-to-simulation Scale Factors . . . . .	89
9.3	Lepton Fake Rate in QCD . . . . .	93
9.4	Additional systematic uncertainties . . . . .	94
9.4.1	$N_b$ distribution with NLO Precision . . . . .	95
9.5	Signal Systematics . . . . .	97
<b>10</b>	<b>Fit Validation</b>	<b>99</b>
10.1	Signal Injection Study . . . . .	99
10.2	Control Region Fit . . . . .	103
<b>11</b>	<b>Results and Interpretation</b>	<b>109</b>
11.1	Results . . . . .	109
11.2	Interpretation and Limits . . . . .	113
<b>12</b>	<b>Conclusions</b>	<b>114</b>
12.1	Section Title . . . . .	114
<b>Part V</b>	<b>Appendix</b>	<b>115</b>
<b>A</b>	<b>DeepJEC</b>	<b>116</b>
A.1	Section Title . . . . .	116
<b>B</b>	<b>HF Timing</b>	<b>117</b>
B.1	Section Title . . . . .	117
<b>Bibliography</b>		<b>118</b>

# List of Figures

2.1	The fundamental particles of the Standard Model and some of their properties. . . . .	5
2.2	The theoretical and experimental value for the production cross section of various processes [1]. . . . .	7
2.3	The fermionic one-loop Higgs mass correction. . . . .	10
3.1	The scalar one-loop Higgs mass correction. . . . .	13
3.2	An example spectrum for natural SUSY. . . . .	15
3.3	An overview of recent results from SUSY searches from the Compact Muon Solenoid experiment [2]. . . . .	16
3.4	An overview of recent results from SUSY searches from the A Toroidal LHC Apparatus experiment [3]. . . . .	17
3.5	Example diagram representing proton decay, where the particle $\tilde{d}_j$ represents a down-type squark [4]. The left vertex is mediated by the baryon number violating coupling, $\lambda''$ , and the right vertex is mediated by the lepton number violating coupling, $\lambda'$ . . . . .	19
3.6	Example diagram of the pair production of gluinos that decay via $\tilde{g} \rightarrow \tilde{t}\bar{t} \rightarrow tbs$ . . . . .	21
4.1	A schematic of the CERN LHC accelerator complex. [5] . . . . .	24
4.2	Ratio of parton luminosities at $\sqrt{s} = 13$ and 8 TeV. [6] . . . . .	26
4.3	A diagram showing the various sub-detectors of the CMS detector. [7] . .	27
4.4	A diagram of the cartesian and cylindrical coordinate systems used by CMS. [8] . . . . .	28
4.5	Layout of the CMS tracking system, showing both the pixel detector (blue) and the strips detector (red). [9] . . . . .	29
4.6	A cross section of the ECAL, showing its geometry and layout. [10] . . .	31
4.7	The layout and geometry of a quarter of the HCAL detector. [11] . . . .	32
4.8	The layout of the muon system within the CMS detector. [12] . . . . .	33
4.9	Flowchart depicting the generation of a L1 Accept. [13] . . . . .	36
5.1	The efficiency to select an analysis-level electron as a function of $p_T$ and $\eta$ . .	46

5.2	The efficiency to select an analysis-level muon as a function of $p_T$ and $\eta$ . . . . .	48
5.3	The distribution of the CSVv2 discriminator values for jets of different flavors. Jets are selected from $t\bar{t}$ events and required to have $p_T > 20$ GeV [14]. . . . .	52
5.4	The efficiency of the CSVv2 algorithm as a function of jet $p_T$ at the working point used in this analysis. . . . .	53
5.5	Distributions of $M_J$ , normalized to the same area, for $t\bar{t}$ events and signal events with $m_{\tilde{g}} = 1000$ GeV and 1600 GeV in a selection of $N_{\text{leps}} = 1$ , $H_T > 1200$ GeV, $N_{\text{jets}} \geq 8$ , $M_J > 500$ GeV, and $N_b \geq 1$ . . . . .	56
6.1	Delivered and recorded integrated luminosity by the LHC and CMS, respectively, over 2016. [15] . . . . .	59
6.2	Example diagram of the T1tbs simplified model. . . . .	64
7.1	The N-1 plots for $N_{\text{leps}}$ (top-left), $H_T$ (top-right), $M_J$ (middle-left), $N_{\text{jets}}$ (middle-right), and $N_b$ (bottom). The black dashed vertical line represents the value of the corresponding baseline requirement. . . . .	66
7.2	Trigger efficiency for HLT_PFHT900 as a function of $H_T$ in Runs B-G (top-left), Run H (top-right), and full dataset (bottom). The efficiencies are measured using a data sample collected with the HLT_Ele27_WPTight trigger and an offline requirement of at least one electron and at least four jets. . . . .	69
7.3	Trigger efficiency as a function of $H_T$ for HLT_PFBjet450 in the full dataset (top-left) and for the combination of HLT_PFHT900 and HLT_PFBjet450 in Run H (top-right) and the full dataset (bottom). The efficiencies are measured using a data sample collected with the HLT_Ele27_WPTight trigger and an offline requirement of at least one electron and at least four jets. . . . .	70
7.4	Trigger efficiency as a function of $M_J$ (top-left), $N_{\text{jets}}$ (top-right), and $N_b$ (bottom) for the combination of the HLT_PFHT900 and HLT_PFBjet450 triggers in the full dataset. The efficiencies are measured using a data sample collected using the HLT_Ele27_WPTight trigger and an offline requirement of at least one electron, at least four jets, and $H_T > 1200$ GeV. . . . .	72
7.5	Illustration depicting the $N_{\text{jets}}$ , $M_J$ binning after the baseline selection, with control and signal region bins denoted by “CR” and “SR”, respectively. . . . .	73
7.6	The simulated $N_b$ distribution for background and signal processes in the control region bins. The top-left plot corresponds to the $4 \leq N_{\text{jets}} \leq 5$ , $500 \leq M_J \leq 800$ GeV bin, the top-right plot to the $5 \geq N_{\text{jets}} \geq 6$ , $M_J \geq 800$ GeV bin, and the bottom plot to the $6 \leq N_{\text{jets}} \leq 7$ , $500 \leq M_J \leq 800$ GeV bin. . . . .	74

7.7	The simulated $N_b$ distribution for background and signal processes in the signal region bins. The top-left plot corresponds to the $6 \leq N_{\text{jets}} \leq 7$ , $800 \leq M_J \leq 1000$ GeV bin, the top-right plot to the $6 \geq N_{\text{jets}} \geq 7$ , $M_J \geq 1000$ GeV bin, the middle-left plot to the $N_{\text{jets}} \geq 8$ , $500 \leq M_J \leq 800$ GeV bin, the middle-right plot to the $N_{\text{jets}} \geq 8$ , $800 \leq M_J \leq 1000$ GeV, and the bottom plot to the $N_{\text{jets}} \geq 8$ , $M_J \geq 1000$ GeV bin. . . . .	75
8.1	Diagram depicting the $N_{\text{jets}}$ , $M_J$ binning of the $N_{\text{leps}} = 0$ QCD control region. . . . .	79
8.2	Distribution of post-fit yields of $t\bar{t}$ in the $N_{\text{jets}} \geq 8$ , $M_J > 1000$ GeV bin for 1,000 psuedodata experiments without (left) and with (right) constraints between adjacent $M_J$ bins. The dotted black line indicates the pre-fit yield. . . . .	80
8.3	Data-to-simulation ratios as a function of $M_J$ for different $N_{\text{jets}}$ bins (data points) with a selection of $N_{\text{leps}} = 1$ , $H_T > 1200$ GeV, and $N_b = 1$ applied. The shaded region corresponds to the size of the $M_J$ connection in each $M_J$ bin. . . . .	81
8.4	Jet multiplicity distribution for data and simulation in a Z + jets control sample selected by requiring $N_{\text{leps}} = 2$ , $H_T > 1200$ GeV, $M_J > 500$ GeV, $N_b = 1$ , and $80 < m_{\ell\ell} < 100$ GeV. The total yield from simulation is normalized to the number of events in data. The uncertainty in the ratio of data to simulation yields (lower panel) is statistical only. . . . .	82
9.1	The $\Delta R_{b\bar{b}}$ distribution shapes for the three gluon splitting categories: Events with a pair of b-tagged jets resulting from gluon splitting (green), events with a gluon splitting yielding fewer than 2 b-tagged jets (blue), and events without a gluon splitting to $b\bar{b}$ . These events are selected by requiring $N_{\text{leps}} = 0$ , $H_T > 1500$ GeV, $M_J > 500$ GeV, $N_{\text{jets}} \geq 4$ , and $N_b = 2$ . . . . .	85
9.2	The relative fraction of the possible final states that occur from gluon splitting to $b\bar{b}$ for events satisfying $N_{\text{leps}} = 0$ , $H_T > 1500$ GeV, $M_J > 500$ GeV, $N_{\text{jets}} \geq 4$ , and $N_b = 2$ . . . . .	86
9.3	Post-fit $\Delta R_{b\bar{b}}$ distributions in a selection with $N_{\text{leps}} = 0$ , $H_T > 1500$ GeV, $M_J > 500$ GeV, $N_{\text{jets}} \geq 4$ , and $N_b = 2$ with the post-fit uncertainty represented by a hatched band. The ratio of data to simulation yields is shown in the lower panel. . . . .	88
9.4	Effect of the $\pm 1$ s.d. variations of the gluon splitting rate on the $N_b$ distribution in $t\bar{t}$ events for the two most sensitive bins: ( $N_{\text{jets}} \geq 8$ , $800 < M_J \leq 1000$ GeV) (left) and ( $N_{\text{jets}} \geq 8$ , $M_J > 1000$ GeV) (right). Event yields are normalized to that expected in $35.9 \text{ fb}^{-1}$ of data. . . . .	88
9.5	The data-to-simulation scale factors for the tagging efficiency of b-flavor jets (top-left), charm-flavor jets (top-right), and light-flavor or gluon jets (bottom) are shown as a function of jet $p_T$ . The associated uncertainty with each scale factor is shown as a blue hashed band. . . . .	91

9.6	Effect of the $\pm 1$ s.d. correlated variations of the b-flavor and c-flavor jet data-to-simulation scale factors on the $N_b$ distribution in $t\bar{t}$ for the two most sensitive bins: ( $N_{\text{jets}} \geq 8$ , $800 < M_J \leq 1000$ GeV) (left) and ( $N_{\text{jets}} \geq 8$ , $M_J > 1000$ GeV) (right). Event yields are normalized to that expected in $35.9 \text{ fb}^{-1}$ of data. . . . .	92
9.7	Effect of the $\pm 1$ s.d. variations of the light-flavor jet data-to-simulation scale factors on the $N_b$ distribution in $t\bar{t}$ for the two most sensitive bins: ( $N_{\text{jets}} \geq 8$ , $800 < M_J \leq 1000$ GeV) (left) and ( $N_{\text{jets}} \geq 8$ , $M_J > 1000$ GeV) (right). Event yields are normalized to that expected in $35.9 \text{ fb}^{-1}$ of data. . . . .	92
9.8	The relative isolation distribution for electrons (left) and muons (right) in the control region bins. The binning of the histograms are chosen such that the first bin corresponds to the relative isolation requirement for signal leptons (0.1 for electrons and 0.2 for muons). The normalizations of the QCD, $t\bar{t}$ , and $W + \text{jets}$ processes are scaled to match the results of a control region fit described in Section 10.2. . . . .	94
9.9	Background systematic uncertainties affecting the $N_b$ shape (in percent) for the ( $N_{\text{jets}} \geq 8$ , $500 < M_J \leq 1000$ GeV) (left) and ( $N_{\text{jets}} \geq 8$ , $M_J > 1000$ GeV) (right) bins. The bottom row shows the total uncertainty for a given $N_b$ bin by summing in quadrature all uncertainties. These values are similar for other ( $N_{\text{jets}}$ , $M_J$ ) bins. . . . .	96
9.10	Comparison of the $N_b$ distribution for a sample generated at LO precision with MADGRAPH5_aMC@NLO 2.2.2 (blue histogram) with that of one generated at NLO precision with POWHEG 2.0 (data points). The comparison is done after the baseline selection and in bins of $4 \leq N_{\text{jets}} \leq 5$ (left), $6 \leq N_{\text{jets}} \leq 7$ (middle), and $N_{\text{jets}} \geq 8$ (right). In order to evaluate only shape differences, the MADGRAPH5_aMC@NLO sample is normalized to match the normalization of the POWHEG sample. . . . .	96
9.11	Signal systematic uncertainties affecting the $N_b$ shape (in percent) for the ( $N_{\text{jets}} \geq 8$ , $500 < M_J \leq 1000$ GeV) (left) and ( $N_{\text{jets}} \geq 8$ , $M_J > 1000$ GeV) (right) bins. The bottom row shows the total uncertainty for a given $N_b$ bin by summing in quadrature all uncertainties. These values are similar for other ( $N_{\text{jets}}$ , $M_J$ ) bins. . . . .	98
10.1	Median extracted signal strength of 1,000 psuedodata experiments as a function of gluino mass. The uncertainties drawn are the median upper and lower errors of the fitted signal strengths per mass point. . . . .	101
10.2	Distribution of fitted signal strengths of 1000 psuedodata experiments for a 2000 GeV gluino at 1x (top-left), 3x (top-right), 5x (bottom-left), and 10x (bottom-right) the nominal cross-section. The amount of signal extracted is 78%, 92%, 95%, and 98% the injected signal, respectively. . . . .	102
10.3	Post-fit $N_b$ distributions of the control region fit. . . . .	104

10.4 Post-fit pulls of the background-only control region fit. The post-fit value of the nuisance parameter is indicated by the data point, while the post-fit uncertainty is shown as a black line and is normalized by the pre-fit uncertainty depicted as the blue band. . . . .	105
10.5 Pre-fit $N_b$ distributions of the control region bins with the background simulation normalized to the observed data yields with a single scaling factor. The ratio of data-to-simulation is shown in the lower panel. The pre-fit uncertainty is represented by the hatched band. . . . .	106
11.1 Data and the background-only post-fit $N_b$ distribution for bins with low expected signal contribution: $4 \leq N_{\text{jets}} \leq 5$ , $500 < M_J \leq 800$ GeV (upper-left), $4 \leq N_{\text{jets}} \leq 5$ , $M_J > 800$ GeV (upper-right), $6 \leq N_{\text{jets}} \leq 7$ , $500 < M_J \leq 800$ GeV (lower-left), and $N_{\text{jets}} \geq 8$ , $500 < M_J \leq 800$ GeV (lower-right). The expected signal distribution is also shown for a gluino mass of 1600 GeV. The ratio of data to post-fit yields is shown in the lower panel. The post-fit uncertainty is depicted as a hatched band. . . . .	110
11.2 Data and the background-only post-fit $N_b$ distribution for bins with large expected signal contribution: $6 \leq N_{\text{jets}} \leq 7$ , $800 < M_J \leq 1000$ GeV (upper-left), $N_{\text{jets}} \geq 8$ , $800 < M_J \leq 1000$ GeV (upper-right), $6 \leq N_{\text{jets}} \leq 7$ , $M_J > 1000$ GeV (lower-left), and $N_{\text{jets}} \geq 8$ , $M_J > 1000$ GeV (lower-right). The expected signal distribution is also shown for a gluino mass of 1600 GeV. The ratio of data to post-fit yields is shown in the lower panel. The post-fit uncertainty is depicted as a hatched band. . . . .	111
11.3 Cross section upper limits at 95% CL for a model of gluino pair production with $\tilde{g} \rightarrow tbs$ compared to the gluino pair production cross section. The theoretical uncertainties in the cross section are shown as a band around the red line [16]. The expected limits (dashed line) and their $\pm 1$ s.d. and $\pm 2$ s.d. variations are shown as green and yellow bands, respectively. The observed limit is shown by the solid line with dots. . . . .	113

# List of Tables

2.1	The theoretical [17] and experimental [18, 19] values of the anomalous electron magnetic moment, $a_e$ . The uncertainty in the last digits is shown in parantheses. . . . .	6
3.1	The additional SUSY particles in the Minimal Supersymmetric Standard Model. . . . .	12
3.2	Rough estimates for the sizes of the $\lambda''_{ijk}$ MFV RPV couplings [20]. . . . .	20
5.1	Identification criteria that a PF electron must pass in order to be considered an analysis-level electron. . . . .	45
5.2	Identification criteria that a PF muon must pass in order to be considered an analysis-level muon. . . . .	47
5.3	Identification criteria that a jet candidate must pass in order to be considered an analysis-level jet. . . . .	50
6.1	Data samples analyzed for this analysis. The corresponding integrated luminosity is $35.9 \text{ fb}^{-1}$ . . . . .	60
6.2	Simulated background samples used in this analysis with their corresponding sample size and equivalent luminosity. . . . .	62
6.3	Simulated signal samples used in this analysis with their corresponding sample size and equivalent luminosity. . . . .	64
7.1	Expected yields in $35 \text{ fb}^{-1}$ from simulations of SM and signal processes. Rows above the horizontal line correspond to requirements in the baseline selection, while those below correspond to additional kinematic cuts. . . . .	67
9.1	Gluon splitting weights derived in the nominal fit, a variation with a requirement of $M_J > 800 \text{ GeV}$ , and 4 variations in bins of $N_{\text{jets}}$ (with the nominal $M_J > 500 \text{ GeV}$ requirement.) . . . . .	87
9.2	Comparison of the relative isolation distributions, as described in the caption of Figure 9.8, for electrons and muons between QCD and data with contributions from “all other” ( $t\bar{t}$ , $W + \text{jets}$ , and Other) subtracted. . . . .	94

9.3	The signal efficiency of the most sensitive bin ( $N_{\text{jets}} \geq 8$ , $M_J > 1000$ GeV) for a 1600 GeV gluino in various bins of the number of truth-level primary vertices. . . . .	97
10.1	Actual coverage probability of the 95% confidence interval of the fit for the mass points with a biased signal extraction. . . . .	100
10.2	Table comparing the post-fit normalizations of the control region fit to the pre-fit yields for the various background processes. . . . .	107
10.3	Table of post-fit pulls of the background-only and signal-plus-background control region fit. The last column, $\rho(\theta_i, \mu)$ , lists the correlation between the corresponding nuisance parameter, $\theta_i$ , and the nuisance parameter controlling the signal strength, $\mu$ . . . . .	108
11.1	Post-fit yields of the background-only fit, observed data, and expected yields for $m_{\tilde{g}} = 1600$ GeV. . . . .	112

# **Chapter 0**

## **Introduction for Non-technical Readers**

# **Chapter 1**

## **Introduction**

## **Part I**

# **Theoretical Context and Motivations**

# Chapter 2

## The Standard Model

### 2.1 Overview and Successes

The Standard Model (SM) of particle physics is a wildly successfull theory and one of the greatest accomplishments in science. Formulated in the second half of the 20th century, it describes 17 experimentally-observed, fundamental particles and their interactions through the electromagnetic, weak, and strong fundamental forces. These particles, shown in Figure 2.1, consist of six quarks and six leptons, known as fermions, which comprise the matter particles, along with four gauge bosons and one scalar boson, which mediate particle interactions.

Formally, the Standard Model is quantum field theory with symmetries described by the group  $SU_c(3) \times SU_L(2) \times U_Y(1)$  and with a Lagrangian of

$$\begin{aligned}\mathcal{L} = & -\frac{1}{4}F_{\mu\nu}F^{\mu\nu} + i\bar{\psi}_i \not{D} \psi_i + h.c. \\ & + \psi_i y_{ij} \psi_j \phi + h.c. + |D_\mu \phi|^2 - V(\phi),\end{aligned}$$

where  $F_{\mu\nu}$  is the field strength tensor,  $D_\mu$  is the gauge covariant derivative,  $\not{D} = \gamma^\mu D_\mu$ ,  $\psi_i$  are the fermion fields,  $\phi$  is the Higgs field,  $y_{ij}$  are the yukawa couplings, and h.c. is the hermitian conjugate of the term directly preceding it. In the top line, the first term

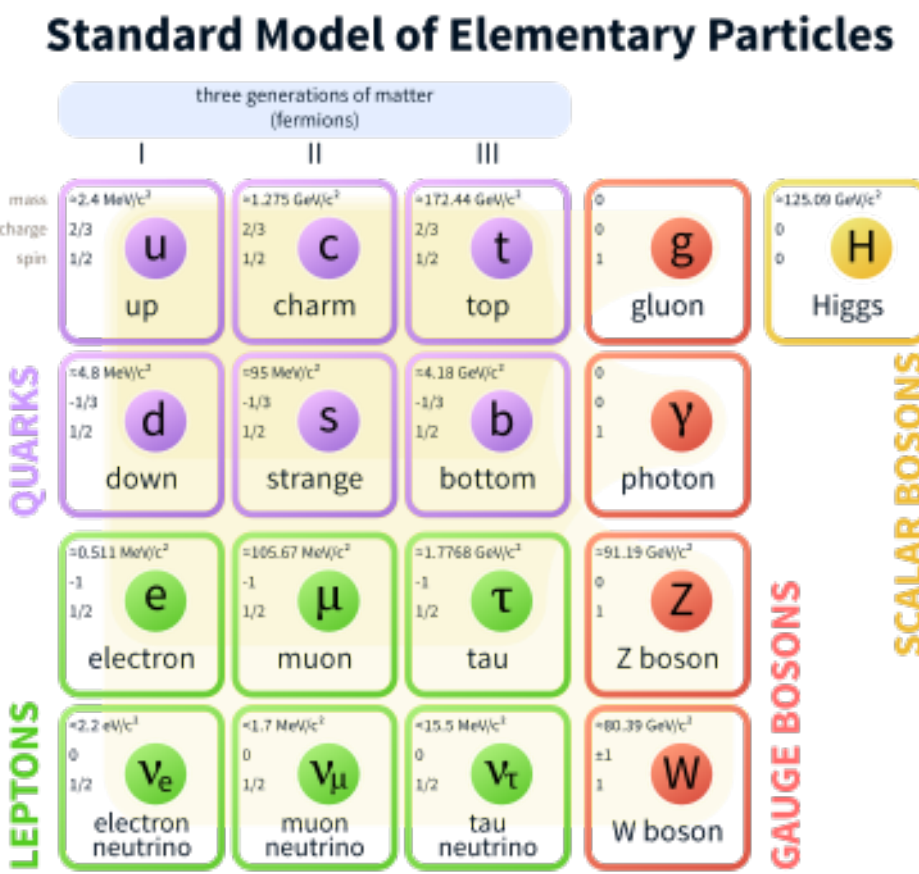


Figure 2.1: The fundamental particles of the Standard Model and some of their properties.

$a_e$ (Theory)	0.001 159 652 181 78(77)
$a_e$ (Experiment)	0.001 159 652 180 73(28)

Table 2.1: The theoretical [17] and experimental [18, 19] values of the anomalous electron magnetic moment,  $a_e$ . The uncertainty in the last digits is shown in parentheses.

of the Lagrangian describes the interactions of gauge bosons, while the second encodes the interactions between gauge bosons and fermions. The bottom line describes Higgs physics with the first term describing the Higgs-fermion interactions, the second term encoding the Higgs-gauge boson interactions, and finally, the third term representing the Higgs potential.

As the Standard Model is able to provide predictions across an enormous scope of physics, it has been rigorously tested throughout its history. For example, Figure 2.2, shows the agreement between the SM predictions and experimental results for the production cross section of a variety of processes. Amazingly, all of the measurements, spanning nine orders of magnitude, agree with SM predictions. At the same time, the Standard Model is the most precisely tested theory in physics with its prediction [17] of the anomalous electron magnetic moment incredibly agreeing with experimental measurements [18, 19] at up to fourteen decimal places, as shown in Table 2.1.

## 2.2 The Standard Model as an Incomplete Theory

Despite the impressive successes of the Standard Model, it is incomplete as a fundamental description of the universe and many tensions exist between it and both experimental and theoretical concerns. For example, the Standard Model glaringly leaves out the fundamental force of gravity and attempts to construct a theory of quantum gravity have been fraught with difficulties. Furthermore, the Standard Model is unable to explain the substantial astrophysical evidence for dark matter [21, 22], which comprises

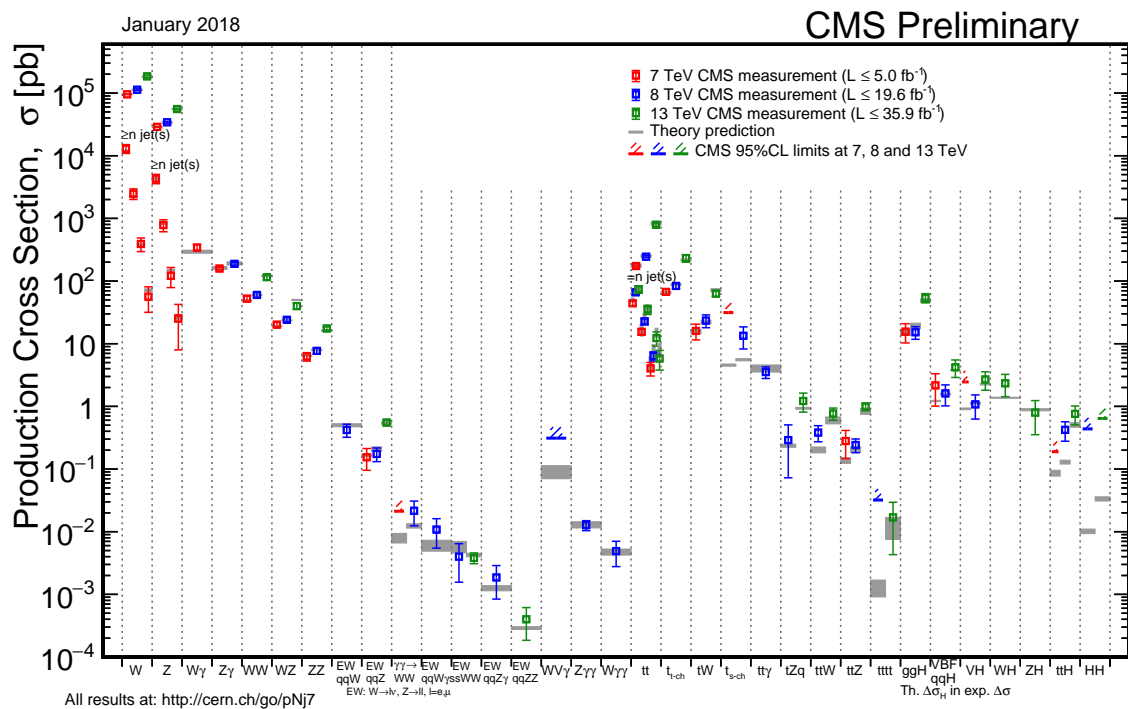


Figure 2.2: The theoretical and experimental value for the production cross section of various processes [1].

$\sim 80\%$  of the matter in the universe, as it has no suitable candidate that can account for the observed mass density of dark matter.

Additionally, the Standard Model provides no mechanisms for:

- the origin of neutrino masses
- the matter-antimatter symmetry
- the presence of dark energy
- a grand unified theory of the strong and electroweak forces

Because of these issues, the Standard Model is believed to be a low-energy effective field theory with new physics entering at higher energies. It is, however, not easy to know what form this new physics may take, and thus solutions to the above problems have been used to drive much of the theoretical framework for extending the Standard Model. In particular, the Hierarchy Problem and the idea of “naturalness”, described in the section below, are, perhaps, the most significant lampposts in the search for new physics.

### 2.2.1 The Hierarchy Problem and Naturalness

The long-awaited discovery of the Higgs boson [23, 24, 25, 26, 27, 28] confirmed the existence of a scalar boson with an observed mass of approximately 125 GeV. This relatively low mass of the Higgs boson, however, creates two related theoretical concerns. First, the Higgs mass is tied to the electroweak scale by the relation

$$v = \frac{m_h}{\sqrt{2}\lambda_h} \approx 246 \text{ GeV} \quad (2.1)$$

where  $v$  is the higgs vacuum expectation value (vev),  $m_H$  is the physical Higgs mass, and  $\lambda_h$  is the Higgs Yukawa coupling. The vev directly dictates the electroweak scale and is only on the order of 100 GeV. The next largest known energy scale is that of quantum gravity and is typically defined as the Planck mass, which is on the order of  $10^{19}$  GeV. The question as to why these two scales are so discrepant is known as the Hierarchy Problem [29].

The second question stems from trying to understand the observed mass of the Higgs boson in the presence of quantum corrections. The Higgs mass can be broken down into two components, its bare mass,  $m_{H,0}$ , and contributions from radiative corrections,  $\delta m_H^2$ , as shown in the equation below

$$m_h^2 = m_{H,0}^2 + \delta m_h^2. \quad (2.2)$$

As a scalar particle, the Higgs boson mass receives contributions from all massive particles, and in particular, for a fermion,  $f$ , the contribution to the Higgs mass at the one-loop level, corresponding to the diagram shown in Figure 2.3, is of the form

$$\begin{aligned} \delta m_h^2|_f &= -\frac{\lambda_f^2}{8\pi^2} N_f \int^{\Lambda_{UV}} \frac{d^4 p}{p^2} \\ &= -N_f \frac{\lambda_f^2}{8\pi^2} \left[ \Lambda_{UV}^2 - 6m_f^2 \ln \left( \frac{\Lambda_{UV}}{m_f} \right) + 2m_f^2 \right] + \mathcal{O} \left( \frac{1}{\Lambda^2} \right), \end{aligned} \quad (2.3)$$

with  $\lambda_f$  the Yukawa coupling and  $N_f$  the number of fermionic degrees of freedom. The quantity  $\Lambda_{UV}$  is the cutoff of the momentum integral, which represents the approximate scale at which the Standard Model is no longer valid. In the case that there is no new physics beyond the Standard Model, this would correspond to  $\Lambda_{UV} \sim$  Planck scale  $\sim 10^{19}$  GeV, where effects due to quantum gravity are introduced.

In this scenario, the leading term of the Higgs mass corrections is  $\mathcal{O}(10^{38} \text{ GeV}^2)$ ,

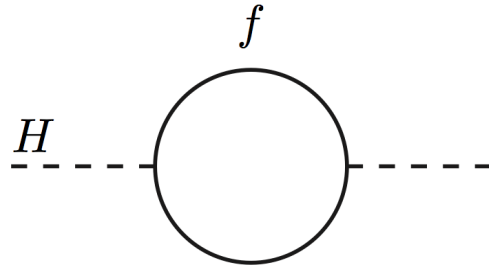


Figure 2.3: The fermionic one-loop Higgs mass correction.

while, as measured, the squared Higgs mass is only  $\mathcal{O}(10^4 \text{ GeV}^2)$ . For these two values to be consistent with each other, the Higgs bare mass parameter must exactly cancel the correction term at over 30 decimal places of precision. This high-level of fine-tuning is considered to be “unnatural” and has been deemed the Naturalness Problem [30, 31, 32, 33]. While it is entirely plausible that such a fine-tuned cancellation of parameters occurs – there is no inherent theoretical reason against this, this problem motivates the need for new physics below the Planck scale, particularly physics that naturally incorporates a mechanism for cancelling the quadratic divergence of the  $\Lambda_{UV}^2$  term.

# Chapter 3

## Supersymmetry

### 3.1 Natural Supersymmetry

Supersymmetry (SUSY) is an extension of the Standard Model that introduces a new symmetry that relates fermionic and bosonic degrees of freedoms [34, 35, 36, 37, 38, 39, 40, 41, 42, 43]. This symmetry imposes that for every fermionic degree of freedom in the Standard Model, there exists a “superpartner” bosonic degree of freedom, and vice versa. Furthermore, this symmetry dictates that both sets of particles couple to physics at the  $\Lambda_{UV}$  scale identitically.

In the Minimal Supersymmetric Standard Model (MSSM) [44], the Standard Model is extended to include a Higgs sector comprised of two scalar doublets and only the SM superpartners. The superpartners of fermions are scalars and labeled by prefixing an “s” to the beginning of the corresponding SM particle name, while the superpartners of fermions are spin-1/2, labeled by suffixing an “ino” to the end of the corresponding SM particle name, and collecticely known as gauginos. Thus, the SUSY particles consist of 4 higgsinos, 12 squarks, 9 sleptons, and 7 gauginos, where there are 2 scalar particles for each SM fermion in order to preserve the number of degrees of freedom. The superpartners of SM particles are not necesarily mass eigenstates and can mix. The gauge and mass eigenstates of the superpartners, along with their properties, are shown in Table 3.1.

Name	Spin	Gauge Eigenstates	Mass Eigenstates
Higgs bosons	0	$H_u^0 H_d^0 H_d^+ H_d^-$	$h^0 H^0 A^0 H^\pm$
squarks	0	$\tilde{u}_L \tilde{u}_R \tilde{d}_L \tilde{d}_R$ $\tilde{c}_L \tilde{c}_R \tilde{s}_L \tilde{s}_R$ $\tilde{t}_L \tilde{t}_R \tilde{b}_L \tilde{b}_R$	same same $\tilde{t}_1 \tilde{t}_2 \tilde{b}_1 \tilde{b}_2$
sleptons	0	$\tilde{e}_L \tilde{e}_R \tilde{\nu}_e$ $\tilde{\mu}_L \tilde{\mu}_R \tilde{\nu}_\mu$ $\tilde{\tau}_L \tilde{\tau}_R \tilde{\nu}_\tau$	same same $\tilde{\tau}_1 \tilde{\tau}_2 \tilde{\nu}_\tau$
neutralinos	1/2	$\tilde{B}^0 \tilde{W}^0 \tilde{H}_u^0 \tilde{H}_d^0$	$\tilde{N}_1 \tilde{N}_2 \tilde{N}_3 \tilde{N}_4$
charginos	1/2	$\tilde{W}^\pm \tilde{H}_u^+ \tilde{H}_d^-$	$\tilde{C}_1^\pm \tilde{C}_2^\pm$
gluino	1/2	$\tilde{g}$	same

Table 3.1: The additional SUSY particles in the Minimal Supersymmetric Standard Model.

With the addition of these superpartners, a mechanism for naturally cancelling the radiative corrections to the Higgs mass is apparent, as the Higgs couples to these new massive particles as well, providing additonal radiative corrections that cancel the SM contributions. For example, for a fermion  $f$ , the radiative corrections from the corresponding sfermion  $\tilde{f}$ , shown in Figure 3.1, take the form

$$\delta m_h^2|_{\tilde{f}} = + N_{\tilde{f}} \frac{\lambda_{\tilde{f}}}{8\pi^2} \left[ -\Lambda_{UV}^2 + 2m_{\tilde{f}}^2 \ln \left( \frac{\Lambda_{UV}}{m_{\tilde{f}}} \right) \right] - N_{\tilde{f}} \frac{\lambda_{\tilde{f}}}{8\pi^2} \left[ -2m_f^2 + 4m_f^2 \ln \left( \frac{\Lambda_{UV}}{m_{\tilde{f}}} \right) \right] + \mathcal{O} \frac{1}{\Lambda_{UV}^2} \quad (3.1)$$

using the relation  $\sqrt{2}m_f = \lambda_f \nu$ . Supersymmetry imposes that  $N_{\tilde{f}} = N_f$  and  $\lambda_{\tilde{f}} = -\lambda_f^2$ , and thus, in the case where  $m_f = m_{\tilde{f}}$ , this perfectly cancels not only the quadratic divergence in Equation 2.3 but also the higher-order corrections, solving the Hierarchy Problem.

Of course, no superparticles have been observed at the SM scale. This, however, does not imply that supersymmetry is incorrect but only that if it exists, it is a broken symmetry. In this scenario where  $m_f \neq m_{\tilde{f}}$ , the quadratically divergent terms still cancel

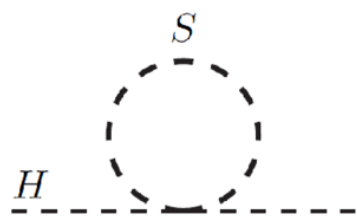


Figure 3.1: The scalar one-loop Higgs mass correction.

and what is left is only a logarithmic divergence, mediated by the squared mass difference of the partner particles:

$$\delta m_h^2 = N_f \frac{\lambda_s}{8\pi^2} \left( m_f^2 - m_{\tilde{f}}^2 \right) \ln \left( \frac{\Lambda_{UV}}{m_{\tilde{f}}} \right) + \dots . \quad (3.2)$$

This squared mass difference defines the degree to which the Higgs mass is fine-tuned.

## 3.2 Phenemonological and Experimental Constraints

While there is no theoretical prediction for the mass of the supersymmetric particles, there are certain guidelines for what the scale of these masses should be for a given level of fine-tuning that is deemed acceptable. Firstly, the Higgsino masses are directly controlled by the value of  $\mu$ , which is related to the electroweak scale by

$$-\frac{m_Z}{2} = m_h^2 + |\mu|^2, \quad (3.3)$$

indicating that the Higgsino masses must be near the electroweak scale,  $\sim 200$  GeV, in order avoid a large fine-tuning of parameters.

The other superparticle masses are constrained by the size of their contributions to the Higgs mass, described in Equation 3.2. Not all superparticles, however, contribute equally to the Higgs mass, and thus the phenemonological constraints for paricles are proportional to the size of their correction to the Higgs mass. The largest constraint is on the stop squark masses due to the large Yukawa coupling of the top quark, which implies that the stop masses must be relatively light in order to keep the squared mass difference small and correspondingly the overall contribution small. This also constrains the mass of the left-handed sbottom squark as it is in a doublet with  $\tilde{t}_L$  and thus must not be much heavier. Finally, the gluino couples to the squarks at the one-loop level,

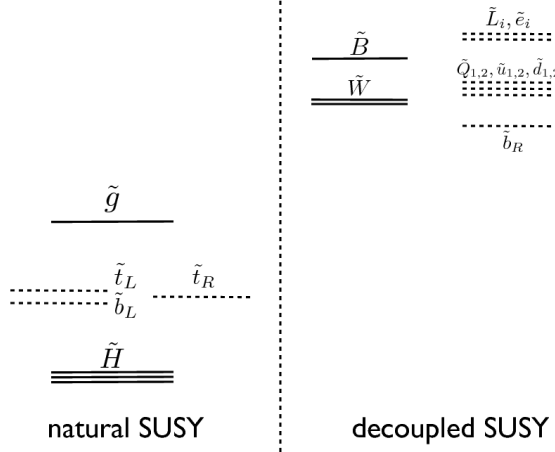


Figure 3.2: An example spectrum for natural SUSY.

which means it still couples to the Higgs boson at the two-loop order, despite the Yukawa coupling for a gluon being zero. This constraint on the gluino is looser than for other particles described, but as it is strongly interacting, it has a high cross section at the Large Hadron Collider (LHC) and is thus an important experimentally accessible one. Not considering model-dependent concerns, these are generically the only SUSY particles that are required to be light, and the rest of the superparticles may be decoupled at very high energies. A qualitative example of a natural SUSY spectrum is shown in Figure 3.2.

In order to gain a rough quantitative sense of what the mass constraints for these particles are, a measure of the Higgs mass fine-tuning can be constructed as

$$\mathcal{N} \equiv \frac{\delta m_h^2}{m_h^2}. \quad (3.4)$$

Thus for  $\mathcal{N} = 10$ , a fine tuning of 1 part in 10, gives bounds of  $m_{\tilde{t}} \lesssim 1$  TeV, correspondingly  $m_{\tilde{b}} \lesssim 1$  TeV, and  $m_{\tilde{g}} \lesssim 2$  TeV.

Recent results from the LHC, however, are already starting to threaten these bounds,

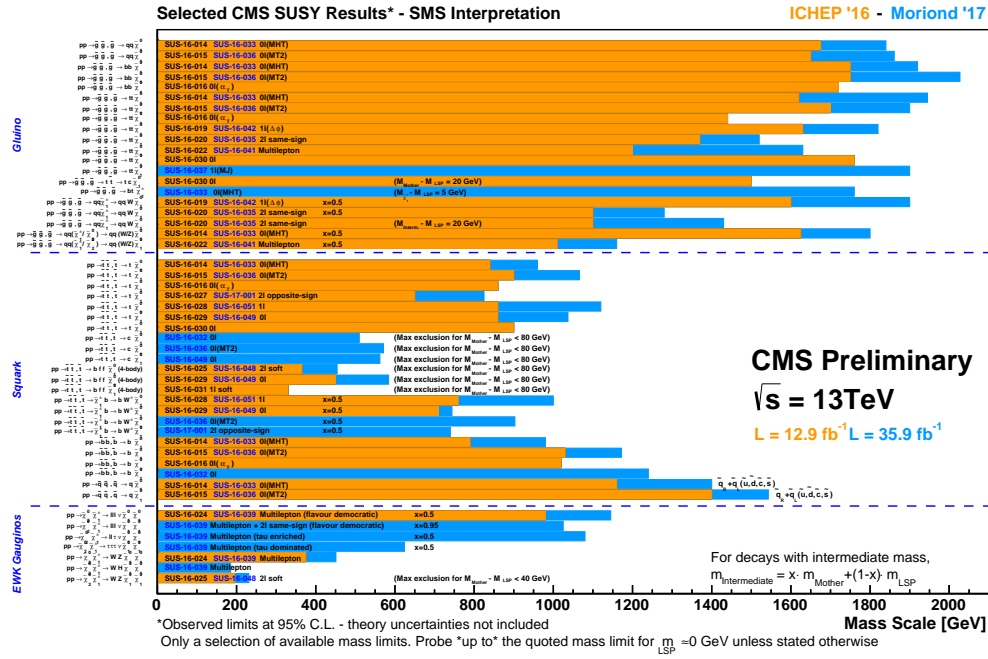


Figure 3.3: An overview of recent results from SUSY searches from the Compact Muon Solenoid experiment [2].

as shown in Figure 3.3 and Figure 3.4, with gluino and stop exclusion limits already surpassing these bounds for certain models. These constraints, however, are largely in the context of  $R$ -parity conserving models, where a new quantum number,  $R$ , is conserved.  $R$ -parity is defined per particle as

$$P_R \equiv (-1)^{3(B-L)+2s}, \quad (3.5)$$

where  $B$ ,  $L$ , and  $s$  is the baryon number, lepton number, and spin of the particle,  $P_R = +1$  for SM particles and  $P_R = -1$  for SUSY particles. The motivation for requiring that  $R$ -parity be conserved is that, in this case, the lightest supersymmetric particle (LSP) cannot decay to SM particles and is therefore stable. For models where the LSP is a neutralino, the LSP is then a strong dark matter candidate.

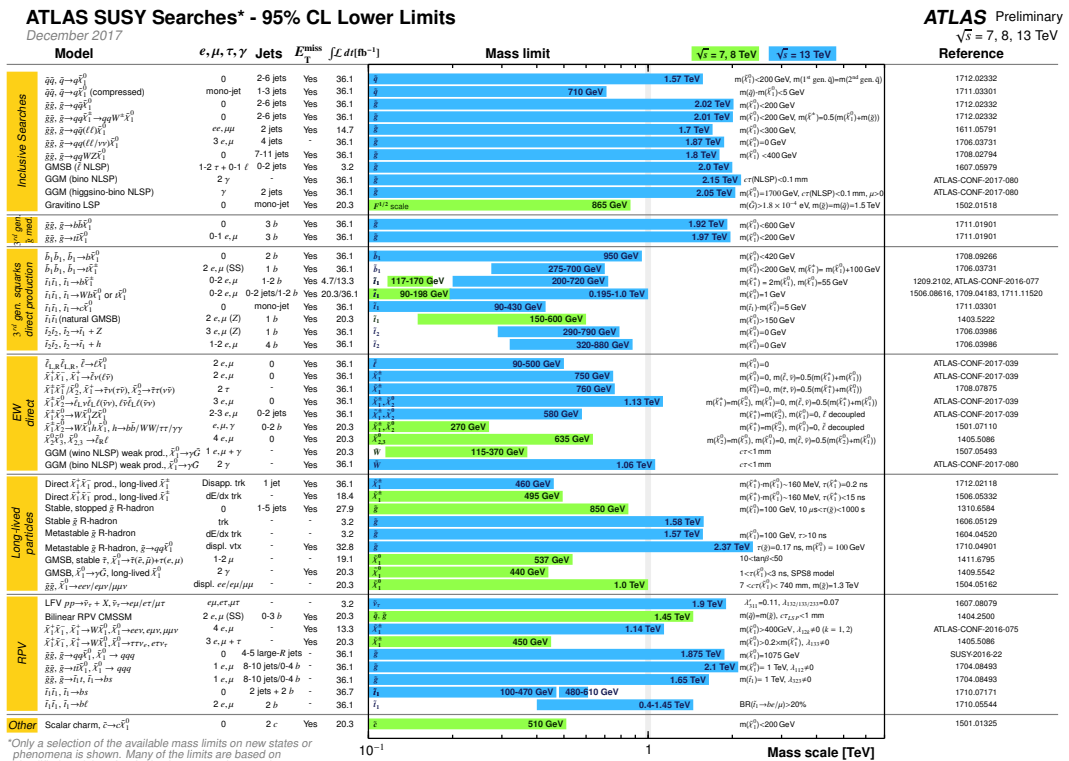


Figure 3.4: An overview of recent results from SUSY searches from the ATLAS experiment [3].

The phenomenology, however, for  $R$ -parity conserving (RPC) and  $R$ -parity violating (RPV) SUSY models is very different. For RPC scenarios, the stable LSP does not interact with the detector and escapes without depositing any energy. The presence of the LSPs, however, can be inferred by examining the missing transverse momentum in an event, which due to momentum conservation and the negligible transverse momentum of the initial colliding particles, should be 0 in events without LSPs or neutrinos. Thus, the  $E_T^{\text{miss}}$  in an event provides a powerful handle for discriminating signal and background and most analyses search for signatures that include significant amounts of  $E_T^{\text{miss}}$ . In RPV models, however, the LSP is not stable and decays to SM particles, which does not produce a large  $E_T^{\text{miss}}$  signature. Although this disfavor the LSP as a dark matter candidate, it allows RPV models to evade the constraints from RPC searches. Subsequently, RPV SUSY yields an important class of models that can ease the tension between natural solutions to the hierarchy problem and current experimental limits.

### 3.3 $R$ -parity violating Supersymmetry

In the MSSM, the additional  $R$ -parity violating terms are

$$W_{\text{RPV}} = \frac{1}{2} \lambda^{ijk} L_i L_j \bar{e}_k + \lambda'^{ijk} L_i Q_j \bar{d}_k + \frac{1}{2} \lambda''^{ijk} \bar{u}_i \bar{d}_j \bar{d}_k + \mu'^i L_i H_u, \quad (3.6)$$

where the color indices have been suppressed, the letters  $i, j, k$  denote generation. The fields  $L_i$ ,  $Q_j$ , and  $H_u$  are SU(2) doublets corresponding to leptons, quarks, and the Higgs boson, respectively, while  $\bar{e}_k$ ,  $u_i$ , and  $d_j$  are the charged lepton, up-type quark, and down-type quark SU(2) singlets. The  $\mu$  and various  $\lambda$  factors are coupling strengths for their corresponding interactions, where  $\lambda$  and  $\lambda''$  must be antisymmetric in their first and last two indices, respectively, due to gauge invariance. A full description of RPV SUSY can

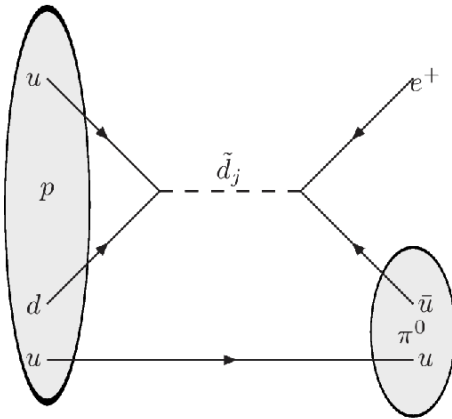


Figure 3.5: Example diagram representing proton decay, where the particle  $\tilde{d}_j$  represents a down-type squark [4]. The left vertex is mediated by the baryon number violating coupling,  $\lambda''$ , and the right vertex is mediated by the lepton number violating coupling,  $\lambda'$ .

be found in Reference [45].

While there is no fundamental theoretical reason forbidding  $R$ -parity violation, there are significant constraints on these interactions, primarily due to the lepton number violating (LNV) and baryon number violating (BNV) nature of the  $\lambda$ ,  $\lambda'$  and  $\lambda''$  couplings, respectively [46]. The most stringent of these constraints is from proton decay on which current experimental results place a lower bound on the proton half-life of  $\mathcal{O}(10^{34}$  years) [47, 48]. Proton decay, however, requires both a lepton number and baryon number violating coupling, as shown in Figure 3.5. These constraint can be avoided if a mechanism exists to make one of these couplings zero or negligibly small. Though, there are additional strong limits on the individual LNV and BNV couplings, for example from neutron oscillation and muon-to-electron decay measurements, which are most stringent for the light generations. Thus, for any mechanism to evade these constraints, it must also motivate smaller couplings for the lighter generations.

	$ds$	$db$	$bs$
$u$	$3 \times 10^{-12}$	$6 \times 10^{-9}$	$5 \times 10^{-7}$
$c$	$1 \times 10^8$	$1 \times 10^{-5}$	$4 \times 10^{-5}$
$t$	$4 \times 10^{-5}$	$6 \times 10^{-5}$	$2 \times 10^{-4}$

Table 3.2: Rough estimates for the sizes of the  $\lambda''_{ijk}$  MFV RPV couplings [20].

### 3.3.1 Mimimal Flavor Violating Supersymmetry

One way to avoid the constraints placed on the RPV couplings is to construct a model by following the structure of minimal flavor violation. In these Minimal Flavor Volating (MFV) SUSY models [49, 50, 20], the RPV couplings are related to the SM Yukawa couplings, making the third generation RPV couplings large and those of the first two small. For example, the  $\lambda''$  coupling can be written as

$$\lambda''_{ijk} = w'' y_i^{(u)} y_j^{(d)} y_k^{(d)} \epsilon_{ijk} V_{il}^* \quad (3.7)$$

with  $w''$  an  $\mathcal{O}(1)$  parameter and  $y^{(u)}$  and  $y^{(d)}$  the up- and down-type Yukawa couplings. From this, the sizes of the  $\lambda''_{ijk}$  couplings can be roughly estimated (using  $w'' = 1$ ) are shown in Table 3.2, which depicts the dependence of the coupling strength on generation. Additionally, in MFV scenarios, the LNV couplings are severely suppressed by neutrino masses, and in the limit of massless neutrinos, are exactly zero. Thus, the only relevant RPV coupling in MFV SUSY models is the BNV  $\bar{u}\bar{d}d$  coupling, which is small for the first two generations – meeting the exact criteria necessary to evade experimental constraints on RPV couplings. Furthermore, in the case where the LSP is a squark, it will decay promptly and not produce  $E_T^{\text{miss}}$ , allowing these models to even evade the constraints placed on results from RPC SUSY searches.

Because of these considerations, MFV SUSY is an intriguing class of models to investigate experimentally. In particular, due to the high  $\tilde{g}\tilde{g}$  cross-section and large value of

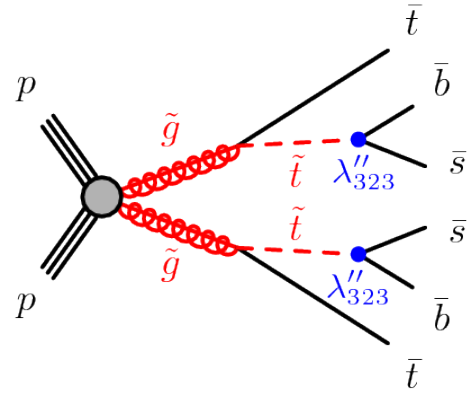


Figure 3.6: Example diagram of the pair production of gluinos that decay via  $\tilde{g} \rightarrow t\bar{t} \rightarrow tbs$ .

$\lambda''_{tbs}$ , a search for the pair-production of gluinos that decay via  $\tilde{g} \rightarrow t\bar{t} \rightarrow tbs$ , as shown in Figure 3.6, is well-motivated.

The remainder of this dissertation is dedicated to describing such a search conducted with the Compact Muon Solenoid detector using  $\sqrt{s} = 13$  TeV  $pp$  collisions.

## **Part II**

### **Experimental Apparatus**

# Chapter 4

## Experimental Apparatus

While the Large Hadron Collider was approved over 20 years ago, much of its design was influenced by the needs of searches for physics beyond the Standard Model (BSM). The two most important properties of a collider, for a BSM search, are its center-of-mass energy and its (instantaneous) luminosity, both of which were designed to be higher than any previous experiment. The designed center-of-mass energy ( $\sqrt{s}$ ) of 14 TeV allows for the production of particles heavier than ever previously, while the designed luminosity of  $10^{34} \text{ cm}^{-2}\text{s}^{-1}$  allows BSM searches to probe very rare processes.

In the same way, the design of the Compact Muon Solenoid (CMS) detector reflects the needs of BSM searches. In particular, to fully search the uncovered parameter space of new physics an all-purpose, hermitic detector that can precisely measure a variety of particles and reliably determine the MET in an event is needed to cover the many (un)theorized new physics models.

This chapter summarizes in more detail the major features of both the LHC and CMS. A complete description of both can be found in Refs.[INCLUDE].

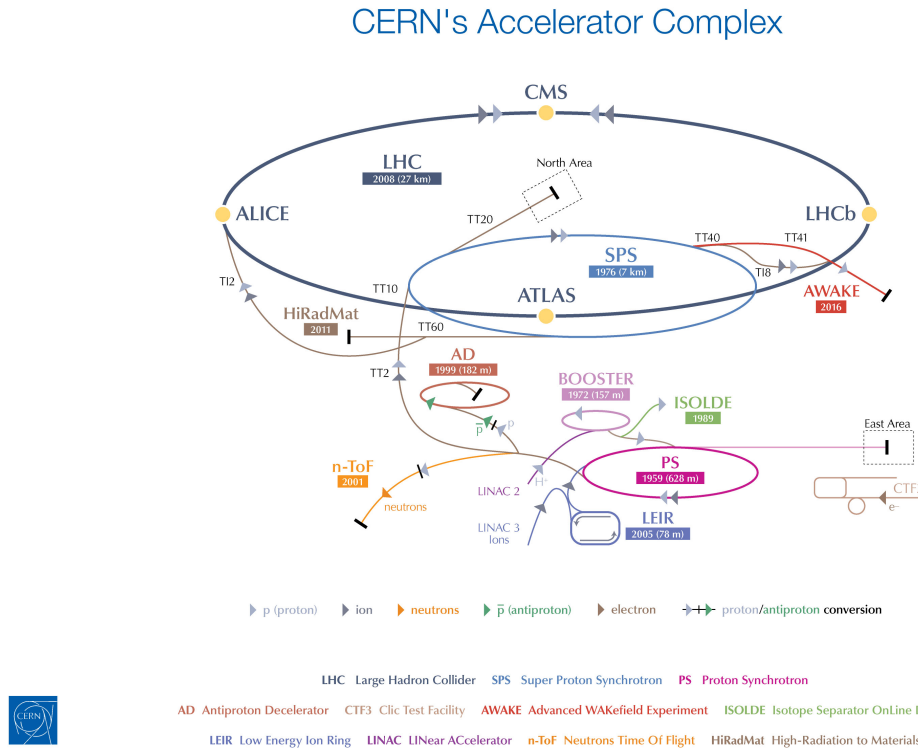


Figure 4.1: A schematic of the CERN LHC accelerator complex. [5]

## 4.1 The Large Hadron Collider

The LHC since 2015 has been colliding protons together at  $\sqrt{s} = 13$  TeV, slightly below the designed specifications but still at an unsurpassed energy. In order to reach this center-of-mass energy, the LHC uses a large accelerator complex consisting of a succession of many smaller particle accelerators, which is necessary to produce protons and bring them up to a speed such that they can be injected into the LHC ring. A diagram of the CERN accelerator complex is shown in Figure 4.1.

This process first begins with a simple bottle of hydrogen gas, which are ionized by an electric field to produce the needed protons. These resulting protons are then fed into LINAC 2, the first accelerator in the chain, which accelerates them up to 50 MeV,

creating a beam of protons. The proton beam is then passed successively to the Proton Synchtron Booster, Proton Synchotron, and Super Proton Synchtron, where the beam reaches energies of 1.4 GeV, 25 GeV and 450 GeV, respectively. At the Proton Synchotron, the beams are additionally split into “bunches”, each consisting of  $O(10^{11})$  protons and separated in time by 25 ns. Finally, the protons can be injected into the two beam pipes of the LHC, each circulating in opposite directions. These beams continue to be accelerated until they reach their final energy of 6.5 TeV, allowing for collisions at  $\sqrt{s} = 13$  TeV. At this point, the proton beams are focused and fine-tuned at several stages in order to increase the luminosity. In 2016, the LHC was able to collide protons with an instantaneous luminosity of  $1.4 \times 10^{34}$  cm $^{-2}$ s $^{-1}$ , exceeding its designed specification, and deliver a record-high integrated luminosity of 41.07 fb $^{-1}$ .

These improvements from previous generations of colliders greatly increase the reach of searches for new, heavy particles. Since the center-of-mass energy of the actual colliding partons ( $\sqrt{\hat{s}}$ ) is typically much less than the overall center-of-mass energy, raising the collider’s energy can greatly increase the production cross-section of heavy particles, especially of those around the TeV scale. For example, Figure 4.2, which depicts the ratio of parton luminosities at  $\sqrt{s} = 13$  TeV and 8 TeV as a function of the characteristic mass scale of the event, shows that a 2000 GeV gluino will be produced through  $gg$  scattering processes  $\sim 15\times$  more often with less than a doubling of the collider energy. Increasing a collider’s energy, however, is not always a practical option, involving new technologies, expensive upgrades, or even a new collider. When this is the case, the best alternative to continue to probe rare processes is to simply take more data, more quickly, which a high luminosity collider like the LHC allows for.

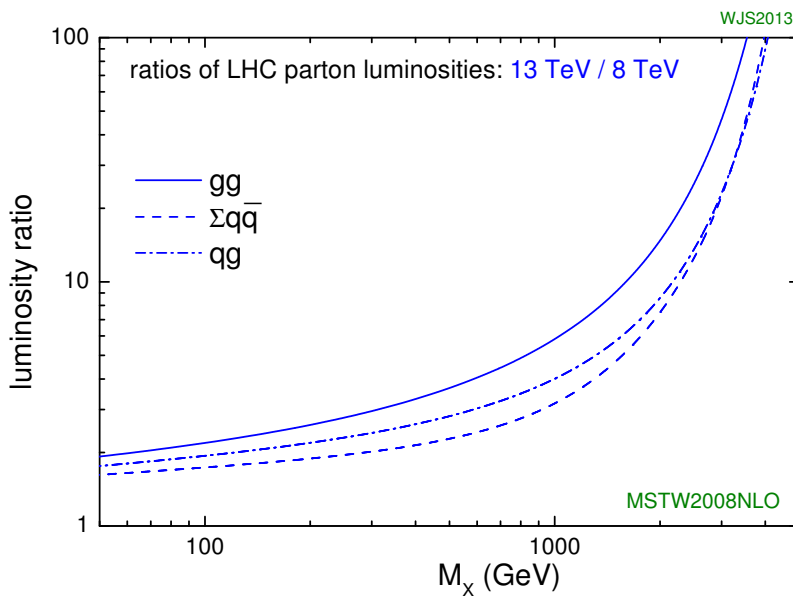


Figure 4.2: Ratio of parton luminosities at  $\sqrt{s} = 13$  and 8 TeV. [6]

## 4.2 Compact Muon Solenoid

Along the tunnels of the LHC, below Cessy, France, sits the CMS detector where the proton-proton collisions are recorded. The overall shape of the detector is cylindrical with a length of 21.6 m and radius of 7.3 m, while weighing roughly 14,000 metric tons. The CMS detector is sometimes called a cylindrical onion, as this shape is constructed through layers of specialized detectors, each designed to provide precise measurements for a particular particle type. Peeling back the layers from the outside-in, the first sub-detector is the muon system. Next is a superconducting solenoid of 6 m internal diameter that produces a magnetic field of 3.8 T, and perhaps most importantly provides the “S” in CMS. Placed within the solenoidal magnet, is the rest of the CMS detector, namely the Hadronical Calorimeter (HCAL), Electromagnetic Calorimeter (ECAL), and a silicon tracker. The design of fitting most of the detector components within the solenoid is

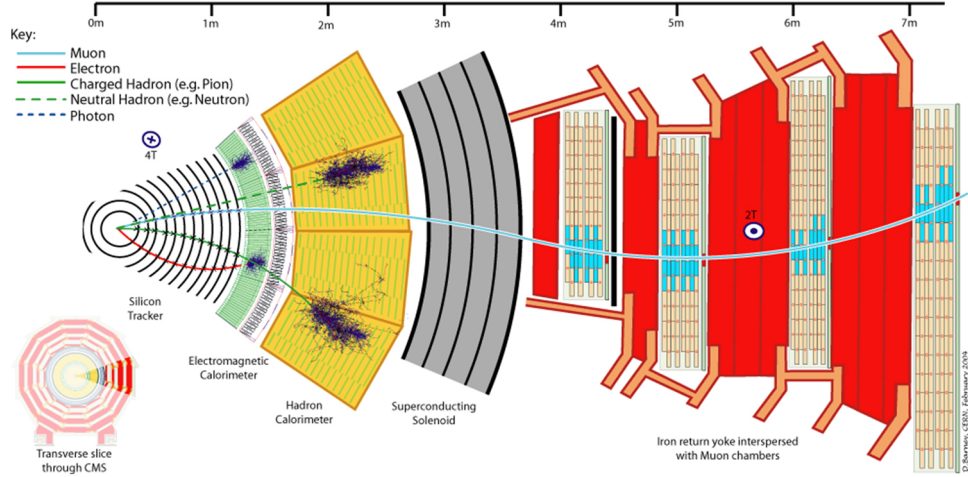


Figure 4.3: A diagram showing the various sub-detectors of the CMS detector. [7]

responsible for the “C” in CMS. A diagram of the layout of the CMS detector can be seen in Figure 4.3.

At the center of the silicon tracker is Interaction Point 5, the beam crossing which provides the proton-proton collisions to the CMS detector, and is the nominal origin of CMS’s coordinate system. The  $x$ -axis is defined to point towards the center of the LHC ring and the  $y$ -axis is defined to point up towards the surface, both of which are transverse to the proton beam. The  $z$ -axis points along the beamline with the positive direction given by the right-hand rule relative to the  $x$ - and  $y$ -axes. Due to CMS detector shape, it is often useful to convert the cartesian coordinates to a cylindrical coordinate system. In this system, the azimuthal angle,  $\phi$ , is measured from the  $x$ -axis in the  $xy$ -plane, and the polar angle,  $\theta$ , is measured from the  $z$ -axis. The polar angle, however, is often replaced by pseudorapidity, defined as  $\eta = -\ln(\theta/2)$ . Thus, any point in the CMS coordinate system can be represented by  $(z, \eta, \phi)$ . A diagram showing both the cartesian and cylindrical coordinate systems can be seen in Figure 4.4.

The remainder of this section briefly describes the main features of the various CMS sub-detectors.

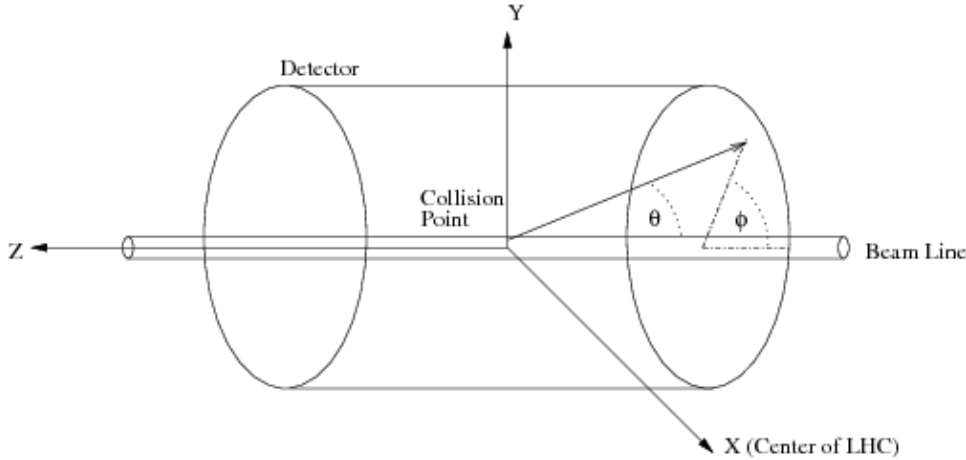


Figure 4.4: A diagram of the cartesian and cylindrical coordinate systems used by CMS. [8]

### 4.2.1 Inner Tracking System

The tracking system is used for precise measurements of the trajectories of charged particles, as well as reconstruction of secondary vertices. As the tracking system is the closest subdetector to the interaction point, it faces a very large particle flux rate and so must be able to provide both high granularity and fast response, as well be able to survive operating in those conditions with an expected lifetime of 10 years. At the same time, these features must be balanced with minimizing the amount of material in order to reduce unwanted interactions with the detector, such as multiple scattering, photon conversion, and nuclear interactions. These requirements lead to a tracking system composed entirely of silicon technology.

The CMS tracking system is actually composed of two parts. The first is the pixel detector, which surrounds the interaction point, and is composed of 3 barrel layers at radii between 4.4 and 10.2 cm and 2 endcap layers that extend the acceptance up to  $|\eta| < 2.5$ . In total, the pixel detector covers an area of roughly  $1 \text{ m}^2$  with 66 million pixels and achieves a resolution of roughly 10 and 20 microns in the directions transverse and longitudinal to the beam line, respectively.

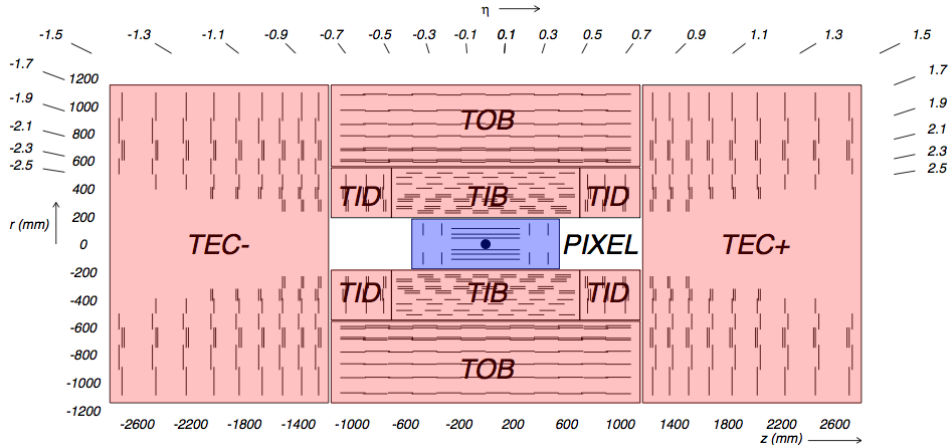


Figure 4.5: Layout of the CMS tracking system, showing both the pixel detector (blue) and the strips detector (red). [9]

The second part of the tracking system is the strips detector which sits just outside the pixel detector. The strips detector is composed of 4 parts: the tracker inner barrel (TIB), tracker inner disks (TID), tracker outer barrel (TOB), and the tracker endcaps (TEC). The TIB and TID extend up to 55 cm in radius and are composed of 4 and 3 layers, respectively, while the TOB, which surrounds the TIB and TID, extends out to 116 cm and is composed of 6 layers. Lastly, the TEC which sits next to the other strip detector components, covers a radius of 22.5 to 113.5 cm and is composed of 9 disks. In total, the strips detector covers an area of  $198 \text{ m}^2$  with 9.3 million strips. A layout of the tracking system including the pixel and strips detector is shown in Figure 4.5.

#### 4.2.2 Electromagnetic Calorimeter

The primary purpose of the electromagnetic calorimeter (ECAL) is to measure the energy of electrons and photons. The ECAL is a hermetic, hemogenous detector made up of a barrel part, covering the  $|\eta| < 1.479$  region, and two endcap parts that cover  $1.566 < |\eta| < 3.0$ . Both the barrel and endcap sections are comprised of lead tungstate

( $PbWO_4$ ) crystals with 61,200 in the barrel and 7,324 in each of the endcaps. The use of the  $PbWO_4$  crystals was motivated by their high density, short radiation length, small Molière radius, and radiation hardness, all of which allow for a fine granularity, radiation resistant, compact calorimeter.

The lead tungstate crystals act as scintillators, which produce an amount of light that is proportional to the energy of an incident particle. This light is then converted to an electrical signal by silicon photodetectors (avalanche photodetectors in the barrel and vacuum hototriodes in the endcaps), which is used for the final energy measurement. The resulting resolution on the energy measurements is given by

$$\frac{\sigma}{E} = \frac{S}{\sqrt{E}} \oplus \frac{N}{E} \oplus C \quad (4.1)$$

where  $S$  is the stochastic term,  $N$  the noise term,  $C$  the constant term, and  $E$  is in units of GeV. Typical values for  $S$ ,  $N$ , and  $C$ , as measured in electron beam tests, are 2.8%, 12%, and 0.30%, respectively.

In addition to the ECAL barrel and endcaps is a preshower detector, which sits in front of the endcaps, covering  $1.653 < |\eta| < 2.6$ . The main purpose of the preshower detector is to identify neutral pions by improving the granularity, so as to be able to resolve photon pairs from the decay of high energy pions that otherwise would be mis-measured as single photons. The preshower detector also provides improved position resolution for electrons and photons and helps identify electrons from minimum ionizing particles. The full layout of the ECAL is shown in Figure 4.6.

### 4.2.3 Hadronic Calorimeter

The primary purpose of the hadronic calorimeter (HCAL) is to measure the energy of hadrons, which can pass through the ECAL as they primarily interact through the

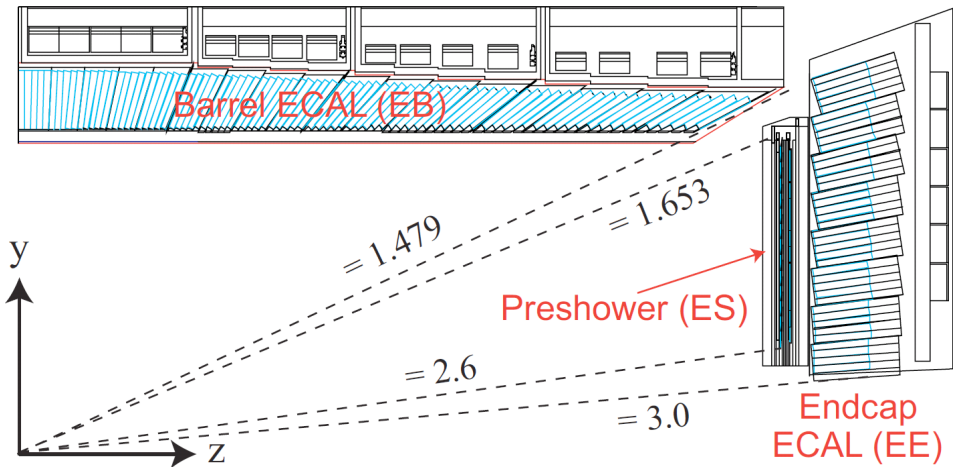


Figure 4.6: A cross section of the ECAL, showing its geometry and layout. [10]

strong force. The HCAL is a sampling calorimeter made up of either brass, iron, or steel absorbers and uses plastic scintillator tiles as the sampling material, which measures the energy of hadrons through scintillation, similarly to the ECAL: As a hadron reaches through the HCAL, it interacts with one of the absorber layers, which results into a “shower” of particles that produces light in the scintillator tiles as the resulting particles pass through the sampling layers. These light pulses are converted to electrical signals by optical fibers, which when summed have an amplitude proportional to the hadron’s energy.

The HCAL is separated into 4 components: the hadron barrel (HB), hadron endcap (HE), hadron forward (HF), and hadron outer (HO), the layouts of which are shown in Figure 4.7. The HB and HE completely surround the ECAL and were designed to minimize any cracks between the two subdetectors with the HB covering  $|\eta| < 1.3$  and the HE covering the rest up to  $|\eta| = 3$ . Both components function as sampling calorimeters with alternating absorber and sampling layers. In the HB, the first and last layers are made of steel while the 14 other absorber layers are made of brass, while the HE is made

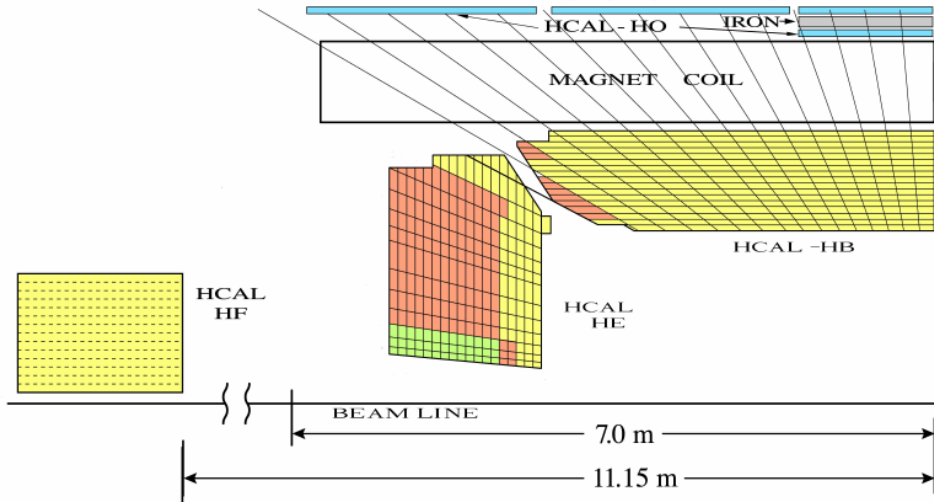


Figure 4.7: The layout and geometry of a quarter of the HCAL detector. [11]

up of 18 brass absorber layers. For both components, there are sampling layers made of plastic scintillator tiles interspersed between each of the absorber layers.

The HF is used to measure the energy of the forward most hadrons in the pseudo-rapidity range of  $3.0 < |\eta| < 5.0$ . At this forward position, the HF faces extraordinary levels of particle flux and had to be designed to handle this radiation. Due to this constraint, the HF uses quartz fibers instead of plastic scintillator tiles as its active medium, as the quartz fiber are more radiation hard. The HF uses both long fibers, which run the full depth (165 cm) of the detector, and short fibers, which begin 22 cm from the front end of the detector. This geometry allows the HF to provide depth information of the energy deposits, which helps to identify electron and photons from hadrons, as the former tends to deposit most of its energy in the first depth, while the latter deposits its energy more equally between the two depths. These fibers are embedded into the steel structure of the HF, which also acts as the absorber.

Lastly is the HO, whose main purpose is to act as a “tail catcher”. Due to the geometrical constraint that the HCAL fit within the CMS solenoid, the HB does not

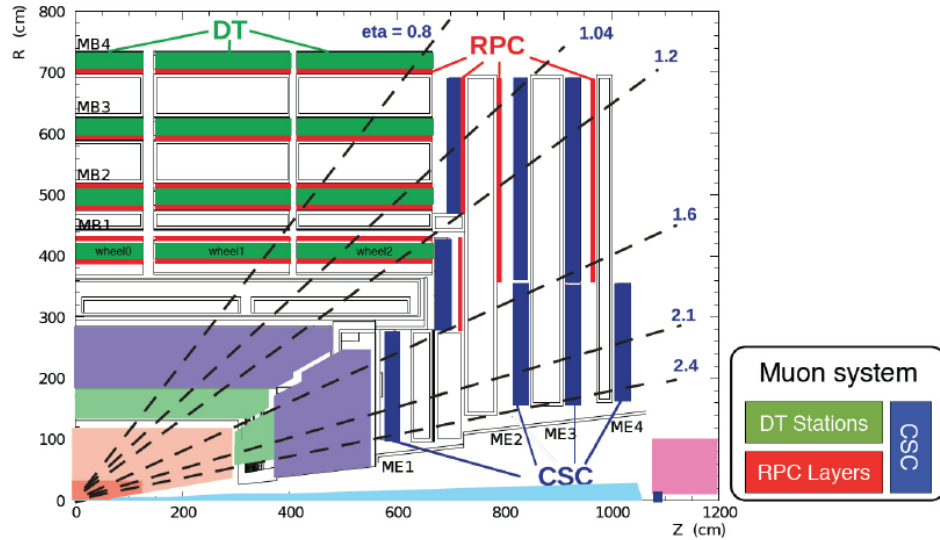


Figure 4.8: The layout of the muon system within the CMS detector. [12]

have enough material in the central  $\eta$  region to adequately contain hadron showers. So to provide extra sampling layers, the HO sits just beyond the solenoid and has 1 to 2 scintillator layers and uses the magnet as an extra absorber layer. At this position, the HO is able to identify late starting showers and measure the amount of energy that is deposited past the HB.

#### 4.2.4 Muon System

Muons, as implied by the “M” in CMS, are a central focus of the CMS detector, and the responsibility of identifying muons with high purity and providing precise momenta measurements falls to the muon system. To do this, the muon system is composed of three types of gaseous detectors, motivated by the need to cover a large area and varying radiation environments. Figure 4.8 shows the layout of the muon system within the CMS detector.

In the barrel region,  $|\eta| < 1.2$ , drift tube chambers (DTs) are used as the neutron-

induced background is small, the muon rate is small, and the magnetic field is uniform. The DTs are organized into 4 stations, with three of the stations containing 8 chambers that measure position in the  $r - \phi$  plane and 4 that measure position in the  $z$ -direction. The last station only contains the 8  $r - \phi$  measuring chambers. In the endcap regions of CMS,  $0.9 < |\eta| < 2.4$ , the expected muon and background rates are higher and the magnetic field is large and non-uniform, both of which preclude the use of DTs. Instead, the muon system endcaps are instrumented with cathode strip chambers (CSCs) that have a high response time, fine segmentation, and higher radiation resistance. The CSCs have 4 stations in each endcap with chambers that are aligned perpendicular to the beam line and are able to provide measurements in the  $r - \phi$  plane and  $z$ -direction, along with the beam crossing time of a muon.

Both the DTs and CSC are capable of providing high efficiency and pure muon  $p_T$  triggers, independent of the rest of the detector. But in order to further improve this, particularly at the full LHC luminosity, another complementary trigger system consisting of Resistive Plate Chambers (RPCs) was added to both the barrel and endcap regions ( $|\eta| < 1.6$ ). The RPCs are double-gap chambers that operate with a fast response and good time resolution. The spatial resolution, however, is coarser than the DTs or CSCs, though the extra hits in the RPC still help resolve ambiguities when making tracks. There are a total of 6 RPC layers in the barrel muon system, which help improve triggers for low  $p_T$  muons, and 3 layers in each of the endcaps that help reduce background and improve the time and  $p_T$  resolution of muons.

#### 4.2.5 Trigger System

The high instantaneous luminosity of the LHC provides many technical challenges for the data acquisition system (DAQ), with proton-proton collisions occurring every 25 ns,

corresponding to a frequency of 40 MHz. At this collision rate, it is unfeasible to process and store the data for each event. In order to reduce the rate, a two-stage trigger system is used to select only the most “interesting” events for processing.

The first stage is the Level-1 (L1) trigger system, which has approximately only  $4 \mu\text{s}$  to decide whether or not an event should be further processed. In order to operate at this timescale, the L1 trigger uses only coarse-grained information from the CMS calorimeters and the muon system.

For the calorimeter set of data, the L1 first generates trigger primitives by looking for large energy deposits in the calorimeter. These trigger primitives are then passed to the Regional Calorimeter Trigger (RCT), which uses this information to determine electron/photon candidates and transverse energy sums per calorimeter region. In addition, the RCT also calculates information relevant for detecting minimally ionizing particles, vetoing tau leptons, and muon isolation. Lastly, the Global Calorimeter Trigger (GCT) uses the information from the RCT to construct jets and calculate the event-level transverse energy and missing transverse energy, along with the final isolated and non-isolated electron/photon candidates.

For the muon portion of the L1 trigger system, the DTs and CSCs both compute local trigger information which consists of two- and three-dimensional track segments, respectively. This information is then passed to a join DT-CSC track finder, which connects these segments into a full candidate track. At the same time, the RPC constructs a separate, independent set of track candidates. Both sets of candidate tracks are sent to the Global Muon trigger (GMT), which also takes in the relevant information from the RCT, to construct muon candidates.

Lastly, the candidate particles and event-level information from the GCT and GMT are sent to the Global Trigger, which takes this information and checks to see if certain criteria are met. If so, a L1 Accept (L1A) is generated, which signals for the event to

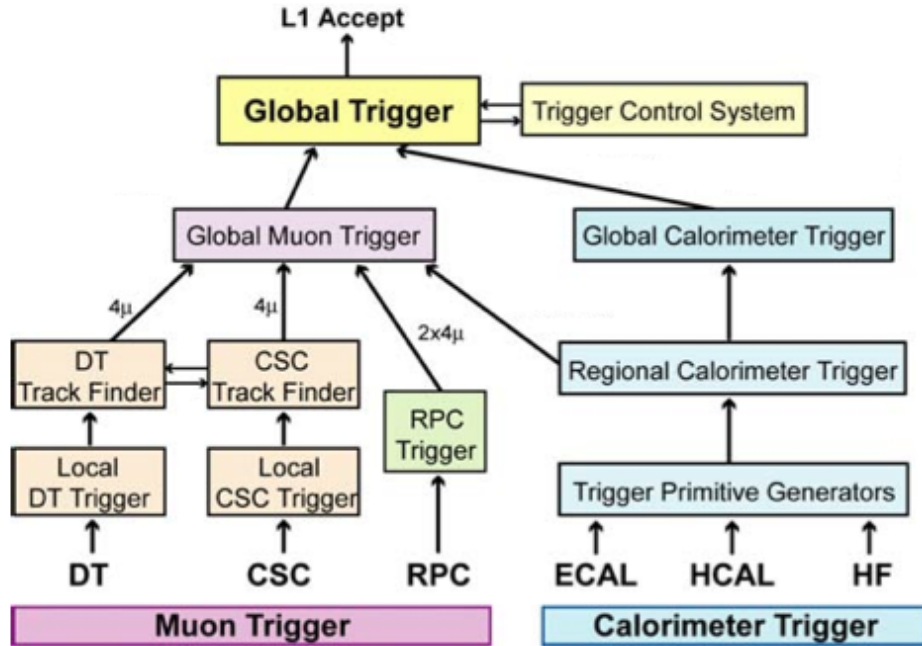


Figure 4.9: Flowchart depicting the generation of a L1 Accept. [13]

be fully read out. This process, shown in Figure 4.9, reduces the full readout rate to at most 100 kHz.

On the generation of an L1A, all the CMS subsystems read out their buffered data corresponding to the L1A event to the an event builder. The data the event builder receives is both more complete and at a finer resolution, allowing it to construct more complex quantities before sending it to the High Level Trigger (HLT), the second stage of the trigger system.

The HLT software is run on a processor farm that reconstructs events in greater detail to decide whether or not they should be kept. This framework is flexible as both the HLT software and the processor farm can be updated to meet changing experimental needs. As such the exact criteria used by the HLT in its decision varies with time, but generally involves thresholding the  $p_T$  and/or multiplicity of particles along with

event-level quantities, such as  $H_T$ . At the end of this process, the trigger rate is at approximately 100 Hz.

# Chapter 5

## Particle Reconstruction and Identification

### 5.1 Tracks

Track reconstruction with the CMS detector faces many challenges, as at each bunch crossing  $\sim O(10^3)$  particles are expected to pass through the CMS tracking system, all of which must be reconstructed in time to be inputted to the HLT. This constraint makes it immensely challenging to attain high track-finding efficiency, while minimizing the number of fake tracks.

The first step of track reconstruction is to reconstruct “hits” in a process called “local reconstruction”. In this step, signals in both the pixel and strip channels that are above some zero-suppression threshold are clustered together into hits, where the cluster positions and uncertainties are then estimated.

Next, tracks are reconstructed from these hits in order to provide estimates for the momentum and position of charged particles associated with the track. This is done using specialized software based off of Kalman filters known as Combinatorial Track Finder (CTF). In order to reduce the combinatorial complexity of the problem, the CTF track reconstruction is performed six times. Each iteration attempts to reconstruct the

most easily-identifiable tracks, e.g. high- $p_T$  tracks, and then removes the hits associated with those tracks. This helps simplify the track reconstruction in the following iterations.

Each iteration consists of four steps:

1. A seed is generated from a few (generally 2 or 3) hits. This seed provides an initial estimate of the trajectory and uncertainties associated with thet track.
2. A Kalman-based track finder is used to extrapolate seed trajectories along their expected paths. Additional hits that are compatabile with a path are assigned to that track candidate.
3. A track-fitting module uses a Kalaman filter and smoother to provide estimates of the trajectory parameters for each track.
4. A track selection sets quality thresholds and discards tracks that fail the specified criteria.

A detailed description of track reconstruction can be found in Reference [51].

### 5.1.1 Vertices

An essential part of event reconstruction is identifying which particles were produced at parton-parton interaction vertices (primary vertices) and which were produced at secondary decay vertices afterwards (secondary vertices). The process for selecting primary vertices consists of three steps: track selection, track clustering, and track fitting.

The track selection criteria is chosen in order to select tracks that are consistent with being produced promptly in the primary interaction region. Tracks are required to have a lot transverse impact parameter relative to the beam spot, a certain number of hits in the pixel and strip detectors, and good fit quality when fitting to the trajectory.

No requirement is placed on the  $p_T$  of tracks, in order to ensure a high reconstruction efficiency, even for minimum-bias events.

After the track selection, a deterministizing annealing clustering algorithm is used in order to group together tracks that appear to originate from the same vertex [52]. Here the selected tracks are originally all assigned to the same vertex and are then slowly divided into multiple vertices. This process continues until reaching a cutoff defined by balancing the risk of incorrectly splitting vertices and the resolving power of the algorithm.

Once the track clustering is completed, an “adaptive vertex fitter” is used to determine the 3D-position of vertices with at least two tracks [53], in which tracks corresponding to a vertex are each assigned a probability of correctly belonging to the vertex. The weighted sum of these probabilities is then used in the fitting algorithm to determine primary vertices.

In this process, many more than one primary vertex are reconstructed due to multiple parton-parton interactions in an event. There is, however, usually only one primary vertex of interest in the event, corresponding to the primary vertex with the highest sum of track  $p_T^2$ . This primary vertex is commonly referred to as *the* primary vertex.

## 5.2 Calorimeter Clusters

Energy deposits in the various CMS calorimeters are clustered together to form “calorimeter clusters”. The purpose of the calorimeter clusters are to aid in, detecting and measuring the energy and direction of stable neutral particles, separating these neutral particles from the energy deposits of charged hadrons, reconstructing and identifying electrons, along with their corresponding bremsstrahlung photons, and measuring the energy of charged hadrons with low-quality track parameters

The calorimeter clustering is done in three steps. First, cluster seeds are identified as cells with an energy both larger than some threshold and larger than the energy of neighboring cells. Next, these cluster seeds are formed into “topological clusters” by iteratively merging together neighboring cells that have significant energy deposits. In this process, topological clusters can merge such that a cluster contains multiple cluster seeds. Lastly, the energy in a topological cluster is distributed among its seeds through a Gaussian-mixture model that results in the final calorimeter clusters.

This clustering is performed separately in each subdetector calorimeter, including the ECAL preshower detector, for which its two layers are treated independently. There is no clustering performed in the HF, as each cell’s short- and long-fibers measure the electromagnetic- and hadronic-energy components, as described in Sub-section 4.2.3. These components directly give rise to “HF EM” and “HF HAD” clusters.

## 5.3 Particle Flow

The particle-flow (PF) algorithm is a holistic approach towards event reconstruction. It combines the basic information of subdetectors, i.e. the tracks and clusters defined above, to identify each final-state particle and reconstruct their corresponding properties. By correlating measurements from the tracker and calorimeter, the PF algorithm is able to provide improved energy and momentum measurements. A complete, detailed presentation of the particle-flow algorithm is given in [54, 55, 56].

### 5.3.1 Linking

As a particle transverses through the CMS detector, it is expected to generate multiple input elements to the PF algorithm. Thus, the first step of reconstructing particles is to *link* the various PF elements stemming from different subdetectors together. This is

done by defining a “distance” between two linked elements, where the closer the distance the more probable it is the two elements correspond to the same particle. The linking algorithm then creates *PF blocks* by associating directly or indirectly linked elements together. The exact criteria used to link elements together and define their distance depends on the type of elements being considered and are listed below.

A link between a track and calorimeter cluster is established by extrapolating the track trajectory through the ECAL and HCAL, up to a depth where energy deposits are most expected. If the extrapolated track falls within the area of the calorimeter cluster, the two elements are linked and the link distance is defined as the separation between their positions in the  $(\eta, \phi)$  plane. In the case multiple clusters are linked to the same track only the link with the smallest distance is kept.

To link tracks with clusters from potential bremsstrahlung photons, tangents to the track are extrapolated to the ECAL. If a tangent line falls within the cluster, the track and cluster are linked with the  $\eta$ - $\phi$  separation used as the link distance.

Calorimeter clusters in the HCAL, ECAL, and preshower detector are linked together when the position of a cluster in a more granular calorimeter (preshower or ECAL) is within the boundaries of a cluster with less granularity (ECAL or HCAL). The distance between these two clusters is defined as either the  $\eta$ - $\phi$  or  $x$ - $y$  separation for HCAL-ECAL and ECAL-preshower links, respectively. In the case where multiple HCAL(ECAL) clusters are linked to the same ECAL(preshower) cluster, only the link with the smallest distance is used.

Links between a track and a standalone-muon track, defined as a track segment constructed from hits in the muon system, are established when a global fit to the two tracks has an acceptable fit quality. The link distance in this case is defined as the  $\chi^2$  of the fit, only the link with the smallest  $\chi^2$  is retained when there are multiple links to the same standalone-muon track. The resulting links are called “global muons”.

### 5.3.2 PF Reconstruction and Identification

Once the PF blocks have been constructed, the PF algorithm is applied to reconstruct and identify a set of particles from each PF block. This algorithm proceeds sequentially to hierarchically reconstruct particles as described below.

First, PF muons are formed by global muons whose momentum is compatible with that determined by only using the tracker. The corresponding tracks are then removed from the PF block.

Next, PF electrons are identified by using information from the inner tracker and calorimeters. Electron candidates in a PF block are seeded by tracks with links to ECAL clusters. These tracks are then re-extrapolated to the ECAL, and if a track is found to be compatible with ECAL energy deposits and consistent with an electron, the track and clusters are labelled a PF electron and are removed from the PF block.

The remaining elements in the PF block are used to form charged hadrons, photons, neutral hadrons, and, in rare cases, additional muons. PF elements are identified as one of these particle-types by comparing the track momentum to the linked cluster energies. The following scenarios define the identification process:

- If the total cluster energy is much smaller than the track momentum, the excess track momentum is labeled as a muon or fake track. This occurs for less than 0.03% of the tracks used in the algorithm.
- If the total cluster energy agrees within the uncertainty of the track momentum, a PF charged hadron is formed. The PF charged hadron is then assigned a mass equal to that of a charged pion and a momentum based on a fit of the tracker and calorimeter measurements.
- If the total cluster energy is significantly larger than the track momentum and

the excess is greater than the total ECAL energy, than the track is considered a PF charged hadron, as described above, the excess ECAL energy is labeled a PF photon, and the remaining energy is assigned to a PF neutral hadron. The excess ECAL energy is preferentially given to photons over neutral hadrons, as typically photons account for 25% of the energy of a jet, while neutral hadrons only account for 3%.

- If the total cluster energy is significantly larger than the track momentum and the excess is less than the total ECAL energy, the track is considered a PF charged hadron and the excess calorimeter energy is assigned as a PF photon.
- If there are ECAL or HCAL clusters without any linked tracks, the deposits are respectively treated as PF photons and PF neutral hadrons.

## 5.4 Leptons

As the identification criteria for selecting PF electrons and PF muons are weak, these object serve as candidate particles. To increase the purity of true electrons(muon), more stringent criteria must be passed for a PF electron(muon) to be considered an analysis-level electron(muon). The number of analysis-level leptons, where a lepton is defined as either an electron or muon, is denoted as  $N_{\text{leps}}$ .

### 5.4.1 Electrons

The electron candidates are required to have  $p_T > 20 \text{ GeV}$ ,  $|\eta| < 2.5$ , and to satisfy identification criteria [57] designed to remove hadrons misidentified as electrons, photon conversions, and electrons from heavy-flavor hadron decays. This criteria is shown in Table 5.1, where  $\sigma_{i\eta i\eta}$  is a variable based on the width of the electron shower shape,

Criteria	Barrel requirement	Endcap requirement
$\sigma_{inj\eta}$	$< 0.0101$	$< 0.0283$
$\Delta\eta(\text{cluster, track})$	$< 0.0103$	$< 0.07333$
$\Delta\phi(\text{cluster, track})$	$< 0.0336$	$< 0.114$
$E_{\text{hadronic}}/E_{\text{electromagnetic}}$	$< 0.876$	$< 0.0678$
$\frac{1}{E} - \frac{1}{p} [\text{GeV}^{-1}]$	$< 0.0174$	$< 0.0898$
$ d_0  [\text{mm}]$	$< 0.0118$	$< 0.0739$
$ d_z  [\text{mm}]$	$< 0.373$	$< 0.602$
Missing hits	$\leq 2$	$\leq 1$
Pass photon conversion	True	True

Table 5.1: Identification criteria that a PF electron must pass in order to be considered an analysis-level electron.

and  $d_0$  and  $d_z$  are the transverse and longitudinal impact parameters, respectively, of the associated electron track.

Additionally, to preferentially select electrons that originate in the decay of W and Z bosons, electrons are required to be isolated from other PF candidates. The relative isolation of a particle  $I^{\text{rel}}$  is quantified using an optimized version of the mini-isolation variable  $I_{\text{mini}}$ . Mini-isolation is computed as the scalar sum of the  $p_T$  of charged hadrons from the PV, neutral hadrons, and photons that are within a cone of radius  $R^{\text{mini-iso}}$  surrounding the electron momentum vector  $\vec{p}$  in  $\eta$ - $\phi$  space [58]. The cone radius  $R^{\text{mini-iso}}$  varies with  $1/p_T$  according to

$$R^{\text{mini-iso}} = \begin{cases} 0.2, & p_T \leq 50 \text{ GeV} \\ 10 \text{ GeV}/p_T, & 50 < p_T \leq 200 \text{ GeV} \\ 0.05, & p_T > 200 \text{ GeV}. \end{cases} \quad (5.1)$$

The  $p_T$ -dependent cone size reduces the rate of accidental overlaps between the electron and jets in high-multiplicity or highly Lorentz-boosted events, particularly overlaps between bottom quark jets and leptons originating from a boosted top quark. Relative

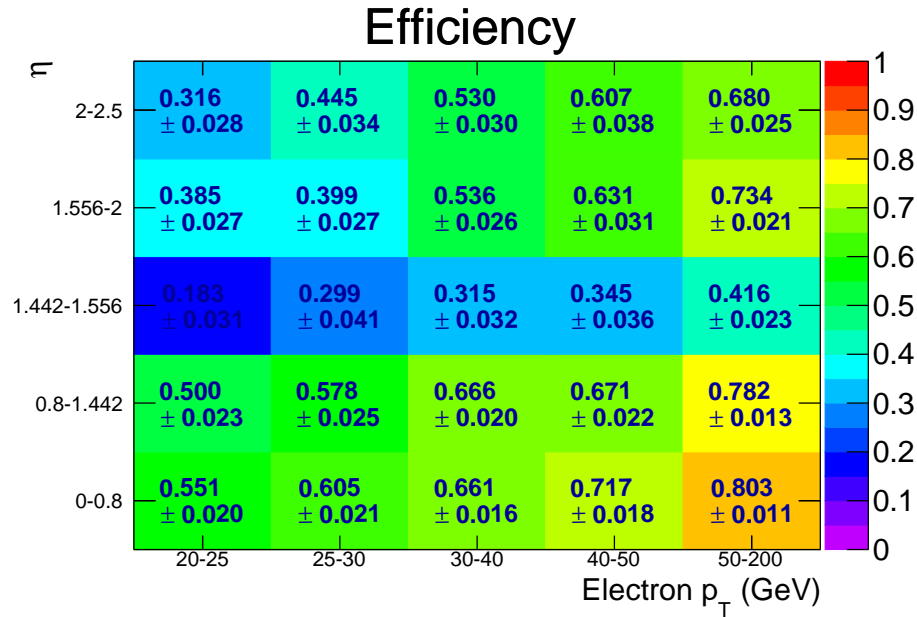


Figure 5.1: The efficiency to select an analysis-level electron as a function of  $p_T$  and  $\eta$ .

isolation is computed as  $I^{\text{rel}} = I_{\text{mini}}/p_T$  after subtraction of the average contribution from additional proton-proton collisions in the same bunch-crossing (pileup). To be considered isolated, electrons must satisfy  $I^{\text{rel}} < 0.1$ .

The combined efficiency for the electron reconstruction, identification, and isolation requirements, shown in Figure 5.1, is about 50% at  $p_T$  of 20 GeV, increasing to 65% at 50 GeV, and reaching a plateau of 80% above 200 GeV [59].

### 5.4.2 Muons

The muon candidates are required to have  $p_T > 20$  GeV,  $|\eta| < 2.4$ , and to satisfy identification criteria [60] to select a high purity muon sample. This criteria is shown in Table 5.2, where  $d_0$  and  $d_z$  are the transverse and longitudinal impact parameters, respectively, of the associated muon track. Analogously to electron candidates, muon candidates are required to satisfy  $I^{\text{rel}} < 0.2$ , where the looser threshold is to account for

Criteria	Requirement
Is PF muon	True
Fraction of valid tracker hits	> 0.8
AND	
$ d_0 $ [mm]	< 2
$ d_z $ [mm]	< 5
Is global muon	True
Normalized global-track $\chi^2$	< 3
$\chi^2$ of tracker-standalone position match	< 12
Track-kink $\chi^2$	< 20
Segment compatibility	> 0.303
OR	
Segment compatibility	> 0.451

Table 5.2: Identification criteria that a PF muon must pass in order to be considered an analysis-level muon.

purity differences between electrons and muons.

The efficiency for reconstructing muons, shown in Figure ?? is about 70% at  $p_T$  of 20 GeV, increasing to 80% at 50 GeV, and reaching a plateau of 95% for  $p_T > 200$  GeV [61].

## 5.5 Jets

When a quark or gluon is produced at the LHC, due to color confinement, they quickly hadronize and produce a collimated “spray” of particles, called a jet, which is the direct detector observable. The parameter of interest, however, is the momentum of the initial parton before hadronization. Thus, clustering the constituent jet particles in a way that accurately reconstructs the initial parton momentum is essential. Events, however, often contain multiple jets with each jet typically composed of some  $\sim 10\text{-}100$  particles that are incident on many detector channels across a large area. This makes the problem of jet clustering non-trivial and an important aspect of object reconstruction.

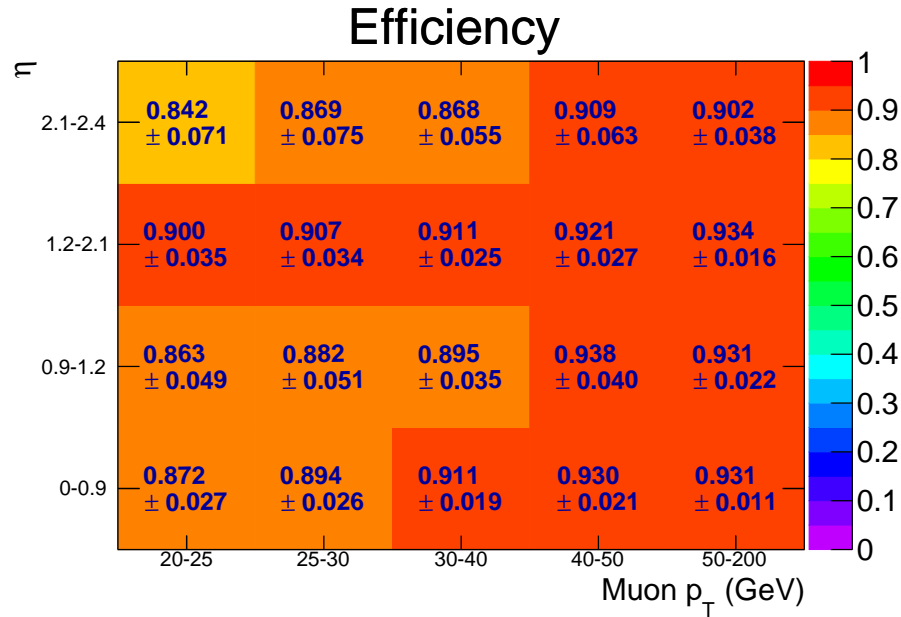


Figure 5.2: The efficiency to select an analysis-level muon as a function of  $p_T$  and  $\eta$ .

### 5.5.1 Clustering

Jets are not physically-defined objects, and instead it is the clustering rules that define what a jet is. The common class of clustering algorithms used are sequential recombination algorithms, which work by defining a distance measure between pairs of particles, typically based on energy and spatial-location, and then combining the closest pair of particles. This process proceeds sequentially and ends when some threshold condition is met.

In particular, the distance measures,  $d_{ij}$ , which is the distance between two entities (particle or psuedojet), and  $d_{iB}$ , which is the distance between an entity and the beam, are often defined to be

$$d_{ij} = \min(p_{Ti}^{2p}, p_{Tj}^{2p}) \frac{\Delta R_{ij}^2}{R^2}, \quad (5.2)$$

$$d_{iB} = p_{Ti}^{2p}, \quad (5.3)$$

where  $\Delta R_{ij}^2 = \Delta\eta_{ij}^2 + \Delta\phi_{ij}^2$ ,  $R$  is the jet radius parameter that sets the scale of the jet's size, and  $p$  which is a parameter of the algorithm. The clustering procedure then proceeds by finding the smallest of the distances, and if it is a  $d_{ij}$ , the two entities  $i$  and  $j$  are merged, while if it is a  $d_{iB}$ , entity  $i$  is called a jet and is removed from the clustering list.

The parameter  $p$  determines the clustering order of the algorithm and thus different choices for the value of  $p$  lead to different clustering algorithms. For  $p = 1$ , the clustering follows the  $k_T$  algorithm [62], which prioritizes clustering softer particles first. Setting  $p = 0$ , reproduces the Cambridge-Aachen algorithm [63], which uses energy-independent clustering, relying only on the spatial distances between particles. Lastly, choosing  $p = -1$ , gives the anti- $k_T$  algorithm [64], which favors using the harder particles as the jet seeds and then clustering around them. A more detailed disussion of jets, including a comparison of these and other clustering algorithms can be found in Reference [65].

### 5.5.2 Selection

The jets used in this dissertation are constructed by clustering PF candidates with the anti- $k_T$  algorithm and  $R = 0.4$ , using the FASTJET package [66]. To reduce the effect of pileup on the jet clustering and energy measurements, a process called “Charged Hadron Subtraction” is applied, where PF charged hadrons that do not originate from the PV are not included in the jet clustering. In addition, to remove the neutral energy component of pileup, the contribution from PF neutral hadrons produced by pileup is estimated based on the area of a jet and the energy density of the event and subtracted from the jet [67]. Lastly, to prevent double-counting, any jets which contain a PF candidate identified as

Criteria	Requirement
Number of constituents	$> 1$
Charged multiplicity	$> 0$
Neutral electromagnetic fraction	$< 0.99$
Neutral hadron fraction	$< 0.99$
Charged electromagnetic fraction	$< 0.99$
Chaged hadron fraction	$> 0$

Table 5.3: Identification criteria that a jet candidate must pass in order to be considered an analysis-level jet.

an analysis-level electron or muon are removed from the jet collection.

Finally, to be considered an analysis-level jet, the jets must have  $p_T > 30$  GeV,  $|\eta| \leq 2.4$ , and must pass a set of loose identification requirements [68, 69] to suppress, for example, calorimeter noise. These requirements are shown in Table 5.3. The resulting jets are considered to be “small- $R$ ” jets and the variable  $N_{\text{jets}}$  represents the number of these jets in an event. Additionally, a proxy for the hadronic energy scale of an event,  $H_T$ , can be defined as

$$H_T = \sum_{i=1}^{N_{\text{jets}}} p_{T,i}^{\text{jet}} \quad (5.4)$$

### 5.5.3 b-tagging

Jets that are formed through b-quark hadronization have many unique properties that allow them to be differentiated from jets formed through other quarks or gluons. This ability to “b-tag” jets is a very useful tool for determining what physics processes occurred in an event, as b quarks are associated with specific physics process, such as top quark decays. At the same time, many SUSY scenarios, where naturalness considerations motivate light third-generation squarks, result in either the direct or indirect production of b quarks through the decay of SUSY particles. Thus, b-tagging jets is not only often a

crucial component to reducing backgrounds from other processes where no b quarks are expected, but also a powerful selector for potential signal events.

This analysis uses the Combined Secondary Vertex v2 (CSVv2) algorithm [70, 14], which utilizes the long lifetimes, large masses, high-momentum daughter particles, and frequent semi-leptonic decays typical of b hadrons to b-tag jets. As the b quark can only decay to an up or charm quark through highly Cabibbo suppressed weak interactions, b hadrons tend to have long lifetimes, typically on the order of 150 ps. Because of this, b mesons can travel a few mm to a cm from the PV before decaying and producing displaced tracks from which a secondary vertex can be reconstructed. In addition, due to the relatively large b-quark mass, b mesons tend to be heavy, which leads to both large secondary vertex masses and daughter particles with a hard momentum spectrum. Lastly, the weak decay of the b quark results in an associated electron or muon in about 20% of decays. The presence of these soft, nonisolated leptons provides an additional marker for the presence of a b-quark.

The CSVv2 algorithm exploits variables based on information about secondary vertices, their associated displaced tracks, and the presence of soft leptons to accurately tag b-quark jets. A selection of the variables with high discrimination are listed below:

- The significance of the flight distance in the transverse plane.
- The number of SV
- The SV mass
- The number of tracks associated with the SV
- The ratio of the transverse momentum of the SV tracks and the transverse momentum of the jet
- The 3D impact parameter of soft leptons associated with the jet

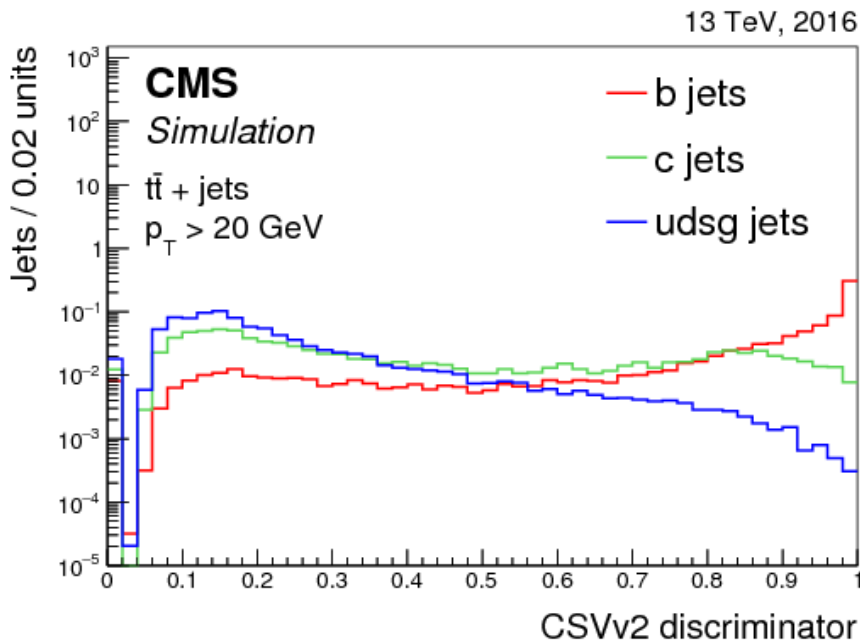


Figure 5.3: The distribution of the CSVv2 discriminator values for jets of different flavors. Jets are selected from  $t\bar{t}$  events and required to have  $p_T > 20$  GeV [14].

These variables are then fed into a multilayer perceptron with one hidden layer then outputs a score between 0 and 1, indicating the likelihood the jet is a b-quark jet. The distribution of CSVv2 discriminator values for different flavor jets is shown in Figure 5.3 [14].

A threshold score for b-tagging a jet is chosen such that the mis-tag rate for light-flavor jets is 1%. This corresponds to a mis-tag rate for c-quark jets of 13–15% (11–13%) in the barrel (endcap) and a tagging efficiency for b jets of 60–67% (51–57%) in the barrel (endcap) for jets with  $p_T$  between 30–50 GeV. The tagging efficiency increases with  $p_T$  before decreasing to  $\approx 50\%$  for jets above 150 GeV. The b-tagging efficiency as a function of jet  $p_T$  is shown in Figure 5.4.

The number of b-tagged jets in an event is denoted as  $N_b$ .

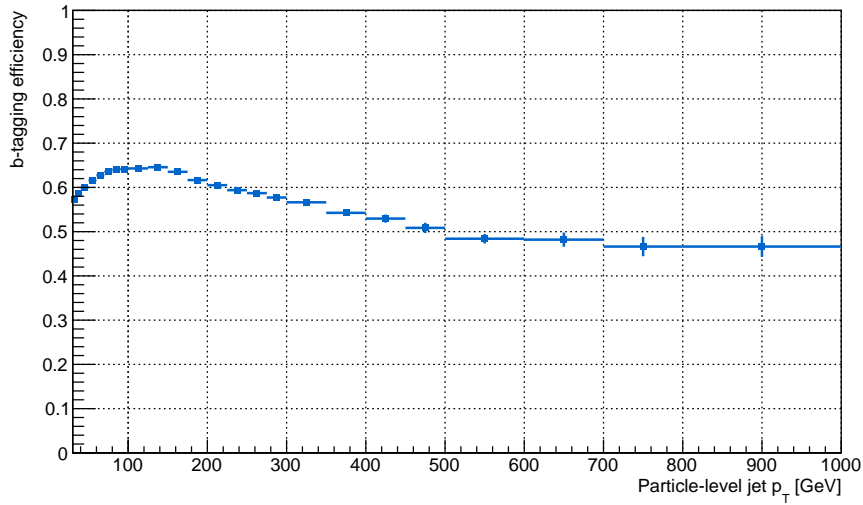


Figure 5.4: The efficiency of the CSVv2 algorithm as a function of jet  $p_T$  at the working point used in this analysis.

## 5.6 Large-radius Jets

While the distance parameter of small- $R$  jets is optimized for clustering the hadronization products of a single parton, it is often useful to exploit information of physical processes on scale larger than a single jet, such as top quark or W boson decays. One way to capture this information is to cluster jets with a large distance parameter, which encodes the momentum, angular, and multiplicity information of the partons contained in the jet.

In particular, this analysis constructs these “large- $R$ ” jets by clustering “small- $R$ ” jets with a distance parameter of  $R = 1.2$ . Due to the relatively small number of small- $R$  jets in an event ( $\lesssim 10$ ), the construction of these large- $R$  jets is insensitive to the clustering algorithm, and the anti- $k_T$  algorithm is used. While these large- $R$  jets could be constructed by performing the clustering at the PF candidate level, no significant improvement in performance was noted. Thus, clustering small- $R$  jets were chosen for the following practical considerations. First, the FASTJET implementation of

the anti- $k_T$  algorithm has complexity  $\mathcal{O}(n \log n)$  [71], which results in a speed-up of on the order of 100x when clustering small- $R$  jets ( $\lesssim 10$  objects) compared to PF candidates ( $\sim 1000$  objects). Secondly, large- $R$  jets clustered from PF candidates would require the computation of new energy-measurement and pileup-removal calibrations for jets of this specific radius. Small- $R$  jets, however, already incorporate standardized calibrations for  $R = 0.4$  jets. Thus, by clustering the calibrated small- $R$  jets, the large- $R$  jets already incorporate corrections without the need of any additional development.

In addition to small- $R$  jets, the jets associated with selected leptons are included in the formation of large- $R$  jets in order to capture as much of the kinematic information as possible. For example, this helps reduce the difference between large- $R$  jets formed by clustering hadronic and (semi-)leptonic decays, as by including the lepton, the only information difference between the two scenarios is due to the undetected neutrino(s).

This technique of clustering small- $R$  jets into large- $R$  jets has been used previously by both the ATLAS and CMS collaborations, e.g. References [72, 73].

### 5.6.1 $M_J$

A measure of the mass-scale of an event,  $M_J$ , can be constructed by summing the masses of large-radius jets, defined as

$$M_J = \sum_{J_i \in \text{large-}R \text{ jets}} m(J_i) \quad (5.5)$$

where  $m(J)$  is the mass of a single large- $R$  jets.

The quantity  $M_J$  has significant discriminating power between SM background processes and signal processes, as SM events tend to have significantly lower mass-scales than signal events that involve high mass particles. For example,  $M_J$  in events with only a produced  $t\bar{t}$  pair is limited to be  $\lesssim 2m_{top} \approx 350$  GeV. This is because the top quarks

decay back-to-back and if each top quark’s decay products are captured in a single large- $R$  jet, two large- $R$  jets are clustered each with  $m(J) = m_{top}$ , resulting in  $M_J = 2m_{top}$ . In the case, where a top quark is not fully contained in a large- $R$  jet, the mass of that large- $R$  jet, and correspondingly  $M_J$ , is even smaller. For signal events, however, the mass-scale is roughly set by the gluino mass, which is on the order of 1 TeV.

The  $M_J$  distribution in  $t\bar{t}$  and signal events with  $m_{\tilde{g}} = 1000$  GeV and 1600 GeV, selected with a  $N_{\text{jets}} \geq 8$  requirement to ensure both processes have a  $N_{\text{jets}}$  distribution, is shown in Figure 5.5. From the figure, it can be seen that the  $M_J$  distribution gets increasingly harder with higher gluino mass. Also of note is that the  $M_J$  distribution in  $t\bar{t}$  events extends past  $2m_{top}$ . This is because, in the presence of significant ISR, the ISR jets can either overlap with the  $t\bar{t}$  daughter jets or boost the  $t\bar{t}$  system such that the system is collimated, both with result in high-mass large- $R$  jets and, correspondingly, high  $M_J$ . Processes of this nature are responsible for generating high  $M_J$  background events.

The quantity  $M_J$  was proposed in phenomenological studies [74, 75, 76] and was first used for RPC SUSY searches by the ATLAS Collaboration in all-hadronic final states [77, 78] and by the CMS Collaboration in single-lepton events [73, 79]. Additionally, the basic properties and performance of the  $M_J$  variable were commissioned using early  $\sqrt{s} = 13$  TeV data [80].

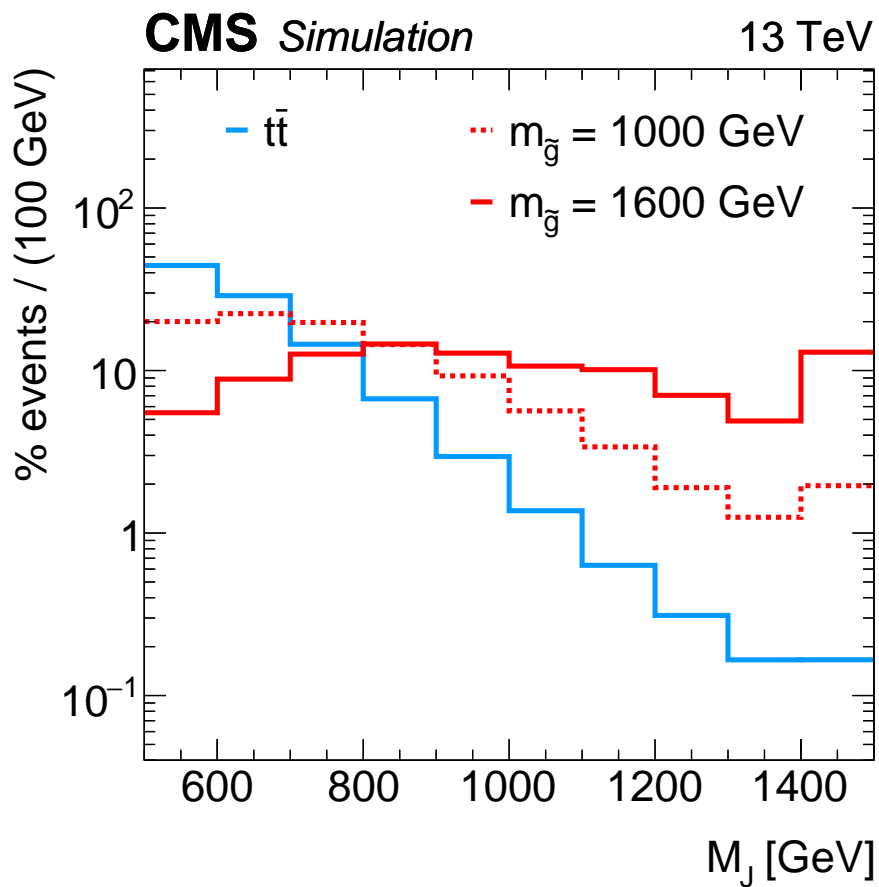


Figure 5.5: Distributions of  $M_J$ , normalized to the same area, for  $t\bar{t}$  events and signal events with  $m_{\tilde{g}} = 1000$  GeV and 1600 GeV in a selection of  $N_{\text{leps}} = 1$ ,  $H_T > 1200$  GeV,  $N_{\text{jets}} \geq 8$ ,  $M_J > 500$  GeV, and  $N_b \geq 1$ .

## Part III

# Data, Simulation, and Selection

# Chapter 6

## Data Samples and Simulation

### 6.1 Data

The dataset used in this search corresponds to  $35.9 \text{ fb}^{-1}$  of proton-proton collisions at  $\sqrt{s} = 13 \text{ TeV}$  collected by the CMS detector over the year 2016. This is a subset of the  $40.8 \text{ fb}^{-1}$  delivered by the LHC and selected to correspond to when all sub-detectors were fully-operational. A plot of the cumulative delivered and recorded integrated luminosity by the LHC and CMS, respectively, is shown in 6.1.

The data samples used in this analysis are shown in Table 6.1. The **JetHT** datasets are primarily used to populate the analysis search region with events, while the **Single Electron** and **Single Muon** datasets are primarily used for trigger efficiency studies.

### 6.2 Monte Carlo Simulation

Monte Carlo simulations (MC) are used to model both SM and BSM physics processes and are extremely useful in the design and optimization of the analysis strategy of new-physics searches. These simulated samples allow for studying processes that in data would have control regions with impure and/or small sample sizes or, in the case of signal processes, may not even exist. This allows for both the optimization and validation of

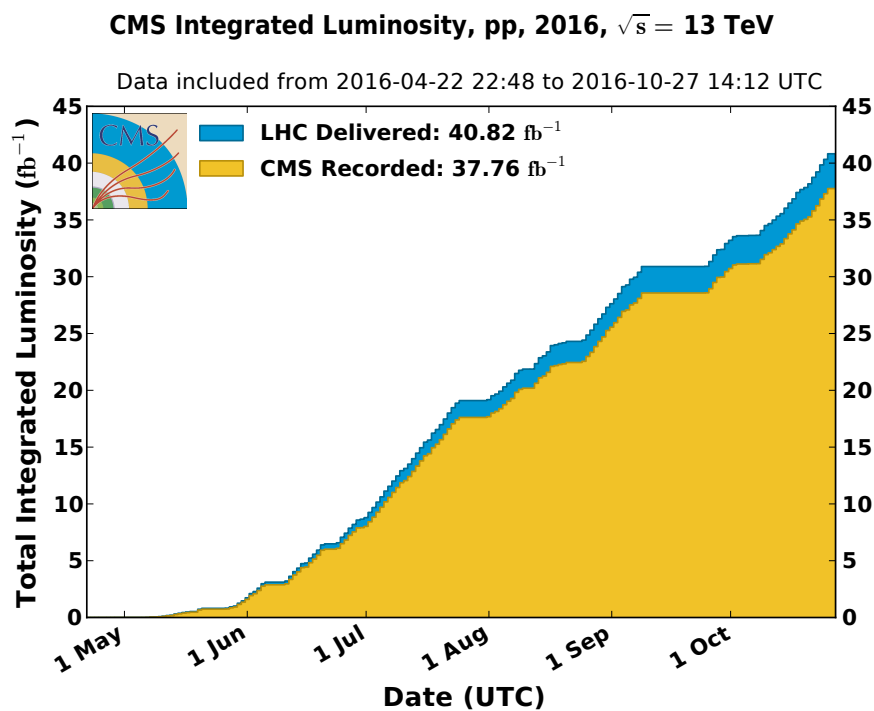


Figure 6.1: Delivered and recorded integrated luminosity by the LHC and CMS, respectively, over 2016. [15]

Dataset name
/JetHT/Run2016B-03Feb2017_ver2-v2/MINIAOD
/JetHT/Run2016C-03Feb2017-v1/MINIAOD
/JetHT/Run2016D-03Feb2017-v1/MINIAOD
/JetHT/Run2016E-03Feb2017-v1/MINIAOD
/JetHT/Run2016F-03Feb2017-v1/MINIAOD
/JetHT/Run2016G-03Feb2017-v1/MINIAOD
/JetHT/Run2016H-03Feb2017_ver2-v1/MINIAOD
/JetHT/Run2016H-03Feb2017_ver3-v1/MINIAOD
/SingleElectron/Run2016B-03Feb2017_ver2-v2/MINIAOD
/SingleElectron/Run2016C-03Feb2017-v1/MINIAOD
/SingleElectron/Run2016D-03Feb2017-v1/MINIAOD
/SingleElectron/Run2016E-03Feb2017-v1/MINIAOD
/SingleElectron/Run2016F-03Feb2017-v1/MINIAOD
/SingleElectron/Run2016G-03Feb2017-v1/MINIAOD
/SingleElectron/Run2016H-03Feb2017_ver2-v1/MINIAOD
/SingleElectron/Run2016H-03Feb2017_ver3-v1/MINIAOD
/SingleMuon/Run2016B-03Feb2017_ver2-v2/MINIAOD
/SingleMuon/Run2016C-03Feb2017-v1/MINIAOD
/SingleMuon/Run2016D-03Feb2017-v1/MINIAOD
/SingleMuon/Run2016E-03Feb2017-v1/MINIAOD
/SingleMuon/Run2016F-03Feb2017-v1/MINIAOD
/SingleMuon/Run2016G-03Feb2017-v1/MINIAOD
/SingleMuon/Run2016H-03Feb2017_ver2-v1/MINIAOD
/SingleMuon/Run2016H-03Feb2017_ver3-v1/MINIAOD

Table 6.1: Data samples analyzed for this analysis. The corresponding integrated luminosity is  $35.9 \text{ fb}^{-1}$ .

the (signal-plus-)background prediction methods, as the sensitivity of the analysis to particular signal models can be estimated and pathologies in the prediction methodology can be unearthed and investigated. Additionally, the simulated samples can be used to help commission and understand the collected data by comparing expectations from simulation to what is actually observed, particularly in the initial data taking periods.

### 6.2.1 Background Samples

The `MADGRAPH5_aMC@NLO` 2.2.2 event generator is used in leading-order (LO) mode [81, 82] to generate the  $t\bar{t}$ , quantum chromodynamics multijet (QCD),  $W + \text{jets}$  and Drell–Yan background processes with extra partons, while the  $t\bar{t}W$ ,  $t\bar{t}Z$ ,  $t\bar{t}t\bar{t}$ , and  $t$ -channel single top quark production backgrounds are generated with `MADGRAPH5_aMC@NLO` 2.2.2 in next-to-leading order (NLO) mode [83]. The `POWHEG` 2.0 event generator [84, 85, 86] is used to generate the  $tW$ ,  $\bar{t}W$ , and  $s$ -channel single top quark processes at NLO precision.

The  $t\bar{t}$ ,  $W + \text{jets}$ , and QCD samples are generated with up to 2, 4, and 2 extra partons, respectively, and all samples are generated using a top quark mass of 172.5 GeV and with the NNPDF3.0 set of parton distribution functions (PDF) [87]. For the fragmentation and showering of partons, the generated samples are interfaced with `PYTHIA` 8.205 [88] and use the CUETP8M1 tune to describe the underlying event [89]. The detector response is simulated with `GEANT4` [90], and the simulated samples are processed through the same reconstruction algorithms as the data, as discussed in Chapter 5. The background samples are normalized to the highest precision cross sections available [91, 92, 93, 94, 95, 96, 97].

The background samples used, along with their sample size and equivalent luminosity, are shown in Table 6.2.

### 6.2.2 Signal Samples

For ease of generation and interpretation, signal samples are produced according to the Simplified Model Spectra (SMS) paradigm [98, 99], where all but one or two mass parameters in a particular decay chain are fixed. Due to their “simplicity”, SMS models can be interpreted generally, reducing the sensitivity of results to model specifics and allowing

Simulated sample name	Events	L [ $\text{fb}^{-1}$ ]
TTJets_TuneCUETP8M1_13TeV-madgraphMLM-pythia8	10,259,790	12.57
TTJets_SingleLeptFromT_TuneCUETP8M1_13TeV-madgraphMLM-pythia8	53,056,561	296.90
TTJets_SingleLeptFromTbar_TuneCUETP8M1_13TeV-madgraphMLM-pythia8	60,282,318	337.34
TTJets_DiLept_TuneCUETP8M1_13TeV-madgraphMLM-pythia8	30,681,952	358.18
TTJets_HT-600to800_TuneCUETP8M1_13TeV-madgraphMLM-pythia8	13,838,472	5,291.21
TTJets_HT-800to1200_TuneCUETP8M1_13TeV-madgraphMLM-pythia8	10,506,985	9,753.77
TTJets_HT-1200to2500_TuneCUETP8M1_13TeV-madgraphMLM-pythia8	2,913,606	14,943.68
TTJets_HT-2500toInf_TuneCUETP8M1_13TeV-madgraphMLM-pythia8	523,826	225,454.60
QCD_HT100to200_TuneCUETP8M1_13TeV-madgraphMLM-pythia8	82,072,813	0.00
QCD_HT200to300_TuneCUETP8M1_13TeV-madgraphMLM-pythia8	57,336,294	0.03
QCD_HT300to500_TuneCUETP8M1_13TeV-madgraphMLM-pythia8	54,706,023	0.15
QCD_HT500to700_TuneCUETP8M1_13TeV-madgraphMLM-pythia8	63,336,989	2.16
QCD_HT700to1000_TuneCUETP8M1_13TeV-madgraphMLM-pythia8	45,232,792	6.93
QCD_HT1000to1500_TuneCUETP8M1_13TeV-madgraphMLM-pythia8	15,314,987	14.39
QCD_HT1500to2000_TuneCUETP8M1_13TeV-madgraphMLM-pythia8	11,647,431	95.86
QCD_HT2000toInf_TuneCUETP8M1_13TeV-madgraphMLM-pythia8	6,004,039	236.19
WJetsToLNu_TuneCUETP8M1_13TeV-madgraphMLM-pythia8	28,210,241	0.46
WJetsToLNu_HT-100To200_TuneCUETP8M1_13TeV-madgraphMLM-pythia8	27,546,847	16.90
WJetsToLNu_HT-200To400_TuneCUETP8M1_13TeV-madgraphMLM-pythia8	19,851,490	45.57
WJetsToLNu_HT-400To600_TuneCUETP8M1_13TeV-madgraphMLM-pythia8	7,432,643	125.41
WJetsToLNu_HT-600To800_TuneCUETP8M1_13TeV-madgraphMLM-pythia8	18,132,628	1,243.62
WJetsToLNu_HT-800To1200_TuneCUETP8M1_13TeV-madgraphMLM-pythia8	1,540,354	231.42
WJetsToLNu_HT-1200To2500_TuneCUETP8M1_13TeV-madgraphMLM-pythia8	7,012,526	4,360.78
WJetsToLNu_HT-2500ToInf_TuneCUETP8M1_13TeV-madgraphMLM-pythia8	2,505,140	64,376.98
DYJetsToLL_M-50_TuneCUETP8M1_13TeV-madgraphMLM-pythia8	49,190,673	8.17
DYJetsToLL_M-50_HT-100to200_TuneCUETP8M1_13TeV-madgraphMLM-pythia8	7,558,769	44.08
DYJetsToLL_M-50_HT-200to400_TuneCUETP8M1_13TeV-madgraphMLM-pythia8	8,683,638	165.14
DYJetsToLL_M-50_HT-400to600_TuneCUETP8M1_13TeV-madgraphMLM-pythia8	396,532	58.65
DYJetsToLL_M-50_HT-600to800_TuneCUETP8M1_13TeV-madgraphMLM-pythia8	8,231,815	4,910.15
DYJetsToLL_M-50_HT-800to1200_TuneCUETP8M1_13TeV-madgraphMLM-pythia8	2,650,562	3,188.24
DYJetsToLL_M-50_HT-1200to2500_TuneCUETP8M1_13TeV-madgraphMLM-pythia8	616,458	4,320.56
DYJetsToLL_M-50_HT-2500toInf_TuneCUETP8M1_13TeV-madgraphMLM-pythia8	375,865	117,894.02
ST_s-channel_4f_leptonDecays_13TeV-amcatnlo-pythia8_TuneCUETP8M1	999,995	116.20
ST_t-channel_antitop_4f_leptonDecays_13TeV-powheg-pythia8_TuneCUETP8M1	1,682,394	64.14
ST_t-channel_top_4f_leptonDecays_13TeV-powheg-pythia8_TuneCUETP8M1	3,279,179	74.41
ST_tW_antitop_5f_NoFullyHadronicDecays_13TeV-powheg_TuneCUETP8M1	5,388,666	343.66
ST_tW_top_5f_NoFullyHadronicDecays_13TeV-powheg_TuneCUETP8M1	5,405,674	344.74
ttHJetTobb_M125_13TeV_amcatnloFXFX_madspin_pythia8	9,823,967	2,957.09
TTGJets_TuneCUETP8M1_13TeV-amcatnloFXFX-madspin-pythia8	4,664,534	132.40
TTTT_TuneCUETP8M1_13TeV-amcatnlo-pythia8	752,497	14,412.60
TTWJetsToLNu_TuneCUETP8M1_13TeV-amcatnloFXFX-madspin-pythia8	252,664	328.75
TTWJetsToQQ_TuneCUETP8M1_13TeV-amcatnloFXFX-madspin-pythia8	833,278	547.03
TTZToLLNuNu_M-10_TuneCUETP8M1_13TeV-amcatnlo-pythia8	398,596	340.36
TTZToQQ_TuneCUETP8M1_13TeV-amcatnlo-pythia8	749,386	310.64
WWTo2L2Nu_13TeV-powheg	1,996,585	163.95
WZTo3LNu_TuneCUETP8M1_13TeV-powheg-pythia8	1,820,203	410.91

Table 6.2: Simulated background samples used in this analysis with their corresponding sample size and equivalent luminosity.

for results to be applicable to a wide variety of new-physics models. Additionally, the use of SMS models results in significantly reduced computing time for model generation, as models need to be produced by scanning across at most only two parameters.

The assumptions used in the simplified model of the  $\tilde{g} \rightarrow t\bar{t} \rightarrow tbs$  process, denoted as T1tbs, are given below:

- squarks other than the top squark are much heavier than the gluino, so they do not affect the gluino decay
- the branching ratio of  $\tilde{g} \rightarrow t\bar{t} \rightarrow tbs$  is 100%
- the top squark is virtual in its decay. This results in a three-body decay, so searches for dijet resonances, i.e.,  $\tilde{t} \rightarrow bs$ , are not applicable in this scenario.
- the gluinos decay promptly

These assumptions correspond to a model of direct gluino pair production with each gluino decaying to a top, bottom, and strange quark. An example diagram of the T1tbs model is shown in Figure 6.2. The only free parameter in this model is the mass of the gluino, and 11 signal models are generated between  $m_{\tilde{g}} = 1000$  and 2000 GeV in steps of 100 GeV.

These signal models are generated with up to two extra partons in leading-order mode and dynamic factorization and renormalization scales by `MADGRAPH5_aMC@NLO 2.2.2`. The rest of the signal sample production follows the same procedure used for the background samples, which includes the parton fragmentation and showering, simulation, and event reconstruction. Lastly, the samples are normalized to the NLO + next-to-leading logarithmic cross sections for gluino pair production [16].

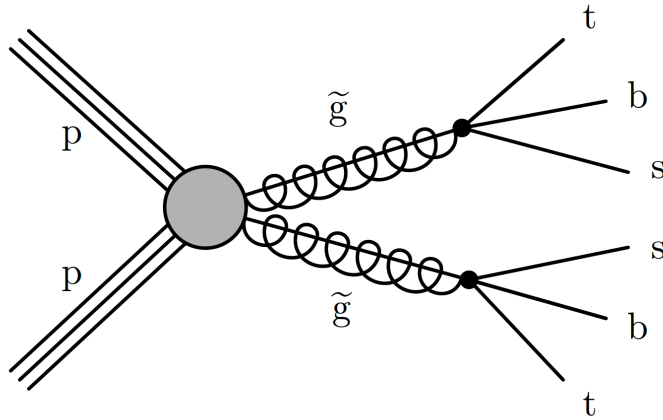


Figure 6.2: Example diagram of the T1tbs simplified model.

Dataset name	Events	$L [fb^{-1}]$
SMS-T1tbs_mGluino-1000_mLSP-0_TuneCUETP8M1_13TeV-madgraphMLM-pythia8	130,281	400.39
SMS-T1tbs_mGluino-1100_mLSP-0_TuneCUETP8M1_13TeV-madgraphMLM-pythia8	71,488	437.26
SMS-T1tbs_mGluino-1200_mLSP-0_TuneCUETP8M1_13TeV-madgraphMLM-pythia8	50,739	592.46
SMS-T1tbs_mGluino-1300_mLSP-0_TuneCUETP8M1_13TeV-madgraphMLM-pythia8	31,815	690.84
SMS-T1tbs_mGluino-1400_mLSP-0_TuneCUETP8M1_13TeV-madgraphMLM-pythia8	21,392	845.61
SMS-T1tbs_mGluino-1500_mLSP-0_TuneCUETP8M1_13TeV-madgraphMLM-pythia8	16,702	1,177.00
SMS-T1tbs_mGluino-1600_mLSP-0_TuneCUETP8M1_13TeV-madgraphMLM-pythia8	10,101	1,246.92
SMS-T1tbs_mGluino-1700_mLSP-0_TuneCUETP8M1_13TeV-madgraphMLM-pythia8	10,380	2,206.99
SMS-T1tbs_mGluino-1800_mLSP-0_TuneCUETP8M1_13TeV-madgraphMLM-pythia8	9,865	3,572.55
SMS-T1tbs_mGluino-1900_mLSP-0_TuneCUETP8M1_13TeV-madgraphMLM-pythia8	10,071	6,157.86
SMS-T1tbs_mGluino-2000_mLSP-0_TuneCUETP8M1_13TeV-madgraphMLM-pythia8	10,556	10,759.60

Table 6.3: Simulated signal samples used in this analysis with their corresponding sample size and equivalent luminosity.

# Chapter 7

## Event Selection

### 7.1 Baseline selection

One of the main challenges for a SUSY search is that the ratio of SM-to-SUSY events is  $\mathcal{O}(10^{12} - 10^{14})$ . To surmount this problem, it is paramount to develop highly efficient signal-to-background discriminators. Fortunately, SUSY signatures typically have characteristics unlike most SM processes. For the T1tbs process, in particular, events are expected to have a large number of jets, many of which are b-quark jets, resulting in a large amount of  $H_T$  and many b-tagged jets. Additionally, the mass scale of the event is expected to be larger than most SM events due to the high masses of the gluinos ( $\mathcal{O}(1 \text{ TeV})$ ), as discussed in Section 5.6.1.

These features are used to construct the “baseline selection”, defined as a basic set of requirements that events must pass, and to reduce the signal-to-background ratio to a more manageable value of  $\mathcal{O}(10^2)$ . Here the baseline selection is defined as  $N_{\text{leps}} = 1$ ,  $H_T > 1200 \text{ GeV}$ ,  $M_J > 500 \text{ GeV}$ ,  $N_{\text{jets}} \geq 4$ , and  $N_b \geq 1$ . To see the separation of signal and background in these variables, the corresponding “N-1” distributions, i.e. the distribution of a variable with the baseline selection applied except for the requirement corresponding to the binned variable, are depicted in Figure 7.1 with the black dashed vertical line representing the value of the baseline cut. Additionally, a “cutflow table” that

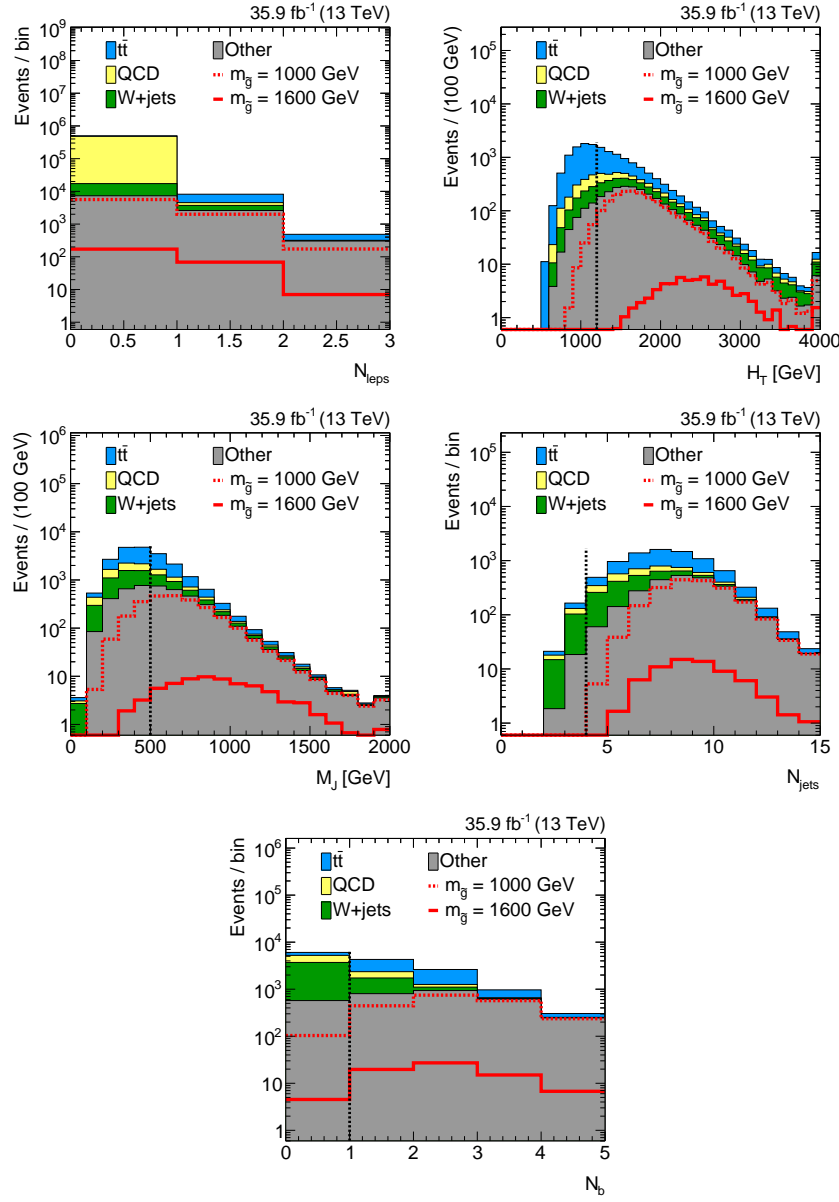


Figure 7.1: The N-1 plots for  $N_{\text{leps}}$  (top-left),  $H_T$  (top-right),  $M_j$  (middle-left),  $N_{\text{jets}}$  (middle-right), and  $N_b$  (bottom). The black dashed vertical line represents the value of the corresponding baseline requirement.

depicts the expected yields for background and signal processes as each baseline selection requirement is individually applied is shown in Table 7.1. Rows above the horizontal line correspond to requirements in the baseline selection, while those below correspond to additional kinematic cuts.

$\mathcal{L} = 35.9 \text{ fb}^{-1}$	QCD	$t\bar{t}$	W+jets	Other	All bkg.	$m_{\tilde{g}} = 1600 \text{ GeV}$
$H_T > 1200 \text{ GeV}$	$1.615 \times 10^7$	$9.76 \times 10^4$	$2.718 \times 10^5$	$2.965 \times 10^4$	$(1.655 \pm 0.007) \times 10^7$	$2.8 \times 10^2$
$N_{\text{leps}} = 1$	$1.11 \times 10^4$	$1.292 \times 10^4$	$2.502 \times 10^4$	$4.48 \times 10^3$	$(5.35 \pm 0.01) \times 10^4$	$7.9 \times 10^1$
$N_b \geq 1$	3240	10340	4990	2150	$20725 \pm 80$	74
$N_{\text{jets}} \geq 4$	2770	9920	3740	1870	$18304 \pm 70$	74
$M_J > 500 \text{ GeV}$	810	3658	1120	574	$6162 \pm 40$	67
$M_J > 800 \text{ GeV}$	99	360	150	75	$685 \pm 9$	47
$N_{\text{jets}} \geq 8$	38	200	42	29	$309 \pm 7$	36
$M_J > 1000 \text{ GeV}$	11	43.0	11.3	7.9	$73 \pm 2$	22.6
$N_b \geq 3$	0.7	6.2	0.5	1.1	$8.5 \pm 0.6$	8.9
	QCD	$t\bar{t}$	W+jets	Other	All bkg.	$m_{\tilde{g}} = 1600 \text{ GeV}$

Table 7.1: Expected yields in  $35 \text{ fb}^{-1}$  from simulations of SM and signal processes. Rows above the horizontal line correspond to requirements in the baseline selection, while those below correspond to additional kinematic cuts.

The  $H_T > 1200 \text{ GeV}$  cut sets the hadronic energy scale of the selected events and reduces contributions from processes other than QCD,  $t\bar{t}$ , and W + jets. At this point, the dominate background is QCD and is significantly reduced by selecting events with  $N_{\text{leps}} = 1$ , which leaves the QCD,  $t\bar{t}$ , and W + jets contributions similar in scale. In order to create a  $t\bar{t}$  dominant background,  $N_b \geq 1$  is required as  $t\bar{t}$  events have at least two b-quark jets, while QCD and W + jets contributions largely pass the selection by the mistagging of at least one jet. Finally, the  $N_{\text{jets}} \geq 4$  and  $M_J > 500 \text{ GeV}$  cuts are applied in order to further increase the  $t\bar{t}$  purity of the analysis region.

A benefit of these selections is that the background is dominated by a single process,  $t\bar{t}$ , which reduces the complexity of the background prediction. This is especially necessary as, after these cuts, the analysis region is on the kinematic tails of SM distributions where the physics is less well-known and correspondingly less well-modelled, typically requiring data-driven background predictions.

Lastly, the baseline selection requires that events pass a series of filters designed to remove poorly reconstructed events. These filters remove events with noise in the HCAL or ECAL, beam halo effects, jets that fail to pass quality criteria, and events with zero good PVs.

A final note of interest is that there is no requirement on the  $E_T^{\text{miss}}$ , making this

analysis sensitive to BSM models other than MFV SUSY that produce either little or no  $E_T^{\text{miss}}$  in an event. While the T1tbs model is used as a benchmark for interpreting results, to take advantage of this feature, this search is structured to be generically sensitive to high-mass signatures with large jet and bottom quark jet multiplicities, which are potential features of other BSM models.

## 7.2 Trigger Efficiency

The data sample used in this analysis is obtained by selecting events that pass a loose HLT selection. In order to avoid biasing the selected sample, the HLT requirements must be significantly loose enough that the selection efficiency is as high as possible and independent of any kinematic properties. In particular, events must pass an OR of the HLT\_PFT900 trigger, which requires an online- $H_T$  of at least 900 GeV and the HLT\_PFJet450 trigger, which at least one jet with online- $p_T$  above 450 GeV.

Figure 7.2 shows the performance of the HLT\_PFT900 trigger as a function of  $H_T$  during the first  $27.3 \text{ fb}^{-1}$  (Runs B-G, top-left), last  $8.7 \text{ fb}^{-1}$  (Run H, top-right), and full dataset (Runs B-H, bottom). The trigger performances are measured in a data sample collected using the HLT\_Ele27\_WPTight trigger and offline requirements of at least one electron and at least 4 jets. While the trigger efficiency for Runs B-G is 100% after the trigger plateau of roughly  $H_T = 1000$  GeV, the trigger efficiency only performs with 80% efficiency in Run H. This inefficiency was caused by an issue with an updated trigger implementation that erroneously excluded high  $p_T$  jets from the online- $H_T$  calculation. This effect corresponds to an overall trigger efficiency of 95%, corresponding to a loss of about  $2 \text{ fb}^{-1}$  of data.

In order to recover this inefficiency, events passing the HLT\_PFJet450 trigger are included in the collected data sample. To pass this trigger, events must have very high  $p_T$

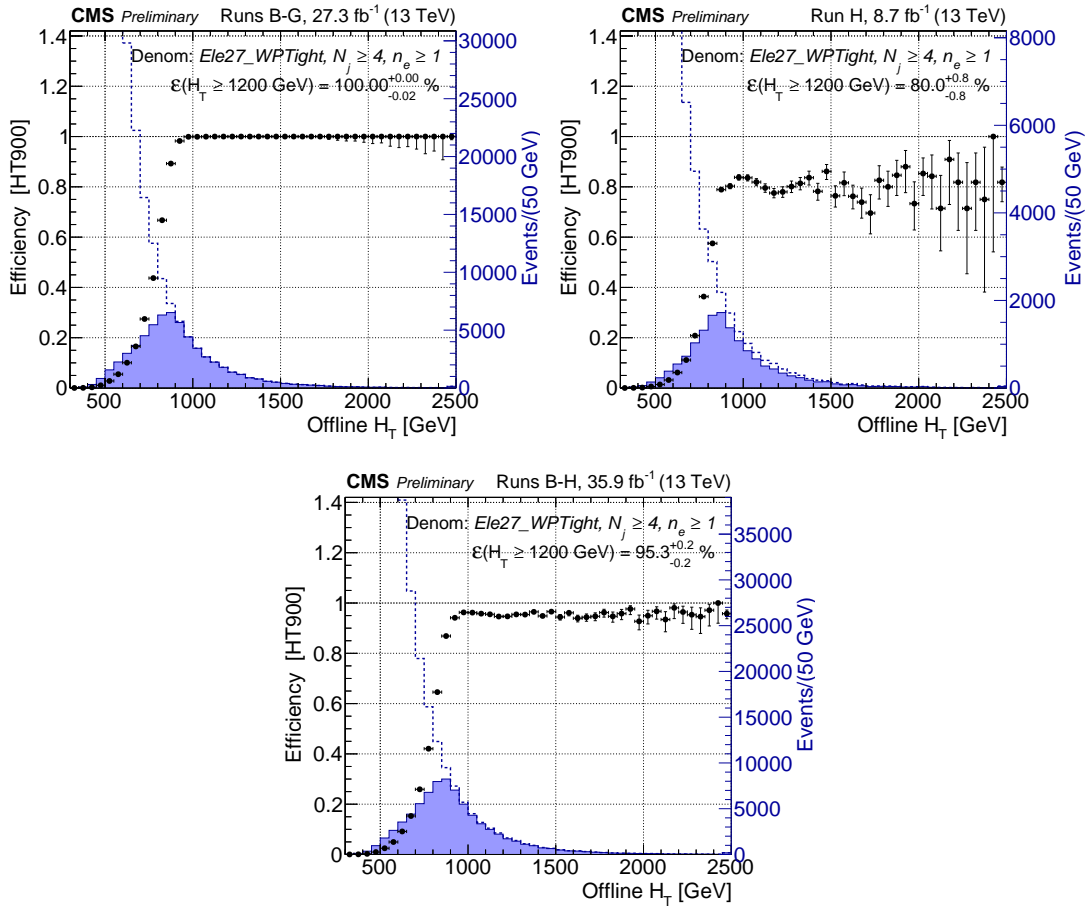


Figure 7.2: Trigger efficiency for HLT\_PFHT900 as a function of  $H_T$  in Runs B-G (top-left), Run H (top-right), and full dataset (bottom). The efficiencies are measured using a data sample collected with the HLT\_Ele27\_WPTight trigger and an offline requirement of at least one electron and at least four jets.

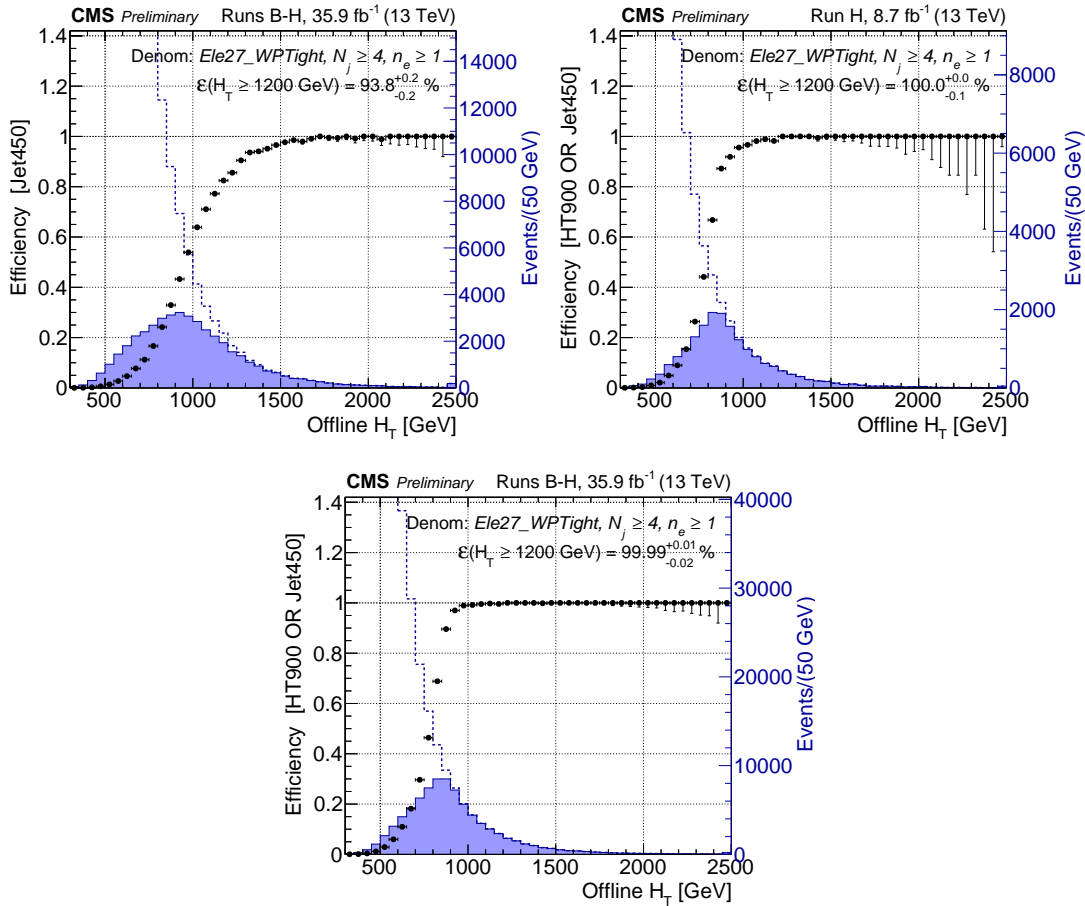


Figure 7.3: Trigger efficiency as a function of  $H_T$  for HLT\_PFJet450 in the full dataset (top-left) and for the combination of HLT\_PFHT900 and HLT\_PFJet450 in Run H (top-right) and the full dataset (bottom). The efficiencies are measured using a data sample collected with the HLT\_Ele27\_WPTight trigger and an offline requirement of at least one electron and at least four jets.

jets, i.e.  $\gtrsim 450$  GeV, which provides complementary efficiency where the HLT\_PFHT900 trigger is inefficient. Figure 7.3 shows the performance as a function of  $H_T$  of the HLT\_PFJet450 trigger in Runs B-H (top-left) and the combination of the HLT\_PFHT900 and HLT\_PFJet450 in Run H (middle) and in the full dataset (bottom), measured with a dataset collected with HLT\_Ele27\_WPTight and offline requirements of at least one electron and at least 4 jets. The inclusion of the HLT\_PFJet450 trigger restores the overall trigger efficiency to essentially 100% in both Run H and the entire dataset.

This trigger efficiency, however, does not necessarily correspond to the efficiency for signal events. A lower bound on the signal efficiency can be estimated by considering that the `HLT_PFTightJet450` trigger is fully efficient for jets with  $p_T > 500$  GeV and 80%-95% of simulated signal events (depending on the mass of the gluino) have a jet with  $pT > 500$  GeV. Thus, in the worst case scenario, the addition of the `HLT_PFTightJet450` trigger is still expected to recover at least 85% of the lost signal efficiency in Run H. This results in an efficiency of at least 97% in Run H and over 99% for the full dataset for signal events.

Lastly, to ensure that there is no kinematic bias in the trigger efficiency either inherently or residually from effects of the online- $H_T$  calculation issue, the trigger efficiency is measured as a function of  $M_J$ ,  $N_{\text{jets}}$ , and  $N_b$ . The measurements, shown in Figure 7.4 are done in a data sample collected with the `HLT_Ele27_WPTight` trigger and an offline requirement of at least one electron, at least four jets, and  $H_T > 1200$  GeV. The resulting efficiencies are all consistent with 100% and no kinematic bias is observed.

## 7.3 Analysis Binning

After the baseline selection, the background is dominated by  $t\bar{t}$  events with small contributions from  $W + \text{jets}$  and QCD production. There are additional rare background processes, jointly noted as “Other”, with tiny, but non-zero contributions that arise from single top quark,  $t\bar{t}W$ ,  $t\bar{t}Z$ ,  $t\bar{t}H$ ,  $t\bar{t}\bar{t}\bar{t}$ , and Drell-Yan production.

In order to further increase the signal-to-background ratio, as well as create background-dominated control regions, the analysis region is binned with respect to  $N_{\text{jets}}$  and  $M_J$ . The  $N_{\text{jets}}$  bins are defined as  $4 \leq N_{\text{jets}} \leq 5$ ,  $6 \leq N_{\text{jets}} \leq 7$ , and  $N_{\text{jets}} \geq 8$ . Each  $N_{\text{jets}}$  bin is further split into bins of  $500 < M_J \leq 800$  GeV,  $800 < M_J \leq 1000$  GeV, and  $M_J > 1000$  GeV, with the exception of the  $4 \leq N_{\text{jets}} \leq 5$  bin for which the two highest

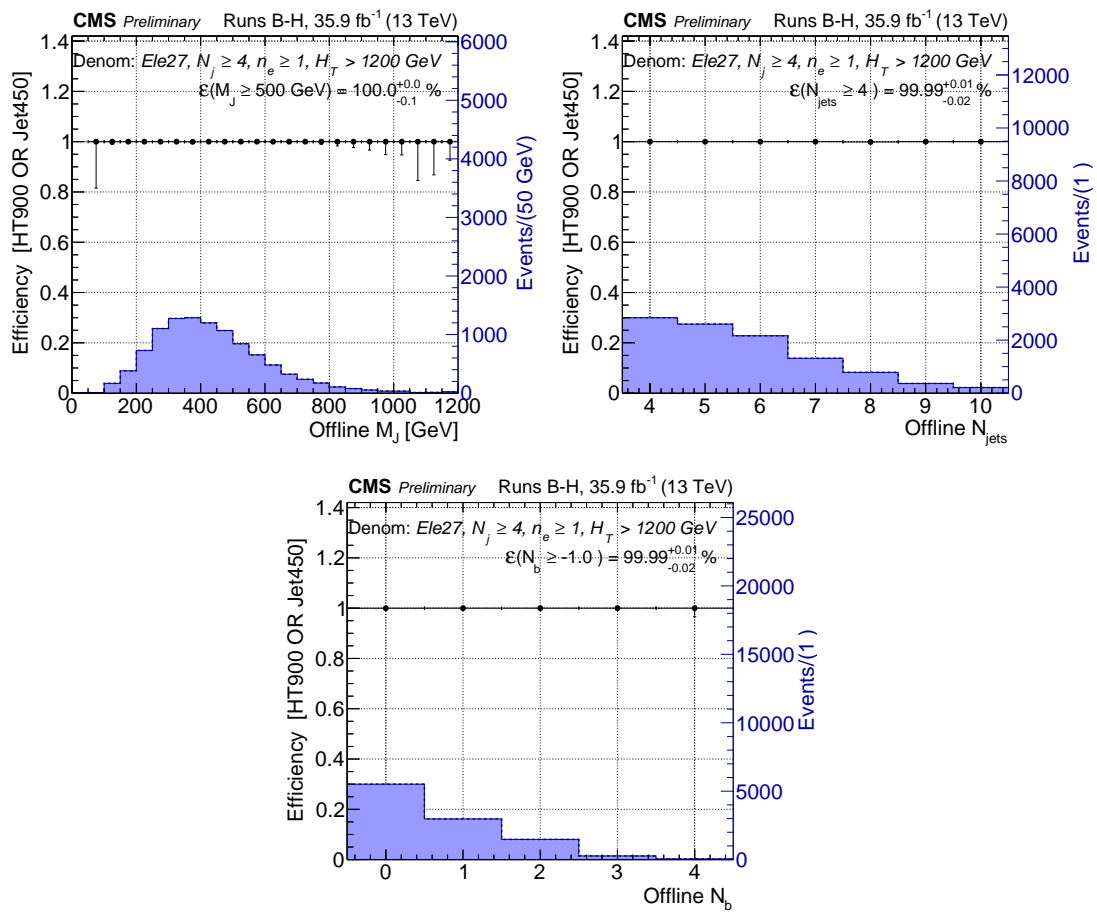


Figure 7.4: Trigger efficiency as a function of  $M_j$  (top-left),  $N_{\text{jets}}$  (top-right), and  $N_b$  (bottom) for the combination of the HLT\_PFT900 and HLT\_PFJet450 triggers in the full dataset. The efficiencies are measured using a data sample collected using the HLT\_Ele27\_WPTight trigger and an offline requirement of at least one electron, at least four jets, and  $H_T > 1200$  GeV.

$M_J$ [GeV]	$N_{\text{jets}}$		
	4–5	6–7	$\geq 8$
500–800	CR	CR	SR
800–1000	CR	SR	SR
$> 1000$	SR	SR	SR

Figure 7.5: Illustration depicting the  $N_{\text{jets}}$ ,  $M_J$  binning after the baseline selection, with control and signal region bins denoted by “CR” and “SR”, respectively.

$M_J$  bins are combined due to the limited data sample size in the  $M_J \geq 1000$  GeV bin. A diagram representing this binning is shown in Figure 7.5. The low- $N_{\text{jets}}$ , low- $M_J$  bins are expected to be background-dominated and are used as control regions for constraining systematics and for validating the prediction methodology, while the high- $N_{\text{jets}}$ , high- $M_J$  bins are used as signal regions.

Within each  $N_{\text{jets}}$  and  $M_J$  bin, the  $N_b$  distribution is examined for evidence of new physics and is separated into bins of  $N_b = 1, 2, 3$ , and  $\geq 4$ . The two lowest  $N_b$  bins are used to provide constraints on the background normalizations and systematic uncertainties, while the higher  $N_b$  bins are the most sensitive to potential signals due to its larger signal-to-background ratios.

In total, this analysis has 8 kinematic regions—3 control and 5 signal regions with four  $N_b$  bins per kinematic region. The simulated  $N_b$  distribution of the SM background processes and a signal model with  $m_{\tilde{g}} = 1600$  GeV for the control and signal regions are shown in Figure 7.6 and Figure 7.7, respectively.

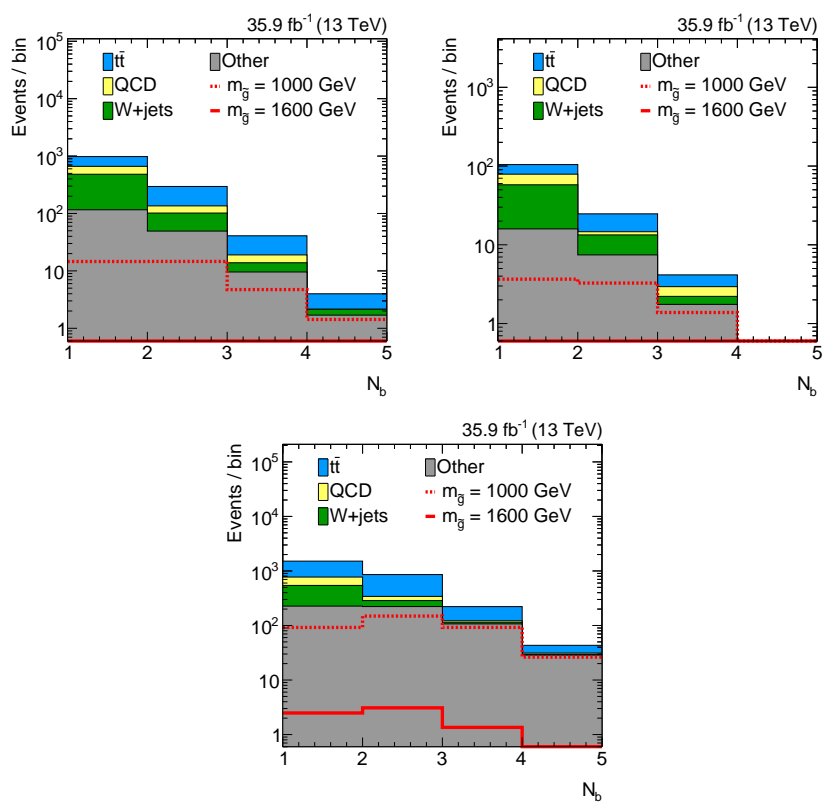


Figure 7.6: The simulated  $N_b$  distribution for background and signal processes in the control region bins. The top-left plot corresponds to the  $4 \leq N_{\text{jets}} \leq 5, 500 \leq M_J \leq 800 \text{ GeV}$  bin, the top-right plot to the  $5 \geq N_{\text{jets}} \geq 6, M_J \geq 800 \text{ GeV}$  bin, and the bottom plot to the  $6 \leq N_{\text{jets}} \leq 7, 500 \leq M_J \leq 800 \text{ GeV}$  bin.

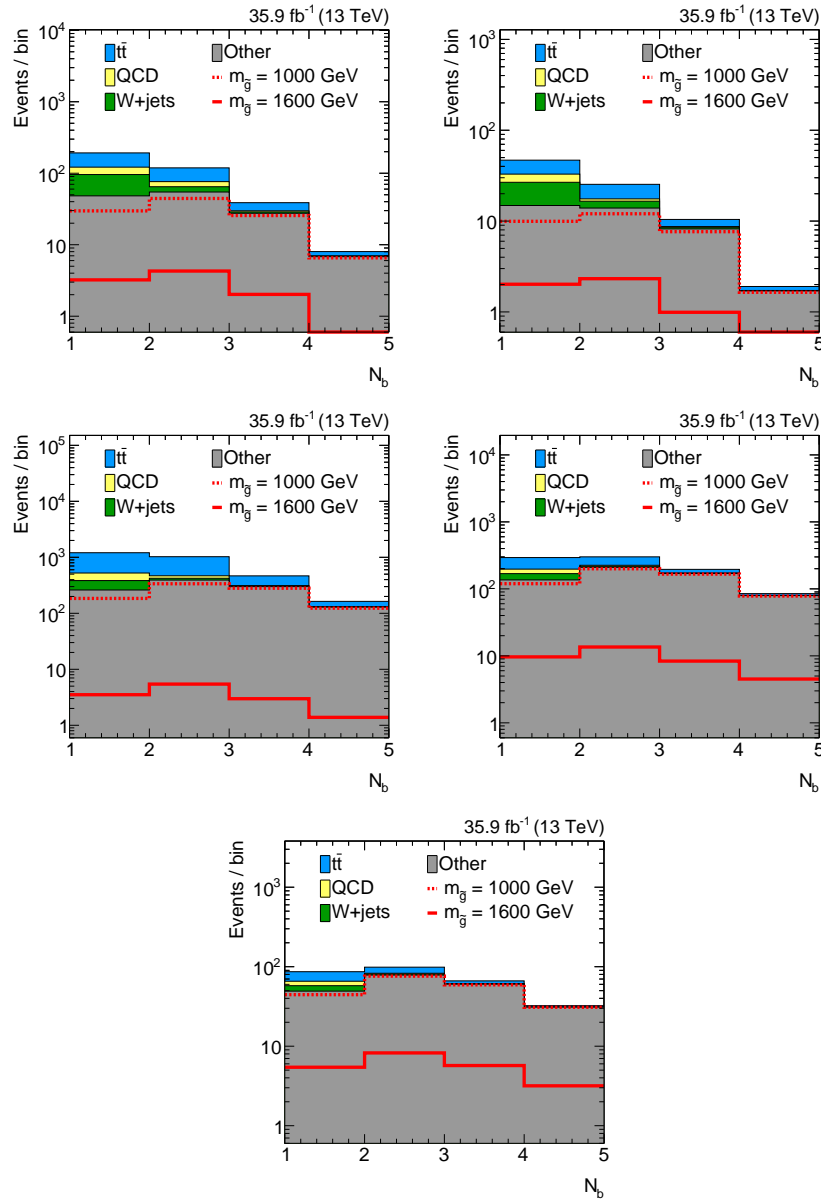


Figure 7.7: The simulated  $N_b$  distribution for background and signal processes in the signal region bins. The top-left plot corresponds to the  $6 \leq N_{\text{jets}} \leq 7$ ,  $800 \leq M_J \leq 1000 \text{ GeV}$  bin, the top-right plot to the  $6 \geq N_{\text{jets}} \geq 7$ ,  $M_J \geq 1000 \text{ GeV}$  bin, the middle-left plot to the  $N_{\text{jets}} \geq 8$ ,  $500 \leq M_J \leq 800 \text{ GeV}$  bin, the middle-right plot to the  $N_{\text{jets}} \geq 8$ ,  $800 \leq M_J \leq 1000 \text{ GeV}$ , and the bottom plot to the  $N_{\text{jets}} \geq 8$ ,  $M_J \geq 1000 \text{ GeV}$  bin.

## **Part IV**

### **The Search**

# Chapter 8

## Background Prediction

### 8.1 Overview

This analysis seeks to find evidence of new physics by searching for deviations from the SM in the  $N_b$  distribution. In order to do this, it is essential to be able to robustly and accurately predict both the normalization and shape of the  $N_b$  distribution. To obtain these predictions, a global maximum-likelihood fit is performed. This fit is carried out both for a background-only hypothesis and for signal-plus-background hypotheses, in which a signal contribution is extracted in addition to the contributions of SM background processes. The model is constructed using the poisson probabilities of the bin contents of the  $N_b$  distribution for all  $N_{\text{jets}}$ ,  $M_J$  regions, while systematic uncertainties are applied as nuisance parameters.

As the kinematic tails of the  $N_{\text{jets}}$  and  $M_J$  variables are difficult to model reliably, the  $t\bar{t}$  and QCD normalizations are individually allowed to (almost) freely vary in each  $(N_{\text{jets}}, M_J)$  bin. The  $t\bar{t}$  normalizations are constrained in each bin by the low- $N_b$  bins, while the QCD normalizations are constrained by control regions with no identified leptons ( $N_{\text{leps}} = 0$ ). The overall  $W + \text{jets}$  normalization is determined from data and is allowed to vary across  $N_{\text{jets}}$  bins by amounts measured using a kinematically similar  $Z + \text{jets}$  sample, while the normalization of Other is largely taken from simulation, as its contribution is

small in the regions considered. Further details on the measurement of the normalizations are given in the following sections.

Once the SM background processes are normalized accordingly, further corrections to the  $N_b$  shape are relatively small. The nominal  $N_b$  shape prediction for each process is taken from simulation with data-to-simulation correction factors (SFs) applied for the tagging efficiency of heavy- and light-flavor jets [70, 14]. This shape is allowed to vary in order to assess the impact of mismodeling of relevant parameters, such as the rate of gluon splitting to  $b\bar{b}$  and the b-tagging SFs. The appropriate ranges for these parameters are determined based on measurements in dedicated control samples and then constrained by a simultaneous fit across all bins of  $N_{\text{jets}}$  and  $M_J$  in a correlated manner. A detailed discussion of these variations and their measurements is given in ??.

## 8.2 $t\bar{t}$ and QCD Normalizations

The  $t\bar{t}$  and QCD normalizations are allowed to float in each  $(N_{\text{jets}}, M_J)$  bin but with a loose constraint across  $M_J$  bins discussed in the following subsection 8.2.1. The largest constraint on the  $t\bar{t}$  normalization in each bin is the background-dominated  $N_b \leq 2$  bins, while the QCD normalization in each bin is mostly constrained by corresponding bins in a similar 0-lepton kinematic region selected by requiring  $N_{\text{leps}} = 0$ ,  $H_T > 1500$  GeV,  $M_J > 500$  GeV,  $N_{\text{jets}} \geq 6$ , and  $N_b \geq 1$ . The higher  $H_T$  requirement compared to the analysis's baseline selection is imposed in order to account for the extra energy in an event carried by the lepton in the  $N_{\text{leps}} = 1$  selection, while the higher  $N_{\text{jets}}$  selection is imposed in order to account for differences in the  $N_{\text{jets}}$  distribution between the  $N_{\text{leps}} = 1$  and  $N_{\text{leps}} = 0$  samples. This control sample follows the same kinematic binning as the  $N_{\text{leps}} = 1$  regions, except that the  $N_b$  distribution in each bin is integrated in  $N_b$  for  $N_b \geq 1$  and each bin's  $N_{\text{jets}}$  requirement is increased by 2. A diagram representing the

$M_J$ [GeV]	$N_{\text{jets}}$		
	4–5	6–7	$\geq 8$
500–800	CR	CR	SR
800–1000	CR	SR	SR
$> 1000$		SR	SR

Figure 8.1: Diagram depicting the  $N_{\text{jets}}$ ,  $M_J$  binning of the  $N_{\text{leps}} = 0$  QCD control region.

binning of the  $N_{\text{leps}} = 0$  control sample is shown in Figure 8.1. The QCD contribution in a particular  $N_{\text{leps}} = 1$  bin is then constrained by the corresponding  $N_{\text{leps}} = 0$  bin. To avoid biasing the normalization measurement, the small contribution of  $t\bar{t}$  background to the  $N_{\text{leps}} = 0$  control regions is included using the normalization from the corresponding  $N_{\text{leps}} = 1$  bins, while contributions from other processes are taken from simulation.

### 8.2.1 $M_J$ Connection

Due to the large freedom of unconstrained normalization parameters, the fit can be sensitive to rare statistical fluctuations and return unphysical normalization values particularly in bins dominated by  $t\bar{t}$  events. For example, in psuedodata experiments, where data are generated according to the statistical and systematic uncertainties of the pre-fit values, the fit reduced the  $t\bar{t}$  contribution in the  $N_{\text{jets}} \geq 8$ ,  $M_J > 1000$  GeV bin (where statistical uncertainties are largest) to  $\sim 0$  in about  $\sim 1\%$  of the experiments. This can be seen in Figure 8.2 (left) which shows a low tail in the distribution of post-fit  $t\bar{t}$  yields in the  $N_{\text{jets}} \geq 8$ ,  $M_J > 1000$  GeV bin for 1,000 psuedodata experiments. When yields in a bin have a large fluctuation downwards, the fit must lower the normalization of a process to compensate. The QCD,  $W + \text{jets}$ , and Other contributions, however, are largely constrained by other data control samples or taken from simulation, and so the fit uses the freedom to adjust the  $t\bar{t}$  normalization in order to compensate for the fluctuation, leading to the unphysically small values.

In order to avoid this instability, the normalizations of  $t\bar{t}$  and QCD are (independ-

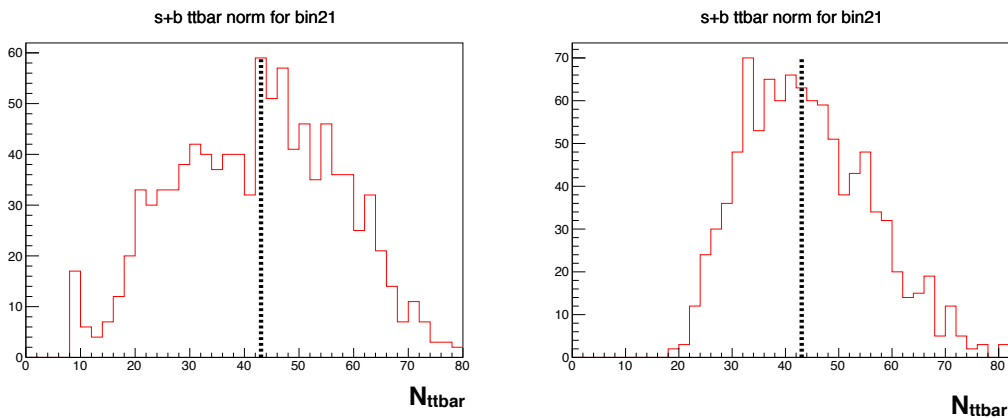


Figure 8.2: Distribution of post-fit yields of  $t\bar{t}$  in the  $N_{\text{jets}} \geq 8$ ,  $M_J > 1000$  GeV bin for 1,000 psuedodata experiments without (left) and with (right) constraints between adjacent  $M_J$  bins. The dotted black line indicates the the pre-fit yield.

dently) connected by log-normal constraints between adjacent  $M_J$  bins. By correlating the normalizations across  $M_J$  bins, the fit's sensitivity to large fluctuations in a single bin is greatly reduced. The size of these connections is motivated by measurements of the data-to-simulation ratio with  $N_b = 1$  events (in order to avoid potential signal contamination) and is particularly chosen to be significantly larger than the uncertainty on the data-to-simulation ratios in order to avoid over-constraining the normalization parameters, while still providing some constraint against unphysical fits. Based on these measurements, shown in Figure 8.3, and criteria, a connection size between adjacent bins of [50%-200%] is chosen.

Figure ?? (right) shows the results of the same 1,000 psuedodata experiments but now with this constraint across  $M_J$  bins applied. The resulting distribution of post-fit  $t\bar{t}$  yields now shows no evidence of unphysical normalizations and appears to be better behaved.

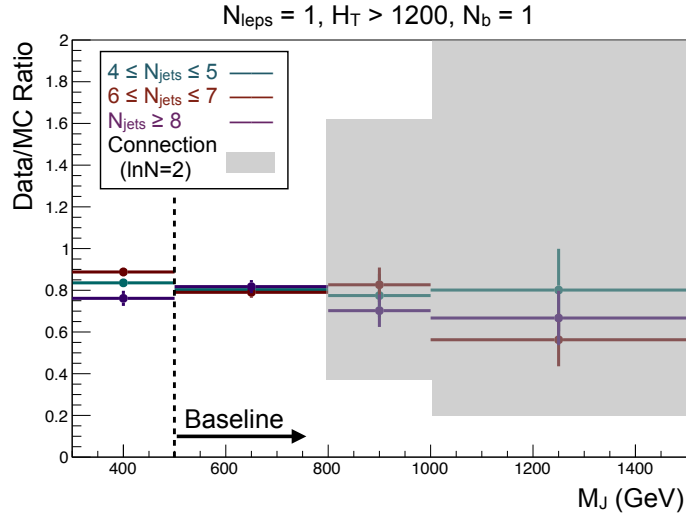


Figure 8.3: Data-to-simulation ratios as a function of  $M_J$  for different  $N_{\text{jets}}$  bins (data points) with a selection of  $N_{\text{leps}} = 1$ ,  $H_{\text{T}} > 1200$  GeV, and  $N_{\text{b}} = 1$  applied. The shaded region corresponds to the size of the  $M_J$  connection in each  $M_J$  bin.

### 8.3 W + jets Normalization

The W + jets background is determined in the fit with one global normalization parameter and two parameters to adjust the bin-to-bin normalization of adjacent  $N_{\text{jets}}$  bins, since the  $N_{\text{jets}}$  shape may not be well-modelled by simulation. The amount the  $N_{\text{jets}}$  shape may vary is based on the data-to-simulation agreement in a kinematically similar Z + jets sample selected with  $N_{\text{leps}} = 2$  (ee or  $\mu\mu$ ),  $H_{\text{T}} > 1200$  GeV,  $M_J > 500$  GeV,  $N_{\text{b}} = 1$ , and  $80 < m_{\ell\ell} < 100$  GeV, where  $m_{\ell\ell}$  is the invariant mass of the two leptons. The  $N_{\text{jets}}$  distribution and data/simulation yields ratio for this sample are shown in Figure 8.4. The resulting variation sizes are 17% between  $4 \leq N_{\text{jets}} \leq 5$  and  $6 \leq N_{\text{jets}} \leq 7$  and 62% between  $6 \leq N_{\text{jets}} \leq 7$  and  $N_{\text{jets}} \geq 8$ . After correcting the  $N_{\text{jets}}$  spectrum, the residual  $M_J$  mismodeling is expected to be small, so no further correction is applied.

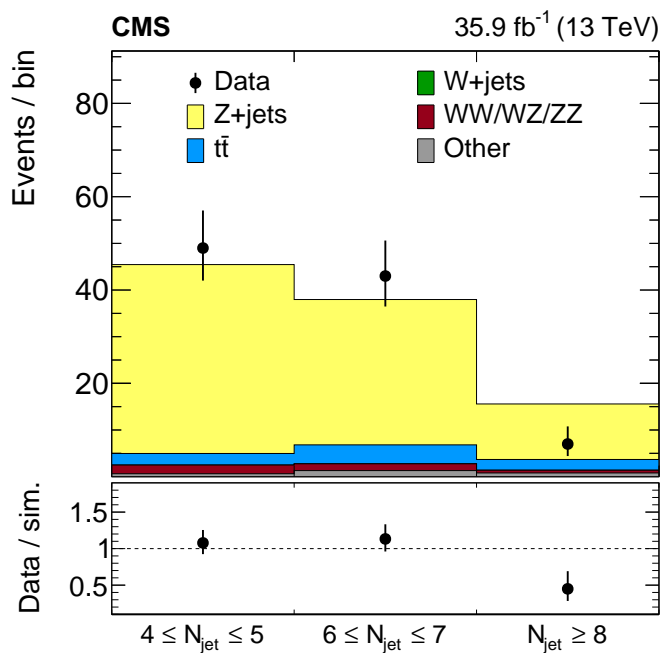


Figure 8.4: Jet multiplicity distribution for data and simulation in a Z + jets control sample selected by requiring  $N_{\text{leps}} = 2$ ,  $H_T > 1200$  GeV,  $M_J > 500$  GeV,  $N_b = 1$ , and  $80 < m_{\ell\ell} < 100$  GeV. The total yield from simulation is normalized to the number of events in data. The uncertainty in the ratio of data to simulation yields (lower panel) is statistical only.

## 8.4 Other Normalization

The nominal normalization for Other is largely taken from simulation, as its contribution is less than 20% in every bin with typical values  $\lesssim 5\%$ . It is, however, allowed to vary according to statistical and systematic uncertainties.

# Chapter 9

## Systematic Uncertainties

The nominal simulated shape of the  $N_b$  distribution is allowed to vary by the inclusion of systematic uncertainties. Each uncertainty is incorporated in the fit with template  $N_b$  histograms to account for the effects of the systematic variation and a nuisance parameter  $\theta$  to control the variation amplitude. The nuisance parameters are subject to Gaussian constraints, normalized so that  $\theta = 0$  corresponds to the nominal  $N_b$  shape and  $\theta = \pm 1$  corresponds to  $\pm 1$  standard deviation (s.d.) variation of the systematic uncertainty. These uncertainties affect only the  $N_b$  shape for  $t\bar{t}$ , QCD, and W+jets backgrounds, because their normalizations are determined from data, while for the other (subleading) backgrounds the uncertainties affect both the  $N_b$  shape and normalization.

### 9.1 Gluon Splitting Rate

The primary source of systematic uncertainty is on the modelling of the rate of gluon splitting, as events with a gluon splitting to  $b\bar{b}$  provide an additional source of b quarks in events. As this process may not be properly simulated, constraining the splitting rate in data is crucial for establishing a robust prediction of the  $N_b$  distribution. The dominant contribution of this effect is due to gluons that split specifically to b quark pairs, so the phrase “gluon splitting” will hereafter refer exclusively to gluon splitting to  $b\bar{b}$ . One way

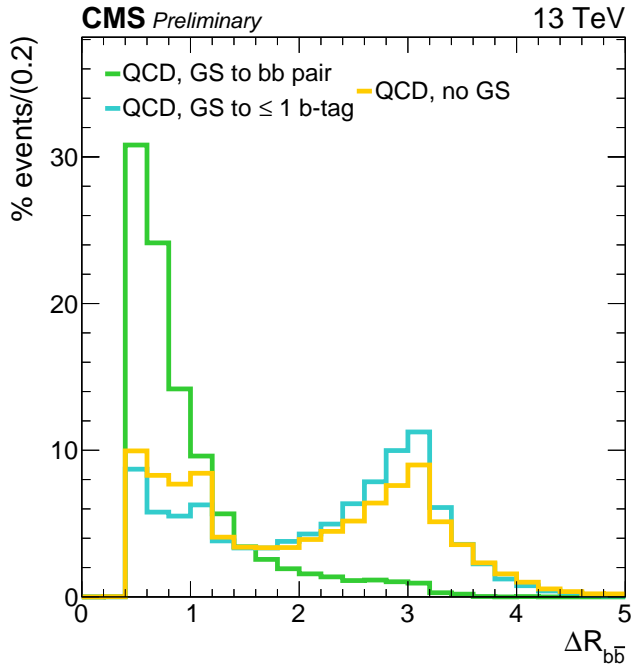


Figure 9.1: The  $\Delta R_{b\bar{b}}$  distribution shapes for the three gluon splitting categories: Events with a pair of b-tagged jets resulting from gluon splitting (green), events with a gluon splitting yielding fewer than 2 b-tagged jets (blue), and events without a gluon splitting to  $b\bar{b}$ . These events are selected by requiring  $N_{\text{leps}} = 0$ ,  $H_T > 1500$  GeV,  $M_J > 500$  GeV,  $N_{\text{jets}} \geq 4$ , and  $N_b = 2$ .

to select a data sample enriched in gluon splitting events is to use the  $\Delta R_{b\bar{b}}$  distribution, where  $\Delta R_{b\bar{b}}$  is defined as the  $\Delta R$  between two b-tagged jets, as pairs of b-tagged jets resulting from the same gluon splitting tend to have smaller values of  $\Delta R_{b\bar{b}}$  than pairs resulting from hard scatter b-quarks or fakes. This can be seen in Figure 9.1, which shows the dR<sub>b̄b̄</sub> distribution in simulated QCD events with  $N_b = 2$  for three important categories: Events that have a correlated pair of b-tagged jets originating from a gluon splitting (green, denoted GSbb) populate the low- $\Delta R_{b\bar{b}}$  region, while events without gluon splitting (yellow, denoted noGS) or where the splitting yields zero one b-tagged jets (blue, denoted GSb) populate the low-and high- $\Delta R_{b\bar{b}}$  regions roughly equally.

Gluon splittings can contribute less than 2 b-tagged jets either because the quarks

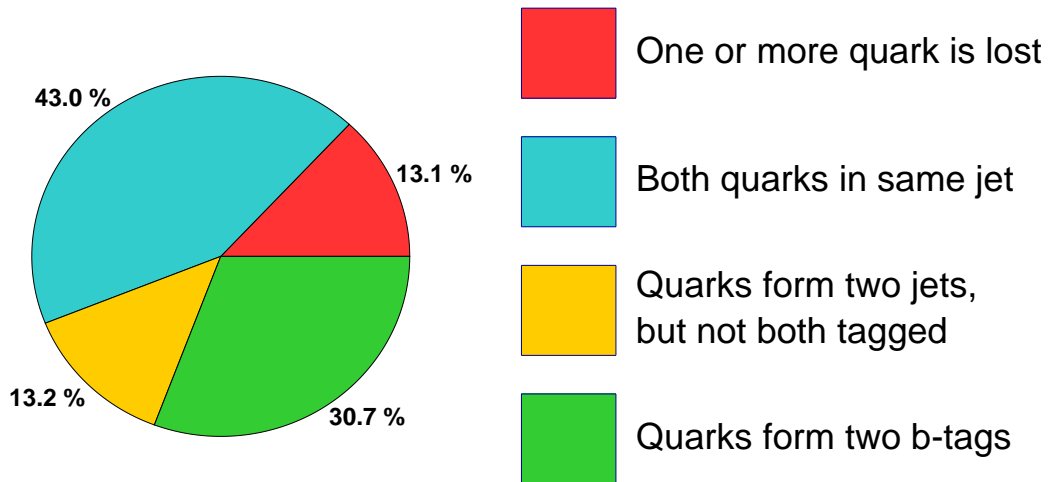


Figure 9.2: The relative fraction of the possible final states that occur from gluon splitting to  $b\bar{b}$  for events satisfying  $N_{\text{leps}} = 0$ ,  $H_T > 1500$  GeV,  $M_J > 500$  GeV,  $N_{\text{jets}} \geq 4$ , and  $N_b = 2$ .

are collimated into a single jet, one of the b-tagged jets is not tagged, or because one of the jets fails to pass the jet selection criteria, typically because it is too soft. The relative fractions of these contributions is shown in Figure 9.2.

The gluon splitting rate is constrained by fitting the  $\Delta R_{b\bar{b}}$  distribution by using the difference in shapes of the GSbb, GSb, and noGS categories. This fit varies the normalization of the GSbb and GSb (varied together) and the noGS contributions in order to extract the relative contributions of events with and without a gluon splitting. It is performed in four equal bins in the range of  $0 \leq \Delta R_{b\bar{b}} < 4.8$  with events selected by requiring  $N_{\text{leps}} = 0$ ,  $H_T > 1500$  GeV,  $N_b = 2$ ,  $N_{\text{jets}} \geq 4$ , and  $M_J > 500$  GeV as the gluon splitting signal in a  $N_{\text{leps}} = 1$  control sample is contaminated by b quarks from the decay of top quarks. Additionally, the  $N_{\text{leps}} = 0$  control sample is formed from a subset of the data that is selected to be most stable in the b tagging algorithm performance, since the precision of the  $\Delta R_{b\bar{b}}$  fit is not limited by the data sample size. This choice isolates the physical effects of gluon splitting from the potential time dependence of the

	Nominal	$M_J > 800 \text{ GeV}$	$4 \leq N_{\text{jets}} \leq 5$	$6 \leq N_{\text{jets}} \leq 7$	$8 \leq N_{\text{jets}} \leq 9$	$N_{\text{jets}} \geq 10$
GS	$0.77 \pm 0.09$	$0.70 \pm 0.38$	$0.80 \pm 0.32$	$0.76 \pm 0.14$	$0.75 \pm 0.16$	$0.95 \pm 0.36$
No GS	$1.21 \pm 0.08$	$1.28 \pm 0.35$	$1.15 \pm 0.26$	$1.22 \pm 0.13$	$1.24 \pm 0.15$	$1.05 \pm 0.36$

Table 9.1: Gluon splitting weights derived in the nominal fit, a variation with a requirement of  $M_J > 800 \text{ GeV}$ , and 4 variations in bins of  $N_{\text{jets}}$  (with the nominal  $M_J > 500 \text{ GeV}$  requirement.)

b tagging performance due to variations in experimental conditions, which are separately incorporated by the b-tag scale factor uncertainties.

The  $\Delta R_{b\bar{b}}$  fit extracts a weight of  $0.77 \pm 0.09$  for gluon splitting events and a weight of  $1.21 \pm 0.08$  for non-gluon splitting events. The post-fit distributions are shown in Figure 9.3. The GSbb and GSb categories are plotted separately to demonstrate the difference in shapes. The discrepancy in the last bin does not significantly impact the fit because the higher yield bins at lower values of  $\Delta R_{b\bar{b}}$  constrain the fit. The deviations of these weights from unity, summed in quadrature with their post-fit uncertainty, are used to form the  $\pm 1$  s.d. variations of the gluon splitting rate nuisance parameter by applying weights of  $1 \pm 0.25$  to gluon splitting events and  $1 \mp 0.22$  to non-gluon splitting events in an anti-correlated manner. The fit results are used as a measure of the uncertainty on modelling of the GS rate as opposed to a correction to the central value, since the  $\Delta R_{b\bar{b}}$  variable may not be a perfect proxy for the GS rate. Figure 9.4 shows the effect of the  $\pm 1$  s.d. variations on the  $N_b$  distribution of  $t\bar{t}$  for the two most sensitive bins.

In order to test the stability of the fit results and the dependence of the gluon splitting weights across kinematic regions, the  $\Delta R_{b\bar{b}}$  fit is repeated both with a higher  $M_J$  threshold and with different  $N_{\text{jets}}$  bins. The resulting weights are shown in Table ?? and are all consistent with those of the nominal fit.

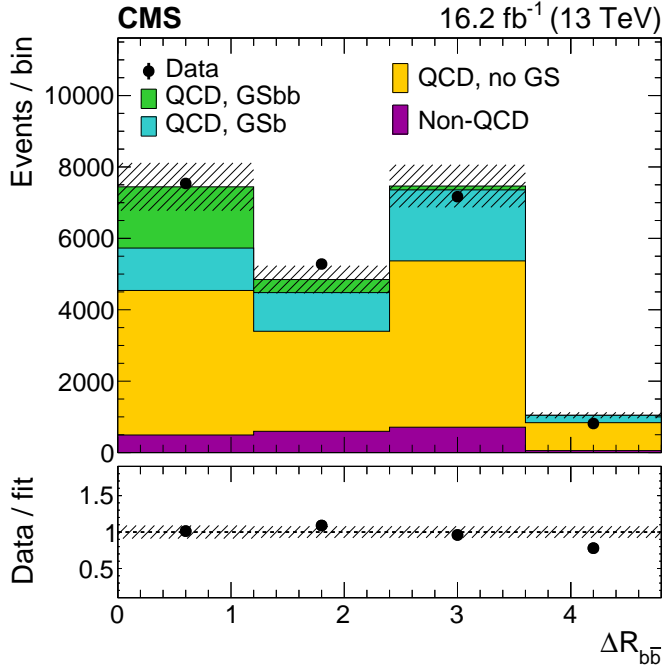


Figure 9.3: Post-fit  $\Delta R_{b\bar{b}}$  distributions in a selection with  $N_{\text{leps}} = 0$ ,  $H_T > 1500 \text{ GeV}$ ,  $M_J > 500 \text{ GeV}$ ,  $N_{\text{jets}} \geq 4$ , and  $N_b = 2$  with the post-fit uncertainty represented by a hatched band. The ratio of data to simulation yields is shown in the lower panel.

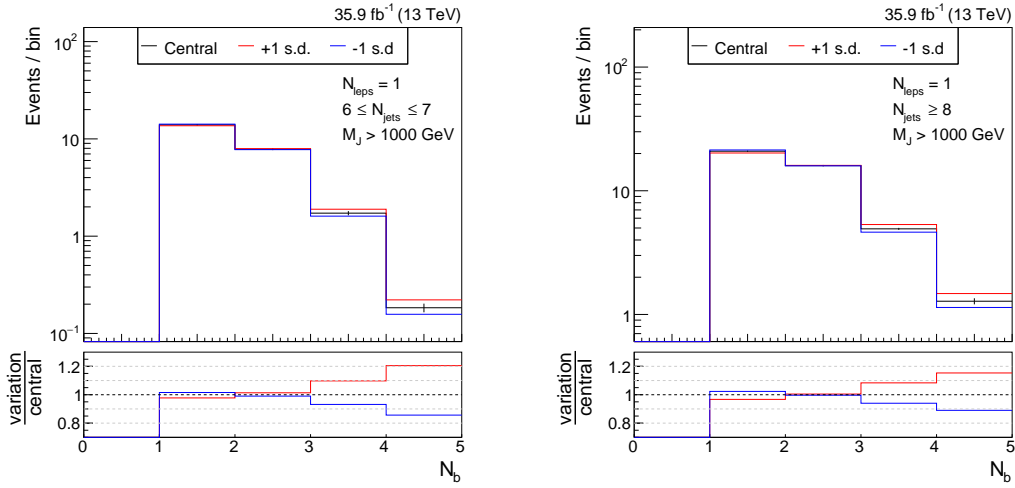


Figure 9.4: Effect of the  $\pm 1$  s.d. variations of the gluon splitting rate on the  $N_b$  distribution in  $t\bar{t}$  events for the two most sensitive bins: ( $N_{\text{jets}} \geq 8$ ,  $800 < M_J \leq 1000 \text{ GeV}$ ) (left) and ( $N_{\text{jets}} \geq 8$ ,  $M_J > 1000 \text{ GeV}$ ) (right). Event yields are normalized to that expected in  $35.9 \text{ fb}^{-1}$  of data.

## 9.2 b-tagging Data-to-simulation Scale Factors

Another significant systematic uncertainty is the uncertainty in the data-to-simulation scale factors (SF) for b tagging efficiency and mistag rates. Simulating the b-tagging algorithm relies on understanding the detailed behavior of the detector and also accurate modelling of the parton shower and hadronization, both of which are non-trivial. Therefore, it is important to measure the b tagging efficiencies and mistag rates in data and correct the simulation to match.

The difference between data and simulation is corrected for by using a per jet data-to-simulation SF

$$SF_f = \varepsilon_f^{data}(p_T)/\varepsilon_f^{sim.}(p_T). \quad (9.1)$$

where  $\varepsilon_f^{data}(p_T)$  and  $\varepsilon_f^{sim.}(p_T)$  are the tagging efficiencies for a jet with flavor  $f$  as a function of  $p_T$  in data and simulation, respectively. No dependence on  $\eta$  is derived due to limited data sample sizes. In simulation, the efficiency is determined by matching jets to their generated hadron to determine their flavor and then measuring how many of those jets are correctly tagged. In data, this is done by using control regions determined by specific selection requirements that produce pure samples of a certain flavor of jets while not biasing the jets with respect to variables used in the b tagging algorithm.

The probability to tag a light-flavor or gluon jet (light jet), is measured in an inclusive QCD sample. This sample is selected through a series of triggers that require at least one jet over a certain  $p_T$  threshold, the lowest being 40 GeV.

The probability to tag a charm-flavor jet (c jet) is determined by measurements in two charm-enriched control regions. The first control region is formed by selecting events in which a charm quark is produced in association with a W boson. The main contributions

to this process is from  $s + g \rightarrow W^- + c$  and  $\bar{s} + g \rightarrow W^+ + \bar{c}$ , where a key property is that the  $W$  boson and quark have oppositely signed electrical charges. The dominant background is  $W + q\bar{q}$  events, which are produced an equal amount of events with same- and opposite-signed  $W$  boson and quark pairs. Thus, this background is removed by measuring its contribution in the same-sign channel and subtracting it from the opposite-sign channel, resulting in a pure  $W + c$  channel. The second charm-enriched control region is created by selecting single-lepton  $t\bar{t}$  events. As hadronically-decaying  $W$  bosons decay to a charm quark about 50% of the time, about one of two single-lepton  $t\bar{t}$  events will contain a charm quark. Finally, measurements in these two regions are combined using the best linear unbiased estimator (BLUE) method, described in Reference [100].

The probability to tag a b-flavor jet (b jet) is computed using QCD and  $t\bar{t}$  control regions. The QCD control regions are enriched in b quarks by requiring that at least one jet contains a muon with  $p_T > 5$  GeV, which takes advantage of the high branching fraction to leptons of b hadrons. In the  $t\bar{t}$ -dominated regions, there are two b quarks per event, due to the decay of the two top quarks, and the b quark purity is further enhanced by limiting the number of non-b jets in the event through the requirement that either one or both of the  $W$  bosons decays leptonically, creating independent single-lepton and di-lepton control regions. Multiple measurements are made in these regions and are then combined through the BLUE method.

The resulting SFs, including their uncertainties, are shown in Figure ???. A complete discussion of how the SF measurements are made can be found in Reference [14].

The systematic uncertainties on the  $N_b$  shape are assessed by the  $\pm 1$  s.d.  $N_b$  templates resulting from varying the SFs according to their uncertainties. Because the b and c jet SFs have correlated uncertainties, they are conservatively varied together, creating one set of templates. The light-flavor SFs are uncorrelated with the b and c jet SFs and are

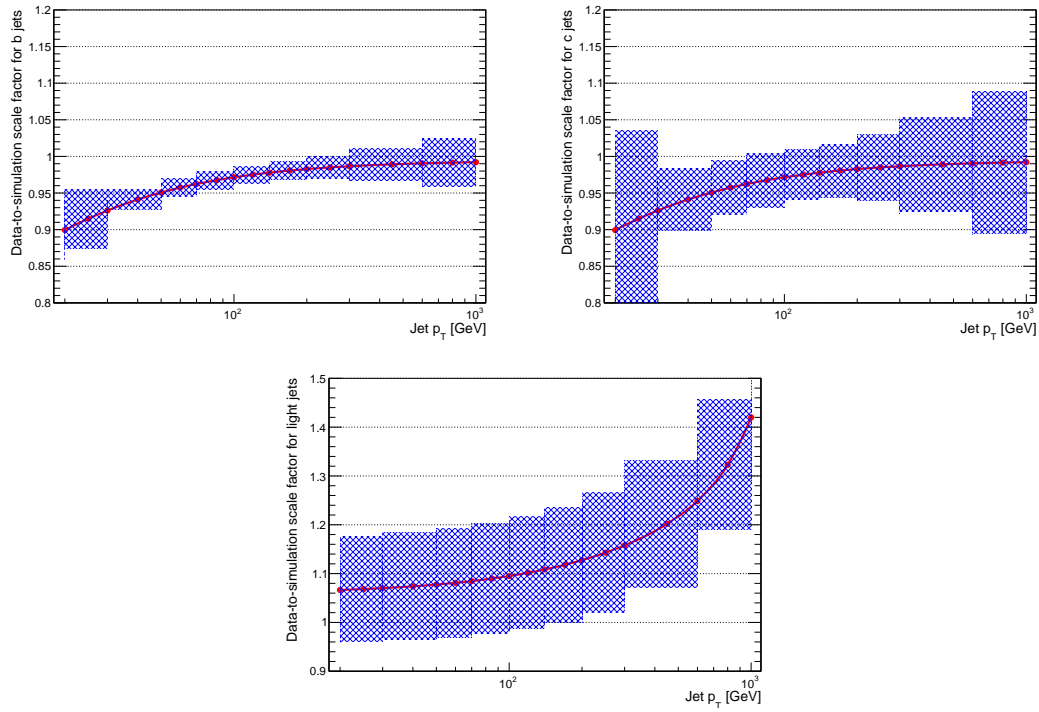


Figure 9.5: The data-to-simulation scale factors for the tagging efficiency of b-flavor jets (top-left), charm-flavor jets (top-right), and light-flavor or gluon jets (bottom) are shown as a function of jet  $p_T$ . The associated uncertainty with each scale factor is shown as a blue hashed band.

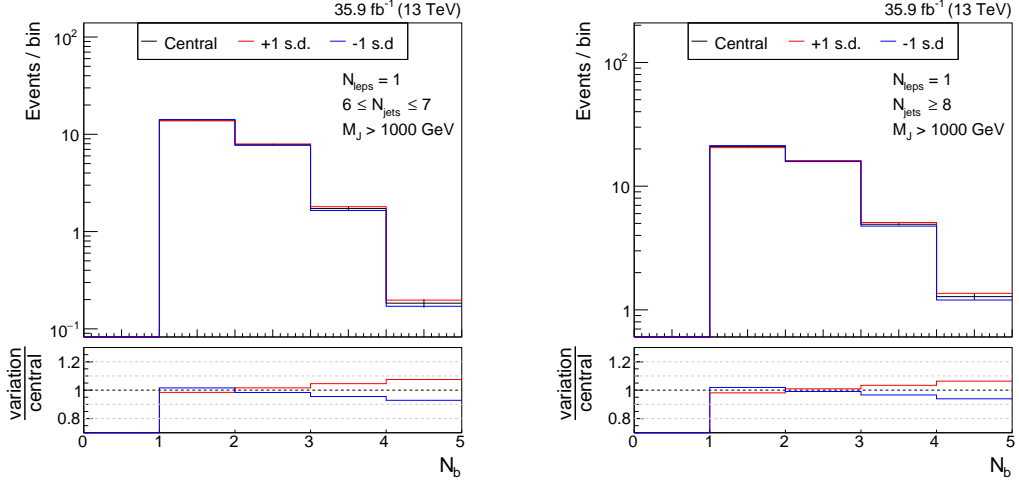


Figure 9.6: Effect of the  $\pm 1$  s.d. correlated variations of the b-flavor and c-flavor jet data-to-simulation scale factors on the  $N_b$  distribution in  $t\bar{t}$  for the two most sensitive bins: ( $N_{\text{jets}} \geq 8$ ,  $800 < M_J \leq 1000 \text{ GeV}$ ) (left) and ( $N_{\text{jets}} \geq 8$ ,  $M_J > 1000 \text{ GeV}$ ) (right). Event yields are normalized to that expected in  $35.9 \text{ fb}^{-1}$  of data.

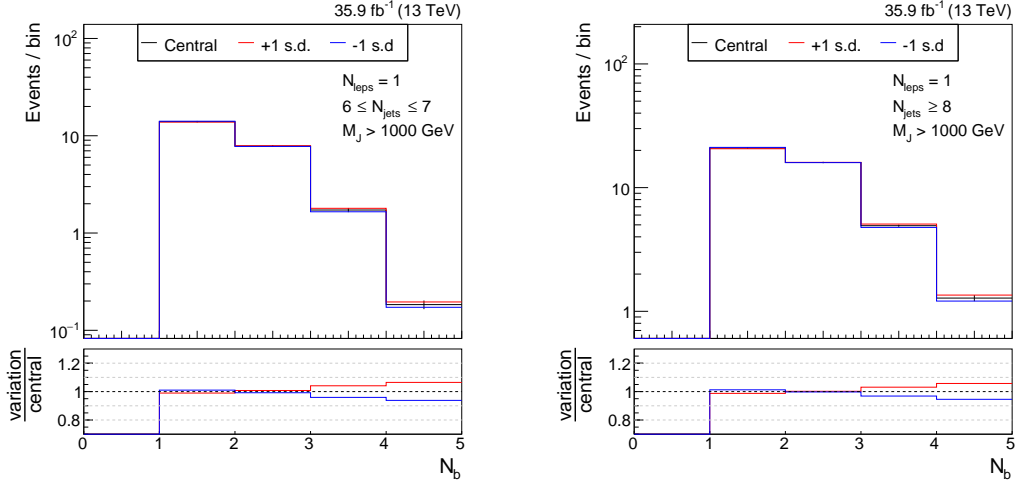


Figure 9.7: Effect of the  $\pm 1$  s.d. variations of the light-flavor jet data-to-simulation scale factors on the  $N_b$  distribution in  $t\bar{t}$  for the two most sensitive bins: ( $N_{\text{jets}} \geq 8$ ,  $800 < M_J \leq 1000 \text{ GeV}$ ) (left) and ( $N_{\text{jets}} \geq 8$ ,  $M_J > 1000 \text{ GeV}$ ) (right). Event yields are normalized to that expected in  $35.9 \text{ fb}^{-1}$  of data.

varied independently. The effect of these variations on the  $N_b$  distribution in  $t\bar{t}$  events is shown in Figure 9.6 and Figure 9.7.

### 9.3 Lepton Fake Rate in QCD

While the QCD normalization is measured from data, it is mostly constrained by the  $N_{\text{leps}} = 0$  selection and applied in a  $N_{\text{leps}} = 1$  region. If the simulated  $N_{\text{leps}}$  distribution is not modelled perfectly, there may be residual differences between the normalizations of these two regions. For processes that have true prompt leptons, such as  $t\bar{t}$  and  $W + \text{jets}$ , the  $N_{\text{leps}}$  distribution is well modelled, because the dominant effects are the  $W$  branching fractions and the acceptance (including selection efficiency), both of which are well understood. For QCD, however, this is less well modelled as the simulation of the tail of the jet fragmentation function as well as detector effects that can produce fake leptons are not as well understood.

To assign a systematic uncertainty on the modelling of the ratio of 0-lepton to 1-lepton events in QCD, the lepton isolation distributions are studied. Figure 9.8 shows the relative isolation distributions for electrons (left) and muons (right) in a data sample corresponding to the control regions. The binning of the histograms are chosen such that the first bin corresponds to the relative isolation requirement for signal leptons (0.1 for electrons and 0.2 for muons). The normalizations of the QCD,  $t\bar{t}$ , and  $W + \text{jets}$  processes are scaled to match the results of a control region fit described in Section 10.2.

Table 9.2 shows the ratio of  $I^{\text{rel}} < 0.1(0.2)$  to  $I^{\text{rel}} \geq 0.1(0.2)$  for electrons(muons) in QCD and data with contributions for all other processes ( $t\bar{t}$ ,  $W + \text{jets}$ , Other) subtracted. As the ratio in data agrees to that in QCD simulation within 20%, an additional 20% log-normal uncertainty is assigned to the QCD normalization in 1-lepton bins.

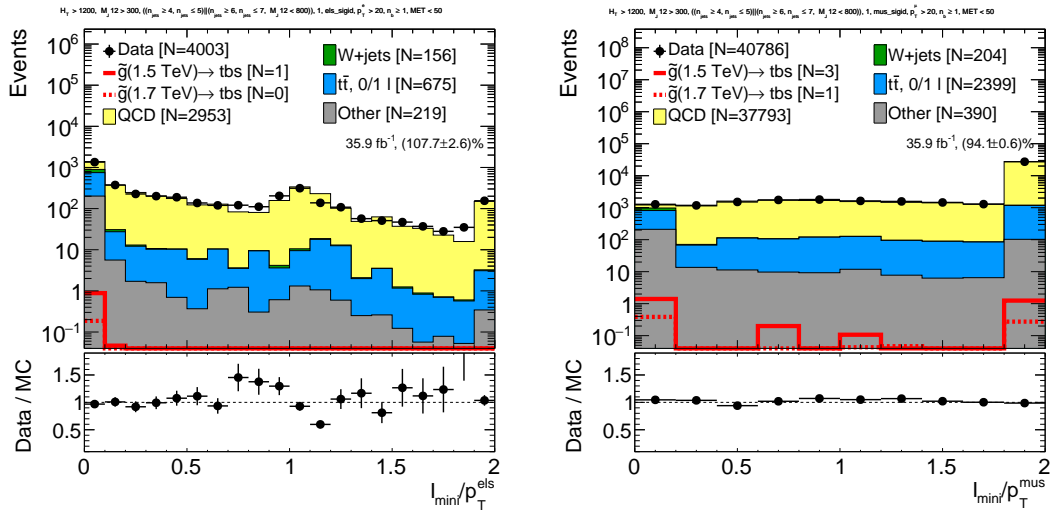


Figure 9.8: The relative isolation distribution for electrons (left) and muons (right) in the control region bins. The binning of the histograms are chosen such that the first bin corresponds to the relative isolation requirement for signal leptons (0.1 for electrons and 0.2 for muons). The normalizations of the QCD,  $t\bar{t}$ , and  $W + \text{jets}$  processes are scaled to match the results of a control region fit described in Section 10.2.

Process	Electrons			Muons		
	$I^{\text{rel}} < 0.1$	$I^{\text{rel}} \geq 0.1$	ratio	$I^{\text{rel}} < 0.2$	$I^{\text{rel}} \geq 0.2$	ratio
QCD	496.8	2455.5	0.20	219.8	36553.3	0.0060
Data - all other	452.8	2500.5	0.18	275.4	37497.7	0.0073

Table 9.2: Comparison of the relative isolation distributions, as described in the caption of Figure 9.8, for electrons and muons between QCD and data with contributions from “all other” ( $t\bar{t}$ ,  $W + \text{jets}$ , and Other) subtracted.

## 9.4 Additional systematic uncertainties

Other experimental uncertainties are small and include lepton selection efficiency, jet energy scale, jet energy resolution, and integrated luminosity. The uncertainty associated with lepton selection efficiency is determined by varying the efficiency to select a lepton within its uncertainty determined from data. Jet energy scale uncertainties [101, 102] are assessed by varying the  $p_T$  of small- $R$  jets as a function of  $p_T$  and  $\eta$ . The uncertainty arising from jet energy resolution [101, 102] is determined by applying an  $|\eta|$ -dependent

factor to the jet  $p_T$  to match the jet energy resolution observed in data. The integrated luminosity is varied according to its uncertainty of 2.5% [103], affecting only the backgrounds estimated from simulation. No uncertainty is applied for the amount of pileup as studies have shown its effect to be negligible in this high- $H_T$  selection. The uncertainties due to the limited size of simulation samples are incorporated as uncorrelated nuisance parameters in the fit.

Theoretical systematic uncertainties are applied and include independent and correlated variations of the renormalization and factorization scales. Additionally, uncertainties on the PDF are incorporated by considering variations in the NNPDF 3.0 scheme [87]. The size of these uncertainties is typically small as the effect of these variations is largely to modify the cross section of processes, which for the main backgrounds are constrained by data.

The background systematic uncertainties that affect the  $N_b$  shape are shown in Figure 9.9 for the two most sensitive search bin.

#### 9.4.1 $N_b$ distribution with NLO Precision

As the nominal  $N_b$  distribution shape is generated at LO precision, it is important to verify that the size of NLO effects is small and covered the experimental uncertainties. To do this, the  $N_b$  distributions of  $t\bar{t}$  samples generated at LO precision with the default MADGRAPH5\_aMC@NLO 2.2.2 and generated at NLO precision with POWHEG 2.0 are compared after the baseline selection. In order to evaluate only the shape differences between the two samples, the normalization of the MADGRAPH5\_aMC@NLO sample is scaled to match that of the POWHEG sample. The comparison of the two distributions, shown in Figure 9.10, is conducted in bins of  $N_{\text{jets}}$  and indicates a disagreement of about 5%.

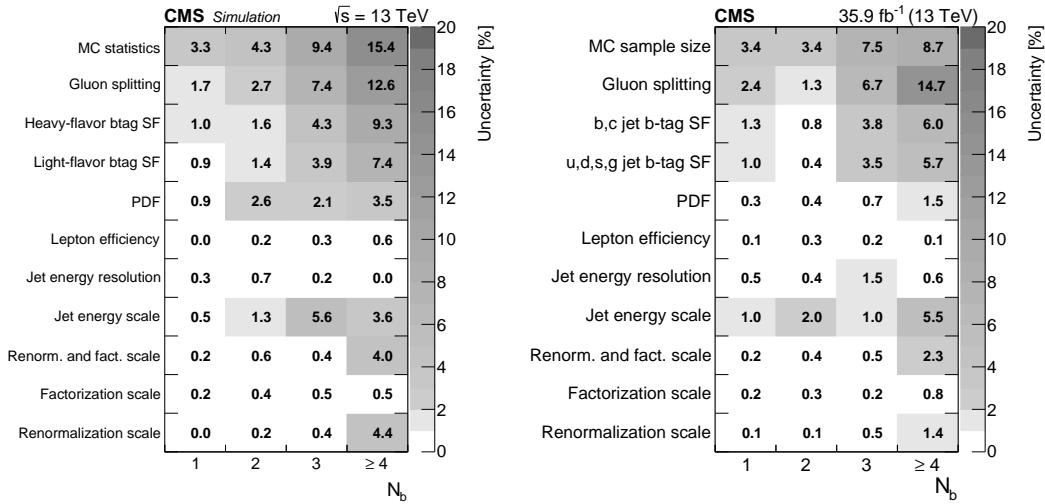


Figure 9.9: Background systematic uncertainties affecting the  $N_b$  shape (in percent) for the ( $N_{\text{jets}} \geq 8$ ,  $500 < M_J \leq 1000 \text{ GeV}$ ) (left) and ( $N_{\text{jets}} \geq 8$ ,  $M_J > 1000 \text{ GeV}$ ) (right) bins. The bottom row shows the total uncertainty for a given  $N_b$  bin by summing in quadrature all uncertainties. These values are similar for other ( $N_{\text{jets}}$ ,  $M_J$ ) bins.

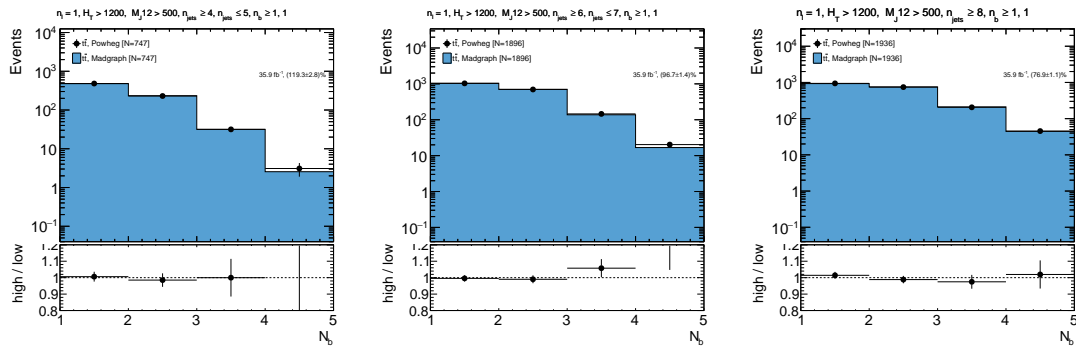


Figure 9.10: Comparison of the  $N_b$  distribution for a sample generated at LO precision with MADGRAPH5\_aMC@NLO 2.2.2 (blue histogram) with that of one generated at NLO precision with POWHEG 2.0 (data points). The comparison is done after the baseline selection and in bins of  $4 \leq N_{\text{jets}} \leq 5$  (left),  $6 \leq N_{\text{jets}} \leq 7$  (middle), and  $N_{\text{jets}} \geq 8$  (right). In order to evaluate only shape differences, the MADGRAPH5\_aMC@NLO sample is normalized to match the normalization of the POWHEG sample.

$N_{PV}^{true} \leq 20$	$20 < N_{PV}^{true} \leq 40$	$N_{PV}^{true} > 40$
$8.0 \pm 0.5\%$	$8.1 \pm 0.4\%$	$7.5 \pm 1.5\%$

Table 9.3: The signal efficiency of the most sensitive bin ( $N_{\text{jets}} \geq 8, M_J > 1000$  GeV) for a 1600 GeV gluino in various bins of the number of truth-level primary vertices.

Given the level of agreement between the two samples, the `MADGRAPH5_aMC@NLO` sample is used in this analysis as the sample size is significantly larger than that for the `POWHEG` sample.

## 9.5 Signal Systematics

Several of the systematic uncertainties affecting the signal yield are evaluated in the same way as the background yield. These are the uncertainties due to gluon splitting, lepton selection efficiency, jet energy scale, jet energy resolution, b tagging scale factors, simulation sample size, integrated luminosity, and theoretical uncertainties. All systematic variations affect both the  $N_b$  shape and normalization, except for the gluon splitting uncertainty, which is taken to affect only the  $N_b$  shape.

The number of jets from ISR produced in the signal simulation is reweighted based on comparisons between data and simulated  $t\bar{t}$  samples. The reweighting factors vary between 0.92 and 0.51 for the number of ISR jets between 1 and  $\geq 6$ . One half of the deviation from unity is taken as the systematic uncertainty in these reweighting factors.

The systematic uncertainties affecting the signal  $N_b$  shape are shown in Fig. 9.11 (right) for the most sensitive bin in a model with  $m_{\tilde{g}} = 1600$  GeV. The dominant signal systematic uncertainties arise from the limited simulation sample size, the b tagging efficiency scale factors, and the ISR modeling. There is no systematic uncertainty taken for pileup reweighting, as the signal efficiency is found to be insensitive to the number of pileup interactions, which is shown in Table 9.3.

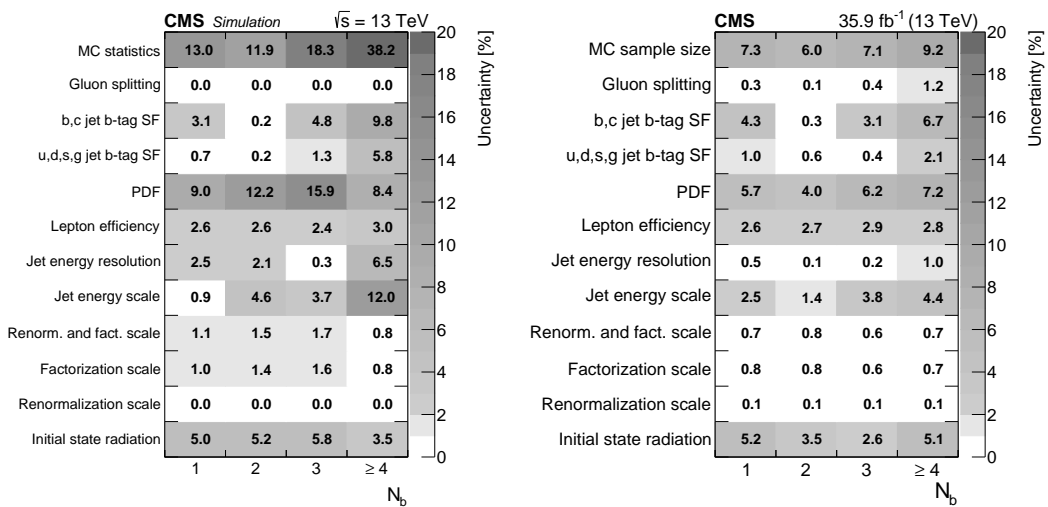


Figure 9.11: Signal systematic uncertainties affecting the  $N_b$  shape (in percent) for the ( $N_{\text{jets}} \geq 8$ ,  $500 < M_J \leq 1000 \text{ GeV}$ ) (left) and ( $N_{\text{jets}} \geq 8$ ,  $M_J > 1000 \text{ GeV}$ ) (right) bins. The bottom row shows the total uncertainty for a given  $N_b$  bin by summing in quadrature all uncertainties. These values are similar for other ( $N_{\text{jets}}$ ,  $M_J$ ) bins.

# Chapter 10

## Fit Validation

Due to the fit's complexity and many adjustable parameters, it is important to verify the fit model and that it behaves as intended.

### 10.1 Signal Injection Study

Signal injection studies are a useful way to quantify how well the maximum-likelihood fit can extract a potential signal if it is indeed present. These studies rely on the use of psuedodata experiments. A single experiment consists of generating psuedodata by fluctuating bin yields around their pre-fit values according to their statistical and systematic uncertainties. This pseudodata can then be treated as observations and can be fit with the results examined. As many psuedodata experiments are generated, the collection of observations approximates the distribution of possible observations as defined by the fit model and correspondingly the distribution of post-fit results approximates the distribution of possible post-fit results.

For the signal injection study, 1000 experiments are generated by fluctuating both the expected background and signal yields (with signal strength = 1) for each gluino mass point. Figure 10.1 shows the median fitted signal strength of the 1000 experiments for each gluino mass point. For gluino masses between 1000 – 1700 GeV the fit shows

$m_{\tilde{g}} = 1800 \text{ GeV}$	$m_{\tilde{g}} = 1900 \text{ GeV}$	$m_{\tilde{g}} = 2000 \text{ GeV}$
96%	95%	96%

Table 10.1: Actual coverage probability of the 95% confidence interval of the fit for the mass points with a biased signal extraction.

no evidence of a bias and has a median extracted signal strength of  $\sim 1$ , while for higher gluino masses, the fit tends to under-extract the signal contribution (up to  $\sim 25\%$  for  $m_{\tilde{g}} = 2000 \text{ GeV}$ ). These biased mass points correspond to models where the number of signal events is very low. For example, there are only 8.6 events expected for the  $m_{\tilde{g}} = 2000 \text{ GeV}$  model, summing over all analysis bins. This low yield means that gaussian-approximations of the poisson-distributed bin yields used in the fit model are inaccurate, leading to the bias in the fit.

In order to test this hypothesis, additional signal injection studies, each consisting of 1000 experiments, are performed for the  $m_{\tilde{g}} = 2000 \text{ GeV}$  mass point, where the injected signal strengths are 1x, 3x, 5x, 10x the nominal cross-section. The resulting median extracted signal is 78%, 92%, 95%, and 98% the injected signal, respectively. These results support the hypothesis, as, with increasing signal strength, the gaussian-approximations become increasingly accurate, allowing for the fit to properly extract the signal contributions. The distributions of fitted signal strengths for these tests are shown in Figure 10.2.

No modifications to the fit model are made to correct for this issue. This is because the fit bias only affects mass points that are far above the highest mass (1650 GeV) expected to be excluded by this analysis, and Figure 10.1 shows that the fit bias is much smaller than the precision of the fit for those mass points. Additionally, the coverage of the 95% confidence intervals of the fit is tested using the signal injection experiments and found to be either correct or slightly conservative, as shown in Table 10.1.

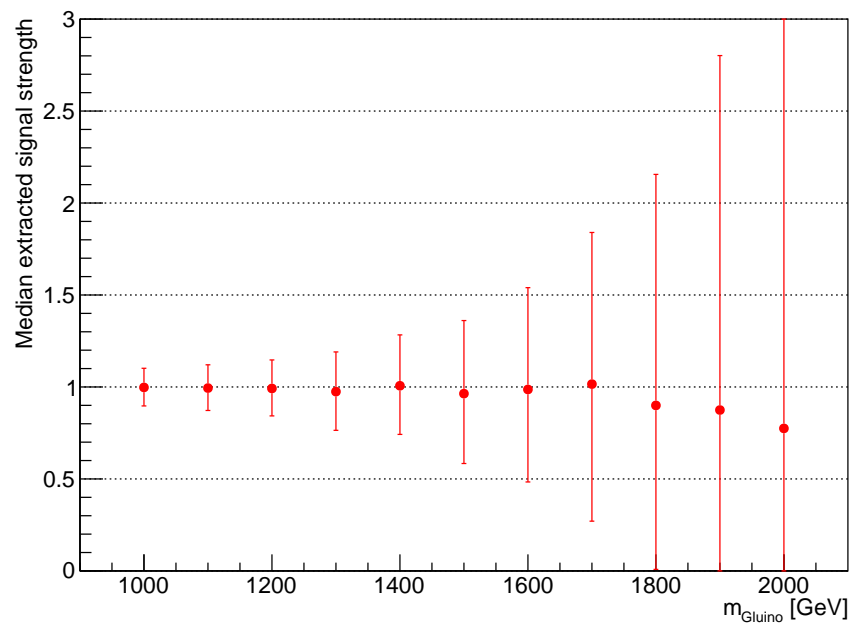


Figure 10.1: Median extracted signal strength of 1,000 psuedodata experiments as a function of gluino mass. The uncertainties drawn are the median upper and lower errors of the fitted signal strengths per mass point.

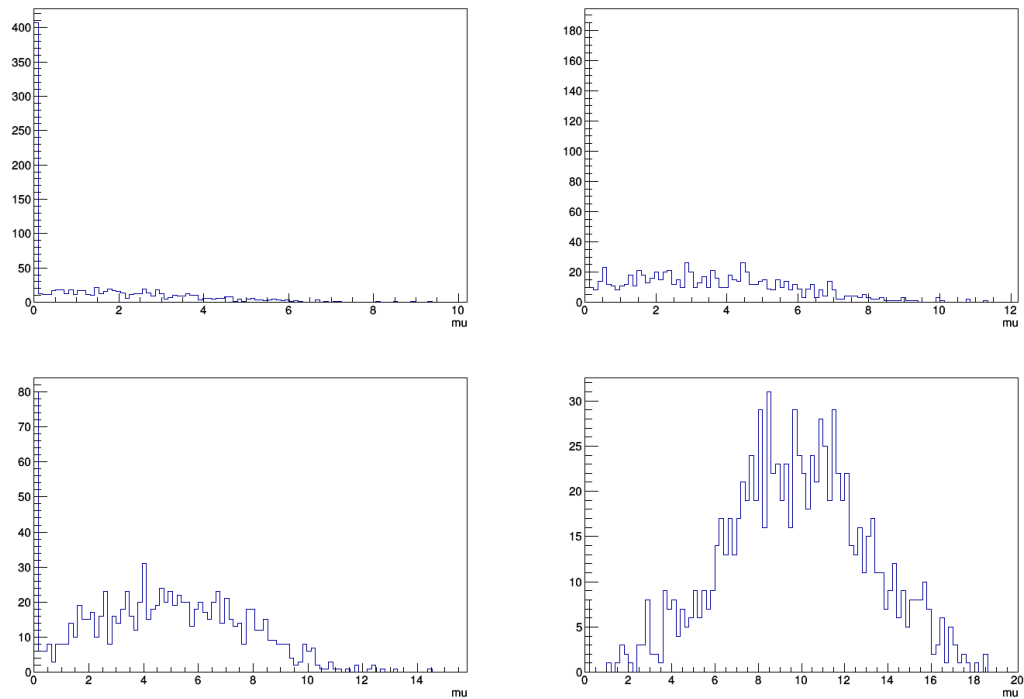


Figure 10.2: Distribution of fitted signal strengths of 1000 pseudodata experiments for a 2000 GeV gluino at 1x (top-left), 3x (top-right), 5x (bottom-left), and 10x (bottom-right) the nominal cross-section. The amount of signal extracted is 78%, 92%, 95%, and 98% the injected signal, respectively.

## 10.2 Control Region Fit

While the signal injection studies are a useful validation of the fit model, it is important to validate the model using data in order to test for unmodeled effects. This is done by performing the maximum-likelihood fit with only the low- $N_{\text{jets}}$ , low- $M_{\text{J}}$  control regions, as defined in Table 7.5. These bins are chosen due to their low-expected signal yields, which avoids signal contamination effects and unblinding the high-expected signal regions in the case further modifications of the fit are needed.

The control region fit, under the background-only hypothesis, is able to model the observed data well without needing large adjustments to the nuisance parameters, as seen in the post-fit  $N_b$  distributions shown in Figure 10.3. The change between the pre- and post-fit normalizations of the background processes is shown in Table 10.2, while the pulls of the nuisance parameters corresponding to systematic uncertainties (largely controlling the shape of the  $N_b$  distribution) are shown in Figure 10.4. Both sets of values are well-behaved, as the largest change in normalization is less than 50%, with typical values around 10-15%, while the nuisance parameters are all consistent with their pre-fit uncertainties, with most shifted less than 0.05 s.d. The largest pulls correspond to nuisance parameters controlling the gluon splitting rate ( $g_s$ , +0.42 s.d.), the light-flavor b-tag SFs ( $\text{btag\_udsg}$ , +0.37 s.d.), and the heavy-flavor b-tag SFs ( $\text{btag\_bc}$ , +0.13 s.d.). These nuisances are expected to be shifted up as the observed data is higher than simulation in the tail of the pre-fit  $N_b$  distributions, as seen in Figure ??, where the background simulation is normalized to match the observed data yields with a single scaling factor and with the pre-fit uncertainty represented by a hatched band.

Lastly, Table 10.3 compares the post-fit pulls of the background-only and signal-plus-background control region fit. The post-fit pulls between the two fits are fully consistent with each other, as is expected for these signal-poor regions.

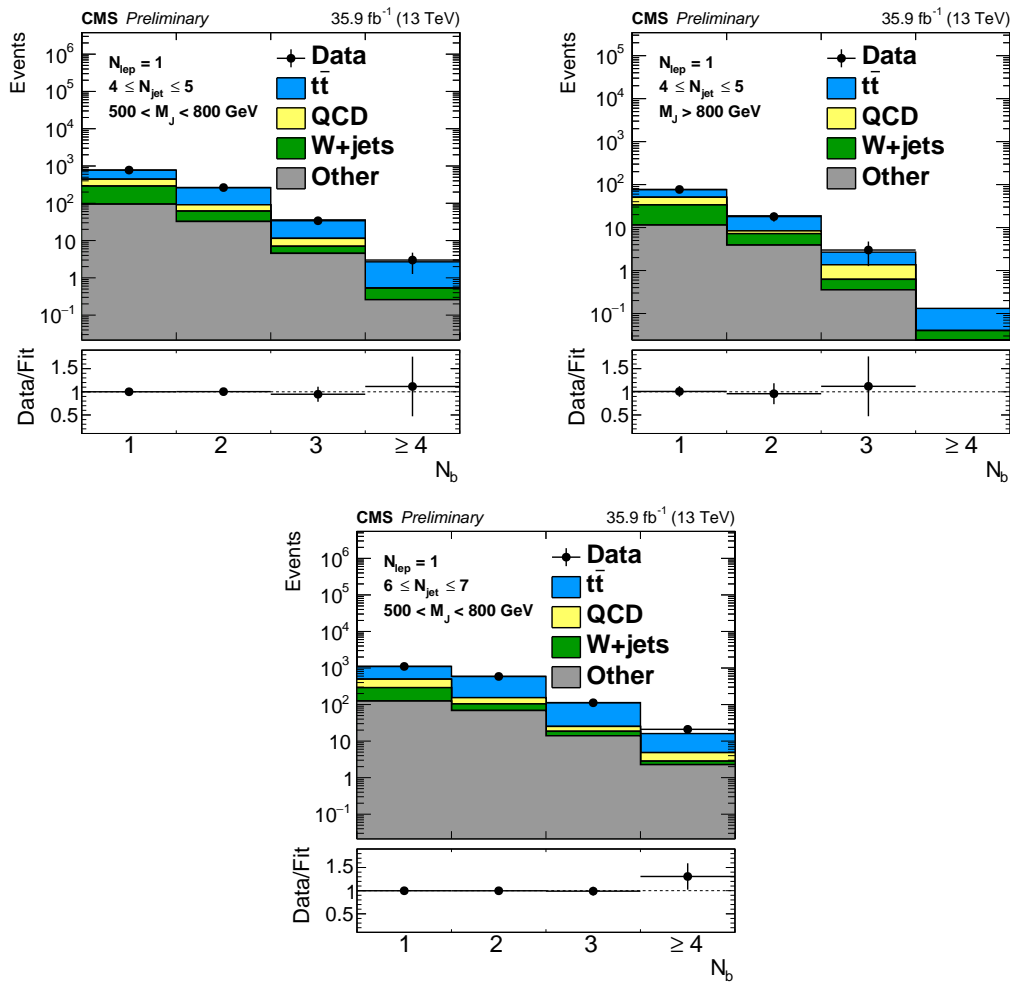


Figure 10.3: Post-fit  $N_b$  distributions of the control region fit.

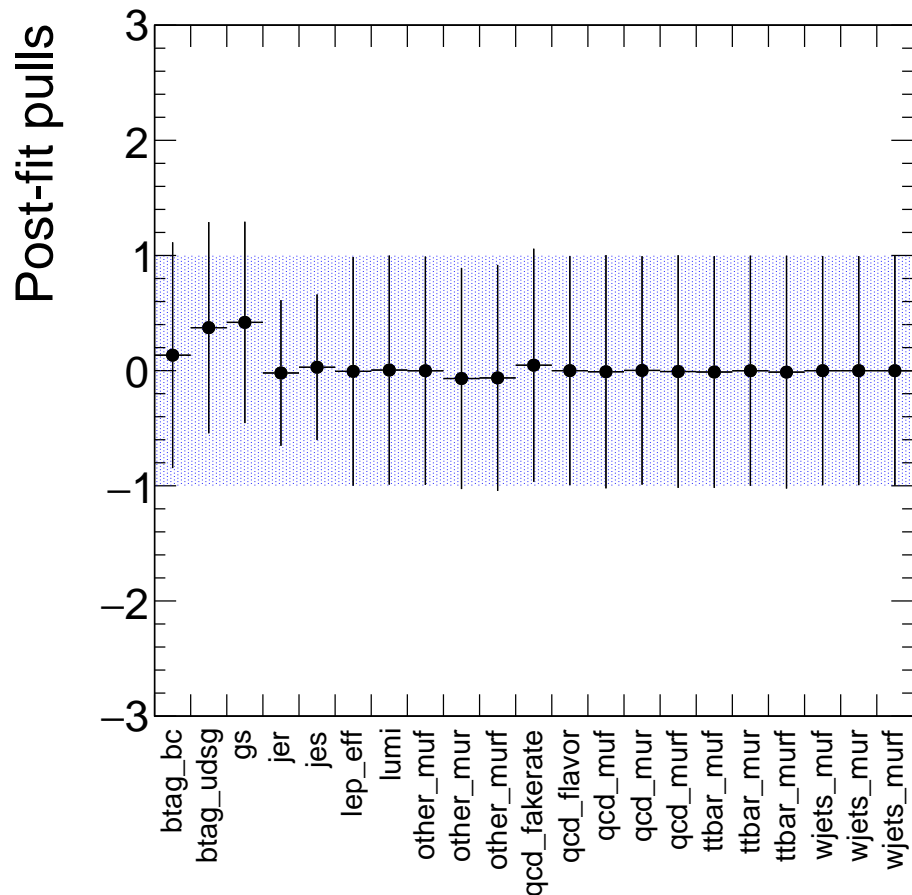


Figure 10.4: Post-fit pulls of the background-only control region fit. The post-fit value of the nuisance parameter is indicated by the data point, while the post-fit uncertainty is shown as a black line and is normalized by the pre-fit uncertainty depicted as the blue band.

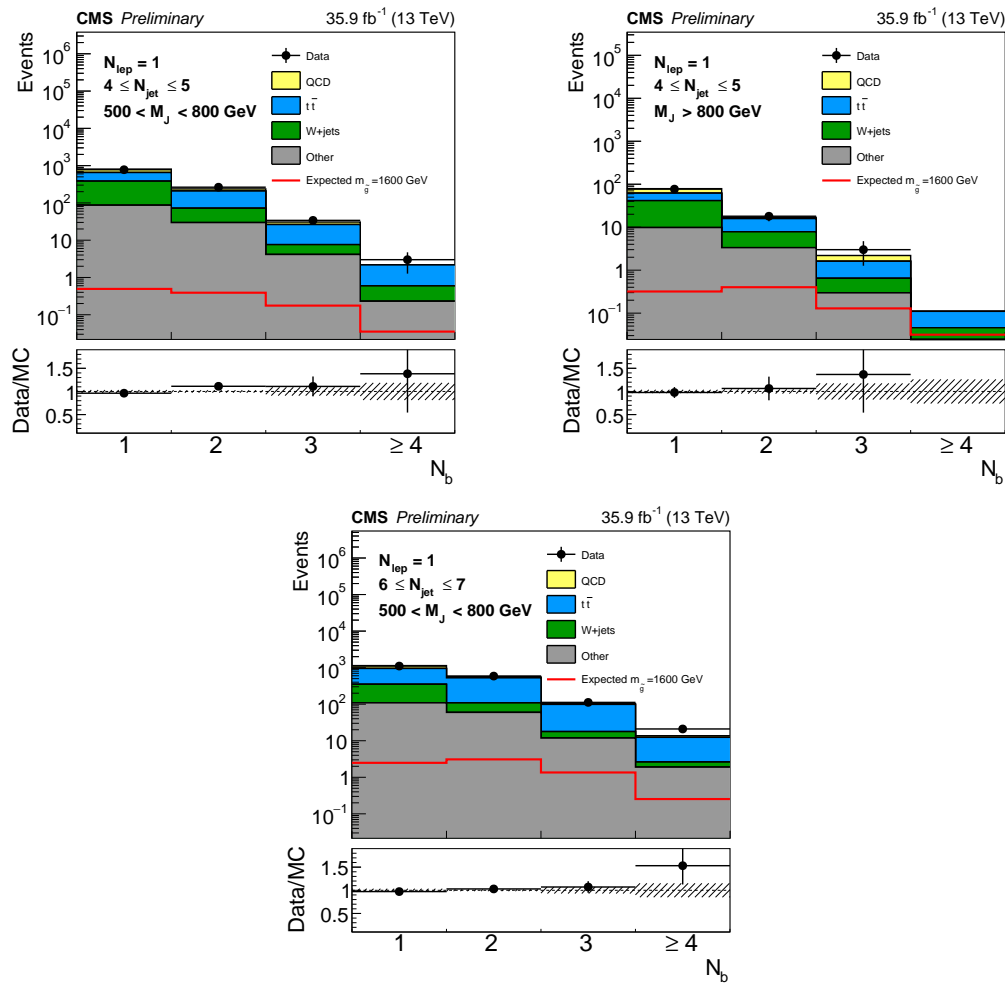


Figure 10.5: Pre-fit  $N_b$  distributions of the control region bins with the background simulation normalized to the observed data yields with a single scaling factor. The ratio of data-to-simulation is shown in the lower panel. The pre-fit uncertainty is represented by the hatched band.

Process	Pre-fit Yield	Post-fit Yield (b-only fit)	% change
$4 \leq N_{\text{jets}} \leq 5, 500 \leq M_J \leq 800$			
t̄t	501.4	$533.3 \pm 80.7$	+6.3
QCD	218.8	$186.7 \pm 36.8$	-14.7
W + jets	400.4	$225.5 \pm 100.0$	-43.7
Other	141.4	$131.8 \pm 34.5$	-6.8
$4 \leq N_{\text{jets}} \leq 5, M_J \geq 800$			
t̄t	36.9	$37.5 \pm 13.3$	+1.6
QCD	23.1	$18.9 \pm 4.5$	-18.2
W + jets	45.7	$25.7 \pm 11.4$	-43.8
Other	16.8	$15.7 \pm 3.8$	-6.5
$6 \leq N_{\text{jets}} \leq 7, 500 \leq M_J \leq 800$			
t̄t	1370.4	$1148.3 \pm 78.0$	-16.2
QCD	293.9	$262.6 \pm 52.1$	-10.6
W + jets	367.7	$205.6 \pm 92.2$	-44.1
Other	225.2	$209.7 \pm 58.5$	-6.9

Table 10.2: Table comparing the post-fit normalizations of the control region fit to the pre-fit yields for the various background processes.

Nuisance parameter	Post-fit pull ( $b$ -only fit)	Post-fit pull ( $s + b$ fit)	$\rho(\theta_i, \mu)$
b,c jet b-tag SF (btags_bc)	+0.13 ± 0.98	+0.07 ± 1.05	-0.18
u,d,s,g jet b-tag SF (btags_udsg)	+0.37 ± 0.92	+0.28 ± 0.95	-0.26
Gluon splitting (gs)	+0.42 ± 0.87	+0.22 ± 1.12	-0.43
Jet energy resolution (jer)	-0.02 ± 0.63	-0.02 ± 0.60	-0.01
Jet energy scale (jes)	+0.03 ± 0.63	+0.03 ± 0.61	-0.03
Lepton efficiency (lep_eff)	-0.01 ± 0.99	-0.01 ± 0.99	+0.01
Luminosity (lumi)	+0.00 ± 0.99	+0.00 ± 0.99	-0.01
Fact. scale for other (other_muf)	-0.00 ± 0.99	-0.00 ± 0.99	+0.00
Renorm. scale for other (other_mur)	-0.07 ± 0.96	-0.06 ± 1.02	+0.02
Renorm. and Fact. scale for other (other_murf)	-0.06 ± 0.98	-0.08 ± 0.96	+0.01
QCD fake rate (qcd_fakerate)	+0.05 ± 1.01	+0.09 ± 1.14	+0.09
Fact. scale for QCD (qcd_muf)	-0.01 ± 1.01	-0.01 ± 1.01	-0.00
Renorm. scale for QCD (qcd_mur)	+0.00 ± 0.99	+0.00 ± 0.99	-0.00
Renorm. and Fact. scale for QCD (qcd_murf)	-0.01 ± 1.01	-0.01 ± 1.01	-0.00
Fact. scale for $t\bar{t}$ (ttbar_muf)	-0.01 ± 1.01	-0.01 ± 1.00	+0.00
Renorm. scale for $t\bar{t}$ (ttbar_mur)	-0.00 ± 1.00	+0.00 ± 0.99	+0.01
Renorm. and Fact. scale for $t\bar{t}$ (ttbar_murf)	-0.01 ± 1.01	-0.01 ± 1.00	+0.01
Fact. scale for W + jets (wjets_muf)	-0.00 ± 0.99	+0.00 ± 0.99	+0.00
Renorm. scale for W + jets (wjets_mur)	-0.00 ± 0.99	-0.00 ± 0.99	-0.00
Renorm. and Fact. scale for W + jets (wjets_murf)	-0.00 ± 1.00	-0.00 ± 1.00	+0.00

Table 10.3: Table of post-fit pulls of the background-only and signal-plus-background control region fit. The last column,  $\rho(\theta_i, \mu)$ , lists the correlation between the corresponding nuisance parameter,  $\theta_i$ , and the nuisance parameter controlling the signal strength,  $\mu$ .

# Chapter 11

## Results and Interpretation

### 11.1 Results

The results of a background-only fit of the observed  $N_b$  distributions are shown in Figures 11.1 and 11.2. These figures separately show the  $N_{\text{leps}} = 1$  control and signal regions, although the fit includes all bins simultaneously. The  $N_b$  distributions in data are well described by the fit, and examination of the nuisance parameters shows that none of them are significantly changed by the fit. The post-fit yields are presented in Table 11.1.

A signal-plus-background fit is performed for gluino masses ranging from 1000 to 2000 GeV. For all masses, the post-fit  $N_b$  distribution describes the data well, and the fit extracts at most a small and insignificant signal contribution. For example, with a 1600 GeV gluino, the extracted signal yield relative to the model prediction is  $r = 0.18^{+0.41}_{-0.18}$ . The change of nuisance parameters by the fit is small and consistent with those of the background-only fit.

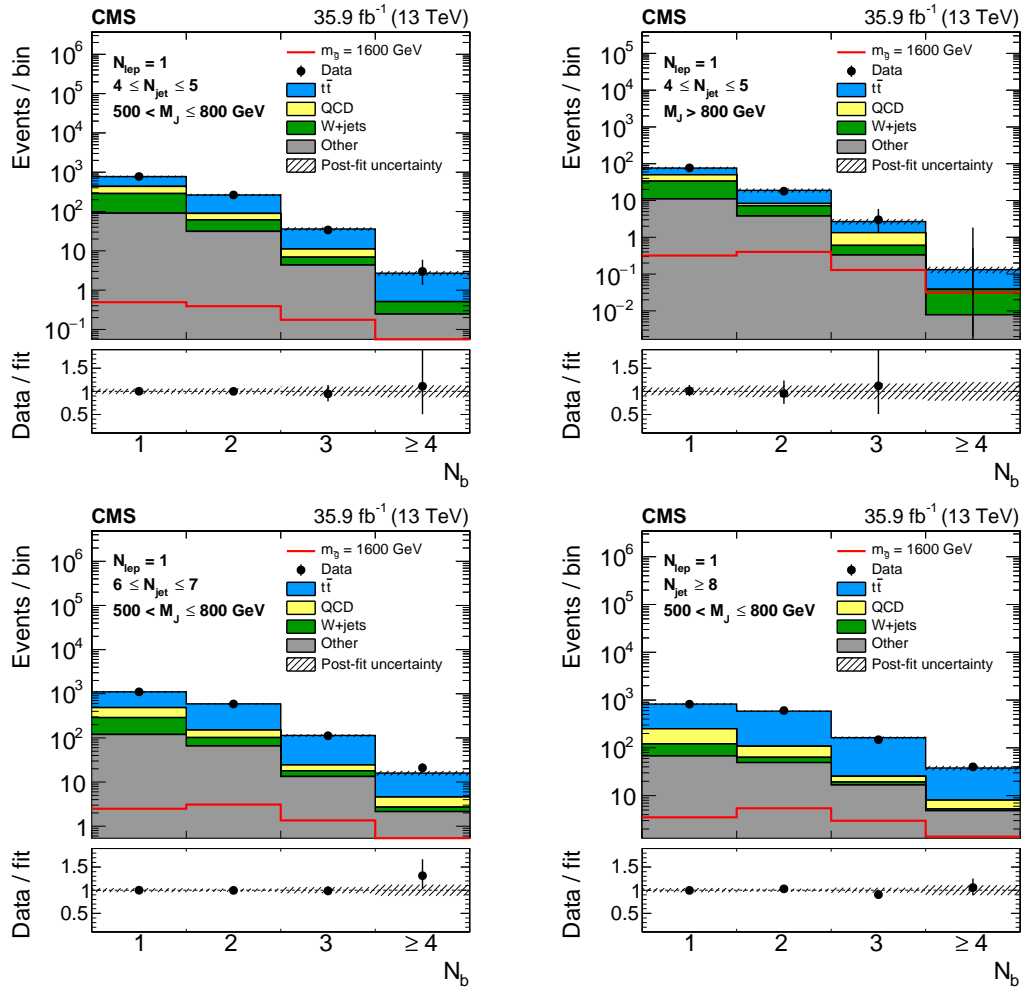


Figure 11.1: Data and the background-only post-fit  $N_b$  distribution for bins with low expected signal contribution:  $4 \leq N_{\text{jets}} \leq 5$ ,  $500 < M_J \leq 800 \text{ GeV}$  (upper-left),  $4 \leq N_{\text{jets}} \leq 5$ ,  $M_J > 800 \text{ GeV}$  (upper-right),  $6 \leq N_{\text{jets}} \leq 7$ ,  $500 < M_J \leq 800 \text{ GeV}$  (lower-left), and  $N_{\text{jets}} \geq 8$ ,  $500 < M_J \leq 800 \text{ GeV}$  (lower-right). The expected signal distribution is also shown for a gluino mass of 1600 GeV. The ratio of data to post-fit yields is shown in the lower panel. The post-fit uncertainty is depicted as a hatched band.

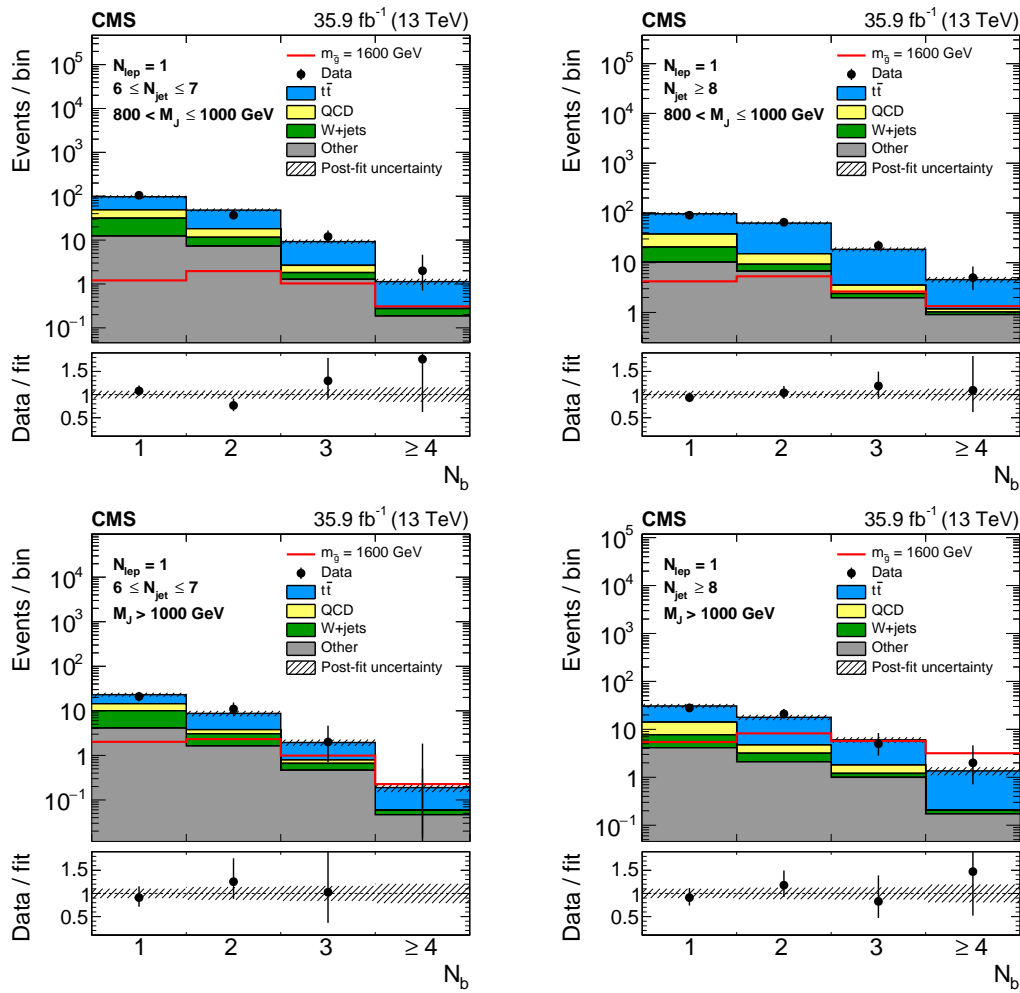


Figure 11.2: Data and the background-only post-fit  $N_b$  distribution for bins with large expected signal contribution:  $6 \leq N_{\text{jets}} \leq 7$ ,  $800 < M_J \leq 1000 \text{ GeV}$  (upper-left),  $N_{\text{jets}} \geq 8$ ,  $800 < M_J \leq 1000 \text{ GeV}$  (upper-right),  $6 \leq N_{\text{jets}} \leq 7$ ,  $M_J > 1000 \text{ GeV}$  (lower-left), and  $N_{\text{jets}} \geq 8$ ,  $M_J > 1000 \text{ GeV}$  (lower-right). The expected signal distribution is also shown for a gluino mass of 1600 GeV. The ratio of data to post-fit yields is shown in the lower panel. The post-fit uncertainty is depicted as a hatched band.

$N_b$	QCD	$t\bar{t}$	W + jets	Other	All bkg.	Data	Expected $m_{\tilde{g}} = 1600$ GeV
$4 \leq N_{\text{jets}} \leq 5, 500 < M_J \leq 800$ GeV							
1	148	340	196	91	$775 \pm 43$	777	$0.50 \pm 0.13$
2	29	175	30	31	$264 \pm 17$	264	$0.39 \pm 0.11$
3	4.3	24.8	2.5	4.4	$36 \pm 4$	34	$0.18 \pm 0.08$
$\geq 4$	0.0	2.2	0.3	0.2	$2.7 \pm 0.4$	3	$0.04 \pm 0.04$
$4 \leq N_{\text{jets}} \leq 5, M_J > 800$ GeV							
1	16.5	26.3	22.5	11.0	$76 \pm 6$	77	$0.32 \pm 0.11$
2	1.1	10.6	3.4	3.8	$19 \pm 2$	18	$0.40 \pm 0.12$
3	0.7	1.3	0.3	0.3	$2.7 \pm 0.5$	3	$0.13 \pm 0.06$
$\geq 4$	0.00	0.09	0.03	0.01	$0.13 \pm 0.03$	0	$0.03 \pm 0.03$
$6 \leq N_{\text{jets}} \leq 7, 500 < M_J \leq 800$ GeV							
1	197	620	169	120	$1106 \pm 48$	1105	$2.5 \pm 0.3$
2	49	440	36	66	$591 \pm 21$	588	$3.1 \pm 0.3$
3	6.4	89.2	4.6	13.4	$114 \pm 8$	112	$1.4 \pm 0.2$
$\geq 4$	1.9	11.4	0.6	2.1	$16 \pm 2$	21	$0.25 \pm 0.09$
$N_{\text{jets}} \geq 8, 500 < M_J \leq 800$ GeV							
1	130	574	53	68	$825 \pm 38$	821	$3.5 \pm 0.3$
2	45	478	14	49	$586 \pm 20$	603	$5.4 \pm 0.4$
3	6.3	138.1	2.5	16.7	$164 \pm 9$	148	$3.0 \pm 0.3$
$\geq 4$	2.8	29.8	0.4	4.8	$38 \pm 4$	40	$1.4 \pm 0.2$
$6 \leq N_{\text{jets}} \leq 7, 800 < M_J \leq 1000$ GeV							
1	17.3	48.4	19.2	12.3	$97 \pm 8$	105	$1.2 \pm 0.2$
2	6.6	30.1	4.3	7.3	$48 \pm 4$	37	$2.0 \pm 0.3$
3	0.8	6.6	0.5	1.3	$9.3 \pm 1.0$	12	$1.0 \pm 0.2$
$\geq 4$	0.0	0.9	0.1	0.2	$1.1 \pm 0.2$	2	$0.31 \pm 0.09$
$N_{\text{jets}} \geq 8, 800 < M_J \leq 1000$ GeV							
1	17.0	58.7	10.3	10.2	$96 \pm 8$	90	$4.2 \pm 0.4$
2	5.8	47.5	2.5	6.8	$63 \pm 5$	65	$5.3 \pm 0.4$
3	1.1	15.0	0.4	2.0	$19 \pm 2$	22	$2.6 \pm 0.3$
$\geq 4$	0.2	3.4	0.1	0.9	$4.6 \pm 0.6$	5	$1.3 \pm 0.2$
$6 \leq N_{\text{jets}} \leq 7, M_J > 1000$ GeV							
1	4.4	8.7	6.0	4.1	$23 \pm 2$	21	$2.0 \pm 0.3$
2	0.7	5.0	1.4	1.6	$8.8 \pm 1.2$	11	$2.3 \pm 0.3$
3	0.1	1.2	0.2	0.5	$1.9 \pm 0.3$	2	$1.0 \pm 0.2$
$\geq 4$	0.00	0.13	0.01	0.05	$0.19 \pm 0.04$	0	$0.23 \pm 0.08$
$N_{\text{jets}} \geq 8, M_J > 1000$ GeV							
1	6.4	16.7	3.5	4.1	$31 \pm 3$	28	$5.4 \pm 0.4$
2	1.6	13.1	1.1	2.1	$18 \pm 2$	21	$8.2 \pm 0.5$
3	0.6	4.2	0.2	1.0	$6.0 \pm 0.8$	5	$5.7 \pm 0.4$
$\geq 4$	0.0	1.2	0.0	0.2	$1.4 \pm 0.3$	2	$3.2 \pm 0.3$

Table 11.1: Post-fit yields of the background-only fit, observed data, and expected yields for  $m_{\tilde{g}} = 1600$  GeV.

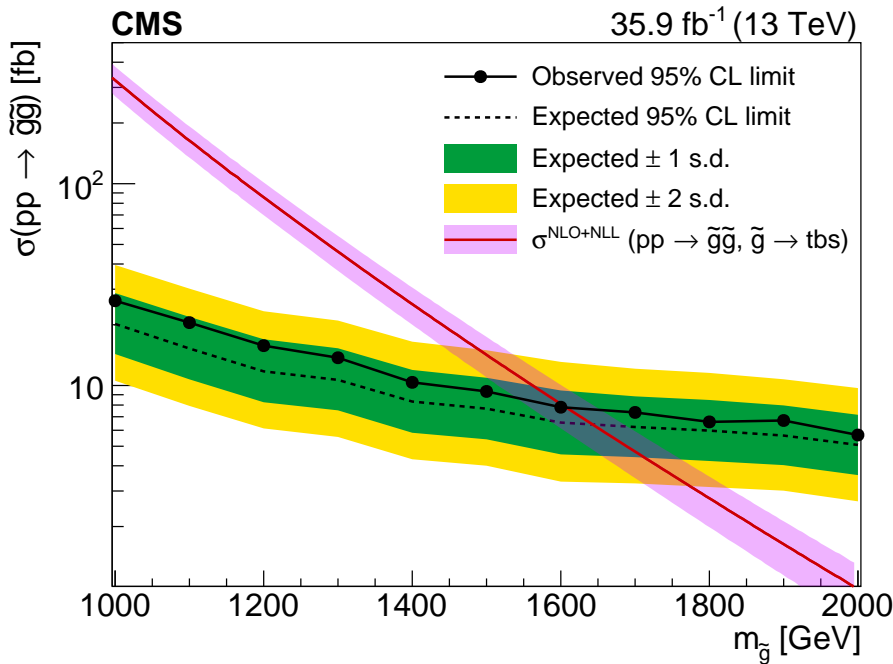


Figure 11.3: Cross section upper limits at 95% CL for a model of gluino pair production with  $\tilde{g} \rightarrow tbs$  compared to the gluino pair production cross section. The theoretical uncertainties in the cross section are shown as a band around the red line [16]. The expected limits (dashed line) and their  $\pm 1$  s.d. and  $\pm 2$  s.d. variations are shown as green and yellow bands, respectively. The observed limit is shown by the solid line with dots.

## 11.2 Interpretation and Limits

Limits on the signal production cross section are calculated at 95% confidence level (CL) using the asymptotic approximation of the  $CL_s$  criterion [104, 105, 106, 107] and shown in Figure 11.3. Comparing the observed limit to the gluino pair production cross section [16], gluino masses below 1610 GeV are excluded in the benchmark  $\tilde{g} \rightarrow tbs$  model.

# **Chapter 12**

## **Conclusions**

### **12.1 Section Title**

  Lorem ipsum dolor sit amet, consectetur adipiscing elit, sed do eiusmod tempor incididunt ut labore et dolore magna aliqua. Ut enim ad minim veniam, quis nostrud exercitation ullamco laboris nisi ut aliquip ex ea commodo consequat. Duis aute irure dolor in reprehenderit in voluptate velit esse cillum dolore eu fugiat nulla pariatur. Excepteur sint occaecat cupidatat non proident, sunt in culpa qui officia deserunt mollit anim id est laborum.

## **Part V**

## **Appendix**

# **Appendix A**

## **DeepJEC**

### **A.1 Section Title**

Appendicitis

# **Appendix B**

## **HF Timing**

### **B.1 Section Title**

Appendicitis

# Bibliography

- [1] CMS Collaboration, “Summaries of CMS cross section measurements.” <https://twiki.cern.ch/twiki/bin/view/CMSPublic/PhysicsResultsCombined>, Jan, 2018. Accessed: May 08, 2018.
- [2] CMS Collaboration, “CMS Supersymmetry Physics Results.” <https://twiki.cern.ch/twiki/bin/view/CMSPublic/PhysicsResultsSUS>, April, 2018. Accessed: May 09, 2018.
- [3] ATLAS Collaboration, “Summary plots from the ATLAS Supersymmetry physics group.” <https://atlas.web.cern.ch/Atlas/GROUPS/PHYSICS/CombinedSummaryPlots/SUSY/>, Dec, 2017. Accessed: May 09, 2018.
- [4] B. C. Allanach, *Beyond the Standard Model Lectures for the 2016 European School of High-Energy Physics*, in *Proceedings, 2016 European School of High-Energy Physics (ESHEP2016): Skeikampen, Norway, June 15-28 2016*, (2017), pp. 123–152, 2017. arXiv:1609.0201.
- [5] F. Marcastel, *CERN’s Accelerator Complex. La chaîne des accélérateurs du CERN, General Photo* (Oct, 2013).
- [6] W. J. Stirling, 13/8 TeV LHC luminosity ratios, *Private Communication* (2013).
- [7] L. R. F. Castillo, *The ATLAS and CMS detectors*, in *The Search and Discovery of the Higgs Boson*, 2053-2571, pp. 4-1 to 4-8. Morgan & Claypool Publishers, 2015.
- [8] M. Schott and M. Dunford, *Review of single vector boson production in pp collisions at  $\sqrt{s} = 7$  TeV.* , *Eur. Phys. J. C* **74** (May, 2014) 60 p.
- [9] T. Lenzi, *Development and Study of Different Muon Track Reconstruction Algorithms for the Level-1 Trigger for the CMS Muon Upgrade with GEM Detectors*, Master’s thesis, U. Brussels, 2013.
- [10] B. Isildak, *Measurement of the differential dijet production cross section in proton-proton collisions at  $\sqrt{s} = 7$  TeV*. PhD thesis, Bogazici U., 2011. arXiv:1308.6064.

- [11] CMS Collaboration, *Identification and filtering of uncharacteristic noise in the cms hadron calorimeter*, *Journal of Instrumentation* **5** (2010), no. 03 T03014.
- [12] P. Paolucci *et. al.*, *CMS Resistive Plate Chamber overview, from the present system to the upgrade phase I*, *Journal of Instrumentation* **8** (2013), no. 04 P04005.
- [13] CMS Collaboration, *The cms experiment at the cern lhc*, *Journal of Instrumentation* **3** (2008), no. 08 S08004.
- [14] CMS Collaboration, A. M. Sirunyan *et. al.*, *Identification of heavy-flavour jets with the CMS detector in pp collisions at 13 TeV*, *Submitted to: JINST* (2017) [arXiv:1712.0715].
- [15] CMS Collaboration, “Public CMS Luminosity Information.” [https://twiki.cern.ch/twiki/bin/view/CMSPublic/LumiPublicResults#2016\\_proton\\_proton\\_13\\_TeV\\_collis](https://twiki.cern.ch/twiki/bin/view/CMSPublic/LumiPublicResults#2016_proton_proton_13_TeV_collis), April, 2018. Accessed: April 23, 2018.
- [16] C. Borschensky, M. Krämer, A. Kulesza, M. Mangano, S. Padhi, T. Plehn, and X. Portell, *Squark and gluino production cross sections in pp collisions at  $\sqrt{s} = 13, 14, 33$ , and 100TeV*, *Eur. Phys. J. C* **74** (2014) 3174, [arXiv:1407.5066].
- [17] T. Aoyama, M. Hayakawa, T. Kinoshita, and M. Nio, *Tenth-order qed contribution to the electron g–2 and an improved value of the fine structure constant*, *Phys. Rev. Lett.* **109** (Sep, 2012) 111807.
- [18] D. Hanneke, S. Fogwell, and G. Gabrielse, *New measurement of the electron magnetic moment and the fine structure constant*, *Phys. Rev. Lett.* **100** (Mar, 2008) 120801.
- [19] D. Hanneke, S. Fogwell Hoogerheide, and G. Gabrielse, *Cavity control of a single-electron quantum cyclotron: Measuring the electron magnetic moment*, *Phys. Rev. A* **83** (May, 2011) 052122.
- [20] C. Csaki, Y. Grossman, and B. Heidenreich, *MFV SUSY: A Natural Theory for R-Parity Violation*, *Phys. Rev.* **D85** (2012) 095009, [arXiv:1111.1239].
- [21] G. Bertone, D. Hooper, and J. Silk, *Particle dark matter: Evidence, candidates and constraints*, *Phys. Rept.* **405** (2005) 279–390, [hep-ph/0404175].
- [22] V. C. Rubin and W. K. Ford, Jr., *Rotation of the Andromeda Nebula from a Spectroscopic Survey of Emission Regions*, *Astrophys. J.* **159** (1970) 379–403.
- [23] ATLAS Collaboration, G. Aad *et. al.*, *Observation of a new particle in the search for the Standard Model Higgs boson with the ATLAS detector at the LHC*, *Phys. Lett.* **B716** (2012) 1–29, [arXiv:1207.7214].

- [24] CMS Collaboration, S. Chatrchyan *et. al.*, *Observation of a new boson at a mass of 125 GeV with the CMS experiment at the LHC*, *Phys. Lett. B* **716** (2012) 30–61, [arXiv:1207.7235].
- [25] CMS Collaboration, S. Chatrchyan *et. al.*, *Observation of a new boson with mass near 125 GeV in pp collisions at  $\sqrt{s} = 7$  and 8 TeV*, *JHEP* **06** (2013) 081, [arXiv:1303.4571].
- [26] CMS Collaboration, V. Khachatryan *et. al.*, *Precise determination of the mass of the Higgs boson and tests of compatibility of its couplings with the standard model predictions using proton collisions at 7 and 8 TeV*, *Eur. Phys. J. C* **75** (2015), no. 5 212, [arXiv:1412.8662].
- [27] ATLAS Collaboration, G. Aad *et. al.*, *Measurement of the Higgs boson mass from the  $H \rightarrow \gamma\gamma$  and  $H \rightarrow ZZ^* \rightarrow 4\ell$  channels with the ATLAS detector using 25  $fb^{-1}$  of pp collision data*, *Phys. Rev. D* **90** (2014), no. 5 052004, [arXiv:1406.3827].
- [28] ATLAS, CMS Collaboration, G. Aad *et. al.*, *Combined Measurement of the Higgs Boson Mass in pp Collisions at  $\sqrt{s} = 7$  and 8 TeV with the ATLAS and CMS Experiments*, *Phys. Rev. Lett.* **114** (2015) 191803, [arXiv:1503.0758].
- [29] R. Barbieri and G. F. Giudice, *Upper Bounds on Supersymmetric Particle Masses*, *Nucl. Phys. B* **306** (1988) 63–76.
- [30] J. L. Feng, *Naturalness and the Status of Supersymmetry*, *Ann. Rev. Nucl. Part. Sci.* **63** (2013) 351–382, [arXiv:1302.6587].
- [31] N. Craig, *The State of Supersymmetry after Run I of the LHC*, in *Beyond the Standard Model after the first run of the LHC Arcetri, Florence, Italy, May 20-July 12, 2013*, 2013. arXiv:1309.0528.
- [32] M. Papucci, J. T. Ruderman, and A. Weiler, *Natural SUSY Endures*, *JHEP* **09** (2012) 035, [arXiv:1110.6926].
- [33] J. A. Casas, J. Moreno, S. Robles, K. Rolbiecki, and B. Zaldívar, *What is a Natural SUSY scenario?*, *JHEP* **06** (2015) 070, [arXiv:1407.6966].
- [34] E. Witten, *Dynamical breaking of supersymmetry*, *Nucl. Phys. B* **188** (1981) 513.
- [35] S. Dimopoulos and H. Georgi, *Softly broken supersymmetry and  $SU(5)$* , *Nucl. Phys. B* **193** (1981) 150.
- [36] P. Ramond, *Dual theory for free fermions*, *Phys. Rev. D* **3** (1971) 2415.
- [37] Y. A. Gol’fand and E. P. Likhtman, *Extension of the algebra of Poincaré group generators and violation of  $P$  invariance*, *JETP Lett.* **13** (1971) 323.

- [38] A. Neveu and J. H. Schwarz, *Factorizable dual model of pions*, *Nucl. Phys. B* **31** (1971) 86.
- [39] D. V. Volkov and V. P. Akulov, *Possible universal neutrino interaction*, *JETP Lett.* **16** (1972) 438.
- [40] J. Wess and B. Zumino, *A lagrangian model invariant under supergauge transformations*, *Phys. Lett. B* **49** (1974) 52.
- [41] J. Wess and B. Zumino, *Supergauge transformations in four dimensions*, *Nucl. Phys. B* **70** (1974) 39.
- [42] P. Fayet, *Supergauge invariant extension of the Higgs mechanism and a model for the electron and its neutrino*, *Nucl. Phys. B* **90** (1975) 104.
- [43] H. P. Nilles, *Supersymmetry, supergravity and particle physics*, *Phys. Rep.* **110** (1984) 1.
- [44] C. Csaki, *The Minimal supersymmetric standard model (MSSM)*, *Mod. Phys. Lett. A* **11** (1996) 599, [hep-ph/9606414].
- [45] R. Barbier *et. al.*, *R-parity violating supersymmetry*, *Phys. Rept.* **420** (2005) 1–202, [hep-ph/0406039].
- [46] B. C. Allanach, A. Dedes, and H. K. Dreiner, *Bounds on R-parity violating couplings at the weak scale and at the GUT scale*, *Phys. Rev. D* **60** (1999) 075014, [hep-ph/9906209].
- [47] B. Bajc, J. Hisano, T. Kuwahara, and Y. Omura, *Threshold corrections to dimension-six proton decay operators in non-minimal SUSY SU (5) GUTs*, *Nucl. Phys. B* **910** (2016) 1–22, [arXiv:1603.0356].
- [48] **Super-Kamiokande** Collaboration, H. Nishino *et. al.*, *Search for Proton Decay via  $p \rightarrow e + \pi^0$  and  $p \rightarrow \mu + \pi^0$  in a Large Water Cherenkov Detector*, *Phys. Rev. Lett.* **102** (2009) 141801, [arXiv:0903.0676].
- [49] C. Csaki and B. Heidenreich, *A Complete Model for R-parity Violation*, *Phys. Rev. D* **88** (2013) 055023, [arXiv:1302.0004].
- [50] G. Krnjaic and D. Stolarski, *Gauging the Way to MFV*, *JHEP* **04** (2013) 064, [arXiv:1212.4860].
- [51] **CMS** Collaboration, S. Chatrchyan *et. al.*, *Description and performance of track and primary-vertex reconstruction with the CMS tracker*, *JINST* **9** (2014), no. 10 P10009, [arXiv:1405.6569].

- [52] K. Rose, *Deterministic annealing for clustering, compression, classification, regression, and related optimization problems*, Proceedings of the IEEE **86** (Nov, 1998) 2210–2239.
- [53] Früwirth, R and Waltenberger, Wolfgang and Vanlaer, Pascal, *Adaptive Vertex Fitting*, Tech. Rep. CMS-NOTE-2007-008, CERN, Geneva, Mar, 2007.
- [54] CMS Collaboration, *Particle-flow reconstruction and global event description with the cms detector*, Journal of Instrumentation **12** (2017), no. 10 P10003.
- [55] **CMS Collaboration** Collaboration, *Particle-Flow Event Reconstruction in CMS and Performance for Jets, Taus, and MET*, Tech. Rep. CMS-PAS-PFT-09-001, CERN, Geneva, Apr, 2009.
- [56] **CMS Collaboration** Collaboration, *Commissioning of the Particle-flow Event Reconstruction with the first LHC collisions recorded in the CMS detector*, Tech. Rep. CMS-PAS-PFT-10-001, 2010.
- [57] CMS Collaboration, “Cut-based Electron Identification in Run 2.” [https://twiki.cern.ch/twiki/bin/view/CMS/CutBasedElectronIdentificationRun2Archive#Spring15\\_selection\\_25ns](https://twiki.cern.ch/twiki/bin/view/CMS/CutBasedElectronIdentificationRun2Archive#Spring15_selection_25ns), May, 2017. Accessed: May 01, 2018.
- [58] K. Rehermann and B. Tweedie, *Efficient identification of boosted semileptonic top quarks at the LHC*, JHEP **03** (2011) 059, [arXiv:1007.2221].
- [59] **CMS Collaboration**, V. Khachatryan *et. al.*, *Performance of electron reconstruction and selection with the CMS detector in proton-proton collisions at  $\sqrt{s} = 8$  TeV*, JINST **10** (2015) P06005, [arXiv:1502.0270].
- [60] CMS Collaboration, “Baseline muon selections for Run-II.” [https://twiki.cern.ch/twiki/bin/viewauth/CMS/SWGuideMuonIdRun2#Medium\\_Muon](https://twiki.cern.ch/twiki/bin/viewauth/CMS/SWGuideMuonIdRun2#Medium_Muon), April, 2018. Accessed: May 01, 2018.
- [61] **CMS Collaboration**, S. Chatrchyan *et. al.*, *Performance of CMS muon reconstruction in pp collision events at  $\sqrt{s} = 7$ TeV*, JINST **7** (2012) P10002, [arXiv:1206.4071].
- [62] S. D. Ellis and D. E. Soper, *Successive combination jet algorithm for hadron collisions*, Phys. Rev. **D48** (1993) 3160–3166, [hep-ph/9305266].
- [63] Y. L. Dokshitzer, G. D. Leder, S. Moretti, and B. R. Webber, *Better jet clustering algorithms*, JHEP **08** (1997) 001, [hep-ph/9707323].
- [64] M. Cacciari, G. P. Salam, and G. Soyez, *The Anti- $k(t)$  jet clustering algorithm*, JHEP **04** (2008) 063, [arXiv:0802.1189].

- [65] G. P. Salam, *Towards Jetography*, *Eur. Phys. J.* **C67** (2010) 637–686, [arXiv:0906.1833].
- [66] M. Cacciari, G. P. Salam, and G. Soyez, *FastJet User Manual*, *Eur. Phys. J.* **C72** (2012) 1896, [arXiv:1111.6097].
- [67] M. Cacciari and G. P. Salam, *Pileup subtraction using jet areas*, *Phys. Lett.* **B659** (2008) 119–126, [arXiv:0707.1378].
- [68] CMS Collaboration, “Jet Identification for the 13 TeV data Run2016.” <https://twiki.cern.ch/twiki/bin/view/CMS/JetID13TeVRun2016>, February, 2018. Accessed: May 01, 2018.
- [69] T. C. collaboration, *Determination of jet energy calibration and transverse momentum resolution in cms*, *Journal of Instrumentation* **6** (2011), no. 11 P11002.
- [70] CMS Collaboration, S. Chatrchyan *et. al.*, *Identification of b-quark jets with the CMS experiment*, *JINST* **8** (2013) P04013, [arXiv:1211.4462].
- [71] M. Cacciari and G. P. Salam, *Dispelling the  $N^3$  myth for the  $k_t$  jet-finder*, *Phys. Lett.* **B641** (2006) 57–61, [hep-ph/0512210].
- [72] ATLAS Collaboration, M. Aaboud *et. al.*, *Search for top-squark pair production in final states with one lepton, jets, and missing transverse momentum using 36  $\text{fb}^{-1}$  of  $\sqrt{s} = 13$  TeV  $pp$  collision data with the ATLAS detector*, arXiv:1711.1152.
- [73] CMS Collaboration, V. Khachatryan *et. al.*, *Search for supersymmetry in  $pp$  collisions at  $\sqrt{s} = 13$  TeV in the single-lepton final state using the sum of masses of large-radius jets*, *JHEP* **08** (2016) 122, [arXiv:1605.0460].
- [74] A. Hook, E. Izaguirre, M. Lisanti, and J. G. Wacker, *High Multiplicity Searches at the LHC Using Jet Masses*, *Phys. Rev.* **D85** (2012) 055029, [arXiv:1202.0558].
- [75] T. Cohen, E. Izaguirre, M. Lisanti, and H. K. Lou, *Jet Substructure by Accident*, *JHEP* **03** (2013) 161, [arXiv:1212.1456].
- [76] S. El Hedri, A. Hook, M. Jankowiak, and J. G. Wacker, *Learning How to Count: A High Multiplicity Search for the LHC*, *JHEP* **08** (2013) 136, [arXiv:1302.1870].
- [77] ATLAS Collaboration, G. Aad *et. al.*, *Search for massive supersymmetric particles decaying to many jets using the ATLAS detector in  $pp$  collisions at  $\sqrt{s} = 8$  TeV*, *Phys. Rev.* **D91** (2015), no. 11 112016, [arXiv:1502.0568]. [Erratum: *Phys. Rev.* D93,no.3,039901(2016)].

- [78] **ATLAS** Collaboration, G. Aad *et. al.*, *Search for new phenomena in final states with large jet multiplicities and missing transverse momentum at  $\sqrt{s}=8$  TeV proton-proton collisions using the ATLAS experiment*, *JHEP* **10** (2013) 130, [arXiv:1308.1841]. [Erratum: JHEP01,109(2014)].
- [79] **CMS** Collaboration, A. M. Sirunyan *et. al.*, *Search for Supersymmetry in pp Collisions at  $\sqrt{s} = 13$  TeV in the Single-Lepton Final State Using the Sum of Masses of Large-Radius Jets*, *Phys. Rev. Lett.* **119** (2017), no. 15 151802, [arXiv:1705.0467].
- [80] **CMS Collaboration** Collaboration, *Commissioning the performance of key observables used in SUSY searches with the first 13 TeV data*, .
- [81] J. Alwall, R. Frederix, S. Frixione, V. Hirschi, F. Maltoni, O. Mattelaer, H. S. Shao, T. Stelzer, P. Torrielli, and M. Zaro, *The automated computation of tree-level and next-to-leading order differential cross sections, and their matching to parton shower simulations*, *JHEP* **07** (2014) 079, [arXiv:1405.0301].
- [82] J. Alwall *et. al.*, *Comparative study of various algorithms for the merging of parton showers and matrix elements in hadronic collisions*, *Eur. Phys. J. C* **53** (2008) 473, [arXiv:0706.2569].
- [83] R. Frederix and S. Frixione, *Merging meets matching in MC@NLO*, *JHEP* **12** (2012) 061, [arXiv:1209.6215].
- [84] P. Nason, *A new method for combining NLO QCD with shower Monte Carlo algorithms*, *JHEP* **11** (2004) 040, [hep-ph/0409146].
- [85] S. Frixione, P. Nason, and C. Oleari, *Matching NLO QCD computations with parton shower simulations: the POWHEG method*, *JHEP* **11** (2007) 070, [arXiv:0709.2092].
- [86] S. Alioli, P. Nason, C. Oleari, and E. Re, *A general framework for implementing NLO calculations in shower Monte Carlo programs: the POWHEG BOX*, *JHEP* **06** (2010) 043, [arXiv:1002.2581].
- [87] **NNPDF** Collaboration, R. D. Ball *et. al.*, *Parton distributions for the LHC Run II*, *JHEP* **04** (2015) 040, [arXiv:1410.8849].
- [88] T. Sjöstrand, S. Ask, J. R. Christiansen, R. Corke, N. Desai, P. Ilten, S. Mrenna, S. Prestel, C. O. Rasmussen, and P. Z. Skands, *An introduction to PYTHIA 8.2*, *Comput. Phys. Commun.* **191** (2015) 159.
- [89] P. Skands, S. Carrazza, and J. Rojo, *Tuning PYTHIA 8.1: the Monash 2013 tune*, *Eur. Phys. J. C* **74** (2014) 3024.

- [90] **GEANT4** Collaboration, S. Agostinelli *et. al.*, *GEANT4—a simulation toolkit*, *Nucl. Instrum. Meth. A* **506** (2003) 250.
- [91] M. Czakon, P. Fiedler, and A. Mitov, *Total top-quark pair-production cross section at hadron colliders through  $\mathcal{O}(\alpha_S^4)$* , *Phys. Rev. Lett.* **110** (Jun, 2013) 252004.
- [92] R. Gavin, Y. Li, F. Petriello, and S. Quackenbush, *W Physics at the LHC with FEWZ 2.1*, *Comput. Phys. Commun.* **184** (2013) 208, [arXiv:1201.5896].
- [93] S. Alioli, P. Nason, C. Oleari, and E. Re, *NLO single-top production matched with shower in POWHEG: s- and t-channel contributions*, *JHEP* **09** (2009) 111, [arXiv:0907.4076]. [Erratum: DOI10.1007/JHEP02(2010)011].
- [94] E. Re, *Single-top Wt-channel production matched with parton showers using the POWHEG method*, *Eur. Phys. J. C* **71** (2011) 1547, [arXiv:1009.2450].
- [95] S. Frixione, V. Hirschi, D. Pagani, H. S. Shao, and M. Zaro, *Electroweak and QCD corrections to top-pair hadroproduction in association with heavy bosons*, *JHEP* **06** (2015) 184, [arXiv:1504.0344].
- [96] G. Bevilacqua and M. Worek, *Constraining BSM Physics at the LHC: Four top final states with NLO accuracy in perturbative QCD*, *JHEP* **07** (2012) 111, [arXiv:1206.3064].
- [97] Z. Nagy, *Three jet cross-sections in hadron hadron collisions at next-to-leading order*, *Phys. Rev. Lett.* **88** (2002) 122003, [hep-ph/0110315].
- [98] J. Alwall, P. Schuster, and N. Toro, *Simplified Models for a First Characterization of New Physics at the LHC*, *Phys. Rev. D* **79** (2009) 075020, [arXiv:0810.3921].
- [99] **LHC New Physics Working Group** Collaboration, D. Alves, *Simplified Models for LHC New Physics Searches*, *J. Phys. G* **39** (2012) 105005, [arXiv:1105.2838].
- [100] L. Lyons, D. Gibaut, and P. Clifford, *How to combine correlated estimates of a single physical quantity*, *Nuclear Instruments and Methods in Physics Research Section A: Accelerators, Spectrometers, Detectors and Associated Equipment* **270** (1988), no. 1 110 – 117.
- [101] **CMS** Collaboration, S. Chatrchyan *et. al.*, *Determination of jet energy calibration and transverse momentum resolution in CMS*, *JINST* **6** (2011) P11002, [arXiv:1107.4277].
- [102] **CMS** Collaboration, V. Khachatryan *et. al.*, *Jet energy scale and resolution in the CMS experiment in pp collisions at 8TeV*, *JINST* **12** (2017), no. 02 P02014, [arXiv:1607.0366].

- [103] CMS Collaboration, GHM *et. al.*, *CMS luminosity measurements for the 2016 data taking period*, CMS Physics Analysis Summary CMS-PAS-LUM-17-001, 2017.
- [104] A. L. Read, *Presentation of search results: the CL<sub>s</sub> technique*, *J. Phys. G* **28** (2002) 2693.
- [105] ATLAS and CMS Collaborations, LHC Higgs Combination Group, *Procedure for the LHC Higgs boson search combination in Summer 2011*, Technical Report CMS-NOTE-2011-005, ATL-PHYS-PUB-2011-11, 2011.
- [106] G. Cowan, K. Cranmer, E. Gross, and O. Vitells, *Asymptotic formulae for likelihood-based tests of new physics*, *Eur. Phys. J. C* **71** (2011) 1554. [Erratum: DOI10.1140/epjc/s10052-013-2501-z].
- [107] T. Junk, *Confidence level computation for combining searches with small statistics*, *Nucl. Instrum. Meth. A* **434** (1999) 435, [hep-ex/9902006].